REPUBLIQUE ALGERIENNE DEMOCRATIQUE ET POPULAIRE

MINISTERE DE L'ENSEIGNEMENT SUPERIEUR ET DE LA RECHERCHE SCIENTIFIQUE
UNIVERSITE FERHAT ABBAS – SETIF -1-

THESE

Présentée à l'Institut d'Optique et Mécanique de Précision
Pour l'obtention du diplôme de

DOCTORAT LMD
En Optique et Photonique Appliquée

Par

Saoussene Chabou

Thème

Amélioration des performances des faisceaux lasers par l'optique diffractive

Soutenue le : 07/07/2021 devant le jury composé de

Président	**K. Ferria**	**Professeur**	**U.F.A Sétif -1**
Rapporteur	**A. Bencheikh**	**MCA**	**U. BBA**
Examinateurs	**B. Bakhouche**	**MCA**	**U.F.A Sétif -1**
	N. Demagh	**Professeur**	**U.F.A Sétif -1**
	A. Hamadou	**Professeur**	**U. BBA**

PEOPLE'S DEMOCRATIC REPUBLIC OF ALGERIA

MINISTRY OF HIGHER EDUCATIONAND SCIENTIFIC RESEARCH

FERHAT ABBAS UNIVERSITY – SETIF -1-

THESIS

Submitted to Institute of Optics and Precision Mechanics

For the degree

Doctorate

In Applied Optics and Photonics

By

Saoussene Chabou

Title

Improvement of laser beams performances by diffractive optics

Defended on: 07/07/2021 in front of the composed committee of

Chairman	**K. Ferria**	**Professor**	**F.A.U Setif -1**
Supervisor	**A. Bencheikh**	**Assistant Professor**	**BBA.U**
Examiners	**B. Bakhouche**	**Assistant Professor**	**F.A.U Setif -1**
	N. Demagh	**Professor**	**F.A.U Setif -1**
	A. Hamadou	**Professor**	**BBA.U**

In the Name of God, Most Gracious, Most Merciful

Allah is the Light of the heavens and the earth. The example of His light is like a niche within which is a lamp, the lamp is within glass, the glass as if it were a pearly [white] star lit from [the oil of] a blessed olive tree, neither of the east nor of the west, whose oil would almost glow even if untouched by fire. Light upon light. Allah guides to His light whom He wills. And Allah presents examples for the people, and Allah is Knowing of all things.

An-Nur 24:35

Acknowledgment

First and foremost, the acknowledgment must be made to my supervisor Mr. Bencheikh Abdelhlim. I would like sincerely to thank him for all the time and effort he spent in assisting me in my work. Thank you for being an inspirational mentor and for motivating me to pursue relevant research.

During my doctoral thesis, I have been extremely lucky to, twice, visit the Structured Light Laboratory of Wits University of Johannesburg, South Africa as a part of an internship, where I did the experimental work found in this thesis. I am very grateful to all members of the Structured Light Laboratory for their welcome and helping to make both internships an enriching experience. In particular, I would like to thank Prof. Andrew Forbes for his warm welcome, kind support, guidance, and invaluable advice during my internship. To Dr. Valaria Rodríguez-Fajardo and Mr. Jonathan Pinnell for all their help. Working with you was a pleasure!

I would express my profound gratitude to Mr. Ferria Kouider for accepting to preside my thesis defense committee. Many thanks go to Mr. Hamadou Abdelouahab, Mr. Demagh Nacereddine, and Mr. Bakhouche Belkacem for accepting to review my thesis manuscript and for their presence in defense committee . Special acknowledgment to my team and all my colleagues at the Institute of Optics and Precision Mechanics.

I am so grateful to my family and friends for their support and for encouraging me to fur-

ther my studies. To my parents for their unconditional confidence which always sustains me. Thank you for always taking an interest in my research and for providing endless support while I pursue my goals.

Finally, I wish to express my sincere gratitude and appreciation to everyone who assisted and supported me throughout the course of this work.

Contents

Acknowledgment iii

Contents v

List of Figures viii

List of Publications xvi

List of Conferences xvii

Introduction 1

1 Backgrounds and basics 3

1.1 Introduction 3

1.2 The Helmholtz wave equation 4

1.3 Fundamental Gaussian beam 7

1.4 Higher-order Gaussian beams 9

1.4.1 Standard Gaussian beams 9

1.4.2 Elegant Gaussian beams 12

1.4.3 Free-diffraction beams 13

1.5 Spatial Light Modulator (SLM) 15

1.5.1 Digital holograms 16

2 Characterizing the diffraction of the Laguerre-Gauss beams by an aperture and an opaque disk 19

2.1 Introduction . . . 19

2.2 LG beam diffraction . . . 20

2.3 Self-healing concept . . . 24

2.4 Abbe experiment and spatial filtering . . . 26

2.5 Experimental realisation of diffracted LG beams . . . 27

2.6 Experimental results versus numerical simulations . . . 30

2.6.1 Diffraction patterns . . . 30

2.6.2 Diffraction spatial characteristics (beam propagation factor and the focal shift effect) . . . 36

2.7 Conclusion . . . 43

3 Modeling the diffraction of the Laguerre-Gauss beams by an aperture and an opaque disk 45

3.1 Introduction . . . 45

3.2 Comparison between Laguerre-Gauss beam and Bessel beam . . . 46

3.3 Analytical description of diffracted LG beam . . . 52

3.3.1 Far-field of the diffracted LGB by small apertures . . . 53

3.3.2 Far-field of the diffracted LGB by an opaque disk . . . 54

3.4 conclusion . . . 63

4 Spatial and propagation properties of the Cosine-Gauss beams 64

4.1 Introduction . . . 64

4.2 Theory of Cosine beam . . . 65

4.3 Diffraction-free nature of Cosine-Gauss beams . . . 67

4.3.1 Propagation characteristics of apodized-Cosine beam . . . 68

4.3.2 Propagation characteristics of higher-order Cosine-Gauss beam . . . 74

4.4 Self-healing property . . . 81

4.5 Conclusion 85

5 The diffraction-free nature of elegant Gaussian beams 87

5.1 Introduction 87

5.1.1 The relationship between the pseudo-nondiffracting beams and the elegant-Gaussian beams 88

5.1.2 Propagation path comparison 89

5.1.3 Transverse shape comparison 91

5.1.4 Quantitative comparison 96

5.2 Non diffracting nature of elegant Gaussian beams 98

5.3 Self-healing ability of elegant Gaussian beams 101

5.4 Conclusion 108

Conclusion 109

5.5 Conclusions 109

5.6 Future studies 110

Bibliography 111

List of Figures

1.1 The Gaussian propagation parameters; The waist, at $z = 0$, has radius w_0. The distance at which the beam has spread to double the area at the waist is the Rayleigh range, z_R. 8

1.2 (a) Transverse intensity profile and (b) cross-sectional intensity profile of a Gaussian beam. 8

1.3 Transverse intensity profiles of higher order Hermite Gaussian beams with different mode indices. 10

1.4 Transverse intensity profiles of higher order Laguerre Gaussian beams with different radial and azimuthal mode indices. 11

1.5 (a, c) Cross-sectional profile and (b, d) transverse profile of intensity of (a, b) a Hermite Gaussian beam ($n = m = 10$) and (c, d) a Laguerre Gaussian beam ($p = 5, l = 0$). 12

1.6 (a, c) Cross-sectional profile and (b, d) transverse profile of intensity of (a, b) an elegant HG beam ($n = m = 10$) and (c, d) an elegant LG beam ($p = 5, l = 0$). 13

1.7 (a, c) Cross-sectional profile and (b, d) transverse profile of intensity of (a, b) a Bessel Gaussian beam and (c, d) a Cosine Gaussian beam. 14

1.8 (a) Illustration of an individual pixel in the liquid crystal display. The pixel (liquid crystal filled cell) is electrically adjusted with an applied voltage. (b) Holoeye SLM. The number of pixels is determined by the resolution of the SLM screen. 16

2.1 Schematic Conceptualizing the diffraction of radial LG beam by (a) an aperture and (b) an opaque disk, and then focused with a lens. The incident beam is partially blocked at the lens plane ($z = 0$) by an obstruction of some radius, selected to coincide with the zeros of the initial beam. The output beam is investigated both at the geometrical focal plane (Fourier plane) of the lens and at the shifted focal plane (shifted plane in short), which corresponds to the plane where the second moment width of the output beam is minimum. 21

2.2 Diffraction geometry, showing the object plane and the image plane. . . . 23

2.3 Numerical simulation for an LG_{50} beam. Density plots in the ξz-plane (top row) and profiles along the ξ-axis (bottom row) of the intensity distribution of the beam for (a) an unobstructed beam, the beam after passing through (b) an aperture, and (c) an opaque disk. 24

2.4 Self-healing principle of BG beams. Conical waves, that formed by refracting plane waves incident on axicon, form a BG beam in the region z_{max}. An opaque obstruction placed at$1/2z_{max}$ blocks a part of waves while allowing the other part (unblocked waves) to interfere at a short distance behind the obstruction, i.e., after z_{min}. The region where the beam is predicted to self-heal totally is the plane z_0. 25

2.5 Spatial filtering. $4f$ optical imaging system perform a Fourier transform followed by an inverse Fourier transform. The Fourier components of the object are separated by the first lens into spatial fraquencies at the Fourier plane. The object Fourier transformed is multiplied by the transmittance of the spatial filter, then the second lens reconstructs the image (inverse Fourier transform of the filtred version). 27

2.6 Holograms encoded on the SLM (top) and experimental intensity profiles (bottom) of Laguerre-Gaussian beam of order $p = 5$. The first column presents the un-obstructed case, the first and third row show the obstruction case by an aperture, and the second and fourth row show the obstruction case by an opaque disk. 29

2.7 Schematic of the experimental setup used to study the diffraction of an LG beam ($p = 5$) by an aperture or an opaque disk. The SLM simultaneously generates the obstructed beam and encodes the lens. 30

2.8 Experimental and theoretical (insets) intensity patterns and the corresponding cross-sectional profiles for non-obstructed LG beam of order $p = 5$, at (a) the shifted plane and (b) the geometric focal plane (Fourier plane). 31

2.9 Experimental and theoretical (insets) intensity patterns (top) and the corresponding cross-sectional profiles (bottom) for an obstructed LG_{50} beam by an aperture, on (a), (d) its second intensity zero, (b), (e) third intensity zero, and (c), (f) fifth intensity zero, at the shifted plane (a), (b) and (c) and at the Fourier plane (d), (e) and (f). 32

2.10 Experimental and theoretical (insets) intensity patterns (top) and associated cross-sectional profiles (bottom) for an obstructed LG_{50} beam by an opaque disk, on (a), (d) its second intensity zero, (b), (e) third intensity zero, and (c), (f) fifth intensity zero, at the near field $z = 10$ mm (a), (b) and (c) and at the shifted plane (d), (e) and (f). 34

2.11 Similarity, S, of both blocked (opaque disk) and apertured LG_{50} beams as a function of the normalized obstruction size, a/w_0. The red dots indicate the positions of the intensity zeros of the LG_{50} beam. 36

2.12 The percentage change in (a) the beam quality factor and (b) focal shift of the obstructed beam as compared to the unobstructed beam, calculated as a function of the normalized obstruction size for an aperture and an opaque disk (blocked). All calculations assumed an initial LG_{50} beam with an $M^2 = 2p + 1$. 41

2.13 Theoretical and experimental beam radius as a function of normalized propagation distance for (a) unobstructed, and obstructed by (b) an aperture, and (c) an opaque disk. In all cases the initial beam was an LG_{50} obstructed at its third intensity zero. The measured and predicted M^2 values are given in the insets. 43

3.1 The transverse cross sections and the intensity profiles of the LGB_n and its equivalent BB (top), for a beam order $p = 10$, showing the truncated versions (bottom). 48

3.2 The on-axis intensty (first column) and the propagation in the $\xi - z$ (second and third column) of the LGB_p and its equivalent BB (top), for a beam order $p = 10$, showing the truncated versions (bottom). 49

3.3 The similarity degree between LGB_p and its equivalent BB as a function of the truncation parameter δ, for different beam orders p. 50

3.4 The LGB_p versus the BB. (a) and (b), represent respectively the unobstructed LGB_{10} and BB. (c) and (d), represent respectively the truncated LGB_{10} and BB. (e) and (f), represent the remaining outer multi-ring part of the truncated LGB_{10} and BB shown in (c) and (d). 51

3.5 The new modeling representation of the outer multi-ring part of the LGB_{10}. (a) The outer multi-ring part of the LGB_{10}, (b) A sum of rings represented by different colors located at the same LGB_{10} rings. The white profiles correspond to the LGB_{10} intensity distribution. 52

3.6 The intensity distribution at the focal plane of a lens ($f = 100mm$) of the apertured LGB_{10}, from, on its second intensity's zero in (a) to on its sixth intensity's zero in (i); numerical integration (in red) versus analytical expression (in blue). 54

3.7 The intensity distribution at the focal plane of a lens ($f = 100mm$) of the obstructed LGB_{10}, from, on its second intensity's zero in (a) to on its last intensity's zero in (i); numerical integration (in red) versus analytical expression (in blue). 56

3.8 Schema illustrating the different parameters of ring shifted-Gaussian beams. 57

3.9 Density plots (a,c) and transverse intensities (b,d) of obstructed LGB_p (in blue) modeled as a sum of ring shifted-Gaussian beams (in red). The white curve represents LGB_{10} profile, while the yellow five rings are ring shifted-Gaussian beams located at the same positions as the LGB_{10} rings. 58

3.10 The on-axis intensity of the obstructed LGB_{10} as a function of the normalized propagation distance. (a) obstructed LGB_{10} (in blue) with its equivalent five ring shifted-Gaussian beam (in red), (b) the obstructed LGB_{10} with its equivalent two rings shifted-Gaussian beam. 59

3.11 (a)The similarity degree between the obstructed LGB_{10} and its equivalent ring shifted-Gaussian beams for a different number of the remaining rings. (b) The transverse cross-sections of the obstructed LGB_{10} on its centrale lobe and the corresponding ring shifted-Gaussian beams. 60

3.12 The intensity distributions of the obstructed LGB_{10} (blue line) and the shifted-ring Gaussian beams (red line), at the input plane on the left and the Fourier plane on the right. 62

4.1 Cosine beams Generation using (a) an axicon [1] and (b) a diffractive optical element (DOE) or a Spatial light modulator (SLM). (b) and (d) Numerical simulations. $\sin(\vartheta) = k_y/k$ and $\tan(\vartheta) = a/z_{max}$ 67

4.2 Propagation characteristics of apodized Cosine beam. (a) Windowed-Cosine beam. (b) Cosine-Gauss beam. (Both beams have the same width $w_0 = 1mm$). 69

4.3 (a) The normalized CB width and (b) the normalized nondiffracting distance, as a function of CG parameter α. 72

4.4 CG beam intensity profile showing the effect of k_y on its spatial extent (width). 73

4.5 CG beam propagation in $(\eta - z)$ plane for different values of α; (a) $\alpha = 0$, (b) $\alpha = 1.6$, (c) $\alpha = 5$, and (d) $\alpha = 10$. 74

4.6 Generation of higher order Cosine-Gauss HCG_n beam with $n = 10$ using a prism. 75

4.7 Simulations of generated higher order Cosine-Gauss beam using: (a) prism and (b) DOE. 76

4.8 The normalized HCG_n beam width as a function of α parameter. 80

4.9 The normalized HCG_n beam range as a function of α parameter for different beam order n values. 81

4.10 HCG beam propagation in $(\eta - z)$ plane for different values of α; (a) $\alpha = 0$, (b) $\alpha = 1$, (c) $\alpha = 5$, and (d) $\alpha = 10$. 81

4.11 Self-healing ability investigation of the HCG_n beams. (a) $n = 0$ with obstruction size 0.25,(b) $n = 0$ with obstruction size 0.5, (c)$n = 10$ with obstruction size 1, and (d)$n = 10$ with obstruction size 2.5. 82

4.12 Self-healing of obstructed HCG_{10} beam with $\alpha = 10$ undergone different obstacle sizes. 84

5.1 The density plots in the plane $\xi - z$ (top row) and the on-axis intensity distribution (bottom row) of the (a) eHG beam ($n = 10$) and the equivalent CG beam, (b)the eLG beam ($p = 10$, $l = 0$) and the equivalent BG beam. 91

5.2 The intensity profiles (top row) and the transverse cross-sections (bottom row) of the eHG beam ($n = 10$) and its corresponding CG beam, (a) at the initial plane ($z = 0$) and (b) at the far-field ($z = f$). 93

5.3 The intensity profiles (top row) and the transverse cross-sections (bottom row) of the eLG beam ($p = 10$) and its corresponding BG beam, (a) at the initial plane ($z = 0$) and (b) at the far-field ($z = f$). 94

5.4 The 3D intensity profiles of the eHG beam ($n = 10$) and its corresponding CG beam, at the initial plane ($z = 0$) on the left side and at the far-field ($z = f$) on the right side. 95

5.5 The 3D intensity profiles of the eLG beam ($p = 10$) and its corresponding BG beam, at the initial plane ($z = 0$) on the left side and at the far-field ($z = f$) on the right side. 96

5.6 Illustration of similarity degree between the two classes of beams at $z = 0$ (top) and at $z = f$ (bottom). (a) The elegant Hermite-Gauss beam and its equivalent Cosine-Gauss beam, (b) the elegant Laguerre-Gauss beam and its equivalent Bessel-Gauss beam. For all the presented beam orders n and in both cases, the value of similarity degree is about 0.99. 97

5.7 The normalized nondiffracting range z_{max}/z_R ,as a function of the beam order, for (a) elegant Laguerre-Gauss beam and (b) elegant Hermite-Gauss beam. 100

5.8 The density plot in the plane $\xi - z$ of the propagated (a) elegant Laguerre-Gauss beam and (b) elegant Hermite-Gauss beam, of beam order $p = n = 10$.100

5.9 (color online) The density plot in the plane $\xi - z$ of the obstructed elegant Hermite-Gauss beam ($n = 10$) by (a) a small obstacle and (b) a big obstacle, with showing the minimum distance z_{min} before the reconstruction occurs. The bold yellow line at the initial plane denotes the size and the position of the obstacle, while the dotted half-rectangle indicates the shadow region. 102

5.10 The density plot in the plane $\xi - z$ of the obstructed elegant Laguerre-Gauss beam ($p = 10$)by (a) a small obstacle and (b) a big obstacle, with showing the minimum distance z_{min} before reconstruction occurs. The bold yellow line at the initial plane denotes the size and the position of the obstacle, while the dotted half-circle indicates the shadow region. 103

5.11 The on-axis intensity distribution of unobstructed beam (green curve) and obstructed beam by small (yellow curve) and big obstacle (black curve). (a) eHG beam of beam order $n = 10$, (b) eLG beam of beam order $p = 10$. The plane z_0 is the plane corresponding to the on-axis intensity maximum. 104

5.12 The intensity patterns and their corresponding profiles at the obstacle plane $z = 0$ (a,c) and at the $z = z_0$ plane (b,d) of obstructed eHG beam ($n = 10$), by a small (a,b) and big obstacle (c,d); showing the self reconstruction process. The obstructed eHG beam at the plane $z = z_0$ is compared with the un-obstructed one (yellow curve); shown in (g) and (h) 105

5.13 The intensity patterns and its corresponding profiles at the obstacle plane $z = 0$ (a,c) and at the $z = z_0$ plane (b,d) of obstructed eLG beam ($p = 10$), by a small (a,b) and big obstacle (c,d); showing the self reconstruction process. The obstructed eLG beam at the plane $z = z_0$ is compared with the un-obstructed one (yellow curve); shown in (g) and (h) 106

List of Publications

1. A. Bencheikh, **S. Chabou**, O.C. Boumeddine, H. Bekkis, A. Benstiti, L. Beddiaf, W Moussaoui, Cosine beam: diffraction-free propagation and self-healing, JOSA A, 37, C7–C14 (2020)

2. A. Bencheikh, **S. Chabou**, O.C. Boumeddine, Far-field modeling of obstructed Laguerre–Gauss beams, JOSA A, 37, C20–C26 (2020)

3. J, Pinnell, V. Rodríguez-Fajardo, A. Forbes, **S. Chabou**, K. Mihoubi, A. Bencheikh, Revealing the modal content of obstructed beams, Physical Review A, 102, 033524 (2020)

4. **S. Chabou**, J, Pinnell, A. Bencheikh, V. Rodríguez-Fajardo, A. Forbes, Do Laguerre–Gaussian beams recover their spatial properties after all obstacles?, Applied Physics B, 126, (2020)

5. **S. Chabou** and A. Bencheikh, Elegant Gaussian beams: the nondiffracting nature and self-healing property, Applied Optics, 59,(2020)

List of Conferences

International

1. **S. Chabou**, A. Bencheikh, Shaping of a Laguerre Gaussian beam by an annular aperture, ICRA (2017).
2. **S. Chabou**, A. Bencheikh, Shaping of a Laguerre-Gaussian beam by a stop, OPAL (2018).
3. **S. Chabou**, A. Bencheikh, Focal shift metrology, ICIMM (2018).
4. A. Bencheikh, **S. Chabou**, Generation of Bessel beam for materials processing, ICAME (2018).
5. **S. Chabou**, A. Bencheikh, M^2 factor of radial Laguerre Gaussian beam passing through an opaque disk, AGICNT (2019).

National

1. **S. Chabou**, A. Bencheikh, Diffraction des faisceaux Laguerre-Gauss LG_{p0} par un axicon, Senalap (2017).
2. **S. Chabou**, A. Bencheikh, Mise en forme des faisceaux Laguerre-Gauss LG_{p0} par une ouverture circulaire, SNLSM (2018).

3. **S. Chabou**, A. Bencheikh, O.C. Boumeddine, Modélisation de la diffraction de faisceau Laguerre-Gauss LG_{10} par une ouverture circulaire, CNPA (2018).

Introduction

The intensity profile of the fundamental mode of lasers is generally Gaussian. Although it is sometimes useful, there are some applications for which a different shape may be desired, thus posing the need for complex light (structured light) modes. Structured light today represents an established section of the wider field of modern optics and photonics. Several classes of complex light shapes have become an experimental fact and are successfully applied in many fields of optics. The success of each application depends strongly on the understanding of the special characteristics of the propagation of the laser mode such as the beam shape, the beam quality, as well as how the beam will change after propagating a certain distance. Scientists and engineers are still working to further understand and improve laser mode characteristics that allowing for new more applications.

The work presented in this thesis is focused on the diffractive properties of higher-order Gaussian beams that passing through different optical elements.
In the first chapter, we give a brief introduction to the paraxial wave equation starting from Maxwell's equations with mentioning its particular beams solutions (the fundamental one and the higher-order ones); As well, we present a quick definition of the most commonly used and powerful tool for the experimental generation of these beams that is the spatial light modulator (SLM).
Following in chapter 2, we show, theoretically and experimentally, how the spatial properties, such as the beam propagation factor M^2 and the focal shift effect, of the higher-order Laguerre Gaussian (LG) beams change when they are passing through an aperture and

an opaque disk. In which, we find that the aperture reduces the beam propagation factor M^2 and strongly provokes the focal shift, while the opaque disk keeps almost all of these characteristics unchanged that reveals, supported by the spatial frequency filtering concept, the self-healing property of such beams.

In the same context and for the importance of the opaque disk in several imaging experiments, such as microscopy, chapter 3 presents a new way to theoretically model the LG beam when is partially blocked by an opaque disk in order to calculate its far-field intensity distribution, including the aperture case.

In chapter 4, we study analytically the non-diffracting properties of Cosine Gaussian beams, which are one-dimensional counterparts of Bessel beams, of fundamental and higher-order. The latter is generated from the interference of two oppositely oblique higher-order Hermite-Gaussian beams.

Finally, in chapter 5, we demonstrate quantitatively and qualitatively, based on asymptotic formulas, that the elegant higher-order Gaussian beams are perfectly identical to the pseudo-nondiffracting beams, we also show that they provide the same characteristics that make them a good alternative to the second one in many situations.

In general, the results presented in this thesis, relating the study and measurements of the propagated laser beam through different optical elements, can offer better performance for many applications such as optical communication (recording and transporting information with required resolution, secure communication, ...), optical trapping and micromanipulation, and microscopy.

The experimental work found in this thesis have been done in the structured light laboratory of South Africa.

Chapter 1

Backgrounds and basics

1.1 Introduction

Since the invention of the laser, the description of the spatial structure of the different beam modes has been the object of theoretical and experimental analysis. The usual starting point for the derivation of laser beam propagation modes is solving the scalar Helmholtz equation within the paraxial approximation. The paraxial approximation is used to describe laser beam propagation as the divergence angle of the beam is considered to be small. There exist many solutions to the paraxial Helmholtz wave equation, whose amplitude distribution is described by either a Gaussian, Laguerre Gaussian, Hermite Gaussian, Bessel, Airy or Mathieu functions.

In this chapter, we will not discuss all of these solutions; instead we will focus on three classes of solutions that have been studied in this thesis. We will first discuss Gaussian beams as this is the fundamental solution beam. Following, the three classes of solutions that will be discussed are standard Gaussian, elegant Gaussian, and non-diffracting beams. In the last, we will describe an effective method, which is an electronic device knows as a spatial light modulator (SLM), to generate the different laser beams.

1.2 The Helmholtz wave equation

The Maxwell's equations [2] in a vacuum, which form the foundation for the derivation of the paraxial Helmholtz wave equation [3], are defined as

$$\vec{\nabla} \cdot \vec{E} = 0, \tag{1.1}$$

$$\vec{\nabla} \cdot \vec{B} = 0, \tag{1.2}$$

$$\vec{\nabla} \times \vec{E} = -\frac{\partial \vec{B}}{\partial t}, \tag{1.3}$$

$$\vec{\nabla} \times \vec{B} = \varepsilon_0 \mu_0 \frac{\partial \vec{E}}{\partial t}. \tag{1.4}$$

where $\vec{E}$ and $\vec{B}$ are the electric and magnetic fields, ε_0 and μ_0 denote the permittivity and permeability of free space, respectively. These two latter parameters are related to the light velocity (the speed of light) in a vacuum as follows: $c = 1/\sqrt{\varepsilon_0 \mu_0}$

In order to obtain (form) the wave equation, we simplify Eq. 1.3 using the vector identity $\vec{\nabla} \times (\vec{\nabla} \times \vec{E}) = \vec{\nabla}(\vec{\nabla} \cdot \vec{E}) - \vec{\nabla}^2 \vec{E}$, , resulting in:

$$\vec{\nabla}(\vec{\nabla} \cdot \vec{E}) - \vec{\nabla}^2 \vec{E} = -\frac{\partial(\vec{\nabla} \times \vec{B})}{\partial t}. \tag{1.5}$$

Substituting Eqs. 1.1 and 1.4 into Eq. 1.5 forms the wave equation

$$\vec{\nabla}^2 \vec{E} = \varepsilon_0 \mu_0 \frac{\partial^2 \vec{E}}{\partial t^2} \Rightarrow \vec{\nabla}^2 \vec{E} - \frac{1}{c^2} \frac{\partial^2 \vec{E}}{\partial t^2} = 0. \tag{1.6}$$

The Helmholtz equation, which represents a time-independent form of the wave equation,

results by applying separation of variables on the electric field into its spatial and time domains:

$$E(x, y, z, t) = A(x, y, z)T(t). \tag{1.7}$$

Substituting Eqs. 1.7 into Eq. 1.6 yields

$$T(t)\nabla^2 A(x, y, z) - \frac{A(x, y, z)}{c^2}\frac{\partial^2 T(t)}{\partial t^2} = 0 \Rightarrow T(t)\nabla^2 A(x, y, z) = \frac{A(x, y, z)}{c^2}\frac{\partial^2 T(t)}{\partial t^2} \tag{1.8}$$

$$\frac{\nabla^2 A(x, y, z)}{A(x, y, z)} = \frac{1}{c^2 T(t)}\frac{\partial^2 T(t)}{\partial t^2} \tag{1.9}$$

Since the left and right sides of Eq. 1.8 are not dependent on the same variable, then this equation is true if both sides are equal to the same constant, $-k^2$

$$\frac{\nabla^2 A(x, y, z)}{A(x, y, z)} = -k^2 \tag{1.10}$$

and

$$\frac{1}{c^2 T(t)}\frac{\partial^2 T(t)}{\partial t^2} = -k^2 \tag{1.11}$$

Eq. 1.10 becomes

$$(\nabla^2 + k^2)A(x, y, z) = 0 \tag{1.12}$$

Eq. 1.12 describes the Helmholtz wave equation, where k is the wave number defined as $k = 2\pi/\lambda$.

The electric field propagating in the z-direction can be expressed as follows

$$A(x,y,z) = u(x,y,z)exp(ikz) \tag{1.13}$$

Substituting Eq. 1.13 into Eq. 1.12, results in

$$\nabla^2(u(x,y,z)exp(ikz)) + k^2(u(x,y,z)exp(ikz)) = 0$$

$$\frac{\partial^2 u(x,y,z)exp(ikz)}{\partial x^2} + \frac{\partial^2 u(x,y,z)exp(ikz)}{\partial y^2} + \frac{\partial^2 u(x,y,z)exp(ikz)}{\partial z^2} + k^2 u(x,y,z)exp(ikz) = 0$$

$$exp(ikz)\left(\frac{\partial^2 u(x,y,z)}{\partial x^2} + \frac{\partial^2 u(x,y,z)}{\partial y^2} + \frac{\partial^2 u(x,y,z)}{\partial z^2} + 2ik\frac{\partial u(x,y,z)}{\partial z}\right) = 0$$

$$\left(\frac{\partial^2}{\partial x^2} + \frac{\partial^2}{\partial y^2} + \frac{\partial^2}{\partial z^2}\right) u(x,y,z) + 2ik\frac{\partial u(x,y,z)}{\partial z} = 0 \tag{1.14}$$

The assumption, known as a slowly varying approximation, under which the paraxial approximation is valid, given by :

$$\left|\frac{\partial^2 u(x,y,z)}{\partial z^2}\right| << k\left|\frac{\partial u(x,y,z)}{\partial z}\right| \tag{1.15}$$

The paraxial form of the Helmholtz equation is found by substituting the above condition

into Eq. 1.14 as follows:

$$\left(\frac{\partial^2}{\partial x^2}+\frac{\partial^2}{\partial y^2}\right)u(x,y,z)+2ik\frac{\partial u(x,y,z)}{\partial z}=0 \tag{1.16}$$

Many solutions to the above equation (1.16), the paraxial Helmholtz wave equation, there exist. In the following, we only will focus on the solutions which have been studied in this thesis.

1.3 Fundamental Gaussian beam

Before moving on to higher-order types of solutions to the paraxial Helmholtz wave equation, we first describe the simplest and fundamental solution to such equation that is the Gaussian beam [4]. The amplitude E and intensity I of the Gaussian beam can be expressed in the forms

$$u(r,z)=\frac{w_0}{w(z)}\exp\left(\frac{-r^2}{w^2(z)}\right)\exp\left(-i\frac{kr^2}{2R(z)}-i\Phi(z)\right) \tag{1.17}$$

$$I(r,z)=|u(r,z)|^2=\left(\frac{w_0}{w(z)}\right)^2\exp\left(\frac{-2r^2}{w^2(z)}\right) \tag{1.18}$$

where $w(z)=\sqrt{w_0^2\left(1+z^2/z_R^2\right)}$ is the beam radius at distance z, $R(z)$ is the radius of curvature defined as $R(z)=z\left(1+z_R^2/z^2\right)$, and $\Phi(z)$ is the Gouy phase given by $\Phi(z)=\arctan\left(z/z_R\right)$. $z_R=\pi w_0^2/\lambda$ is the Rayleigh range, w_0 is the radius at the beam waist, and λ is the wavelength.

The shape of the Gaussian beam as it propagates along the z-axis is shown in Fig. 1.1, illustrating the width evolution represented by the black line. The maximum intensity

occurs on-axis at z = 0.

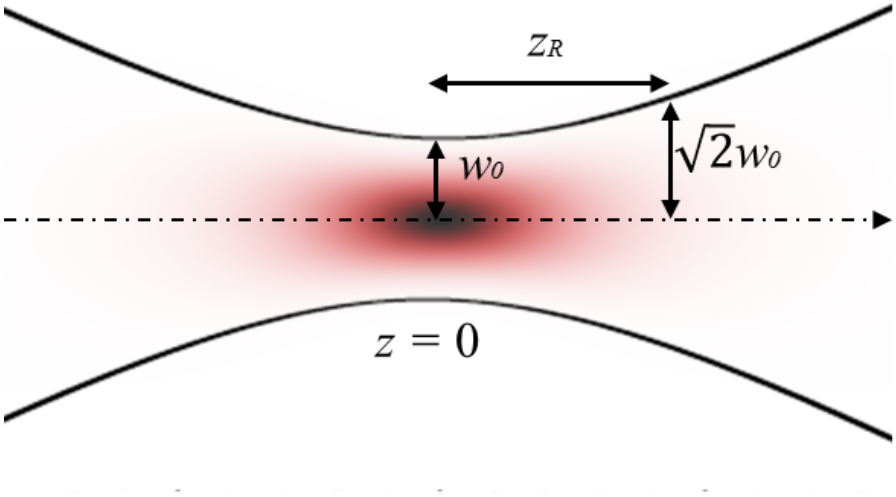

Figure 1.1: The Gaussian propagation parameters; The waist, at $z = 0$, has radius w_0. The distance at which the beam has spread to double the area at the waist is the Rayleigh range, z_R.

The transverse intensity of a Gaussian beam is displayed in Fig. 1.2 (b). The intensity has a Gaussian distribution, with the maximum occurring at $r = 0$ and decreasing monotonically with an increase in r, clearly seen in Fig. 1.2(a).

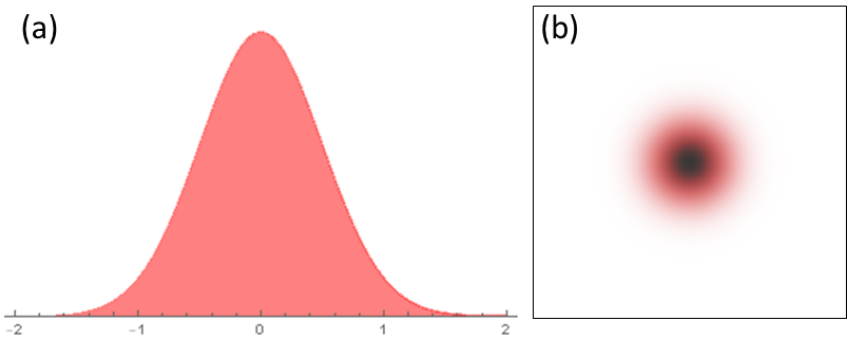

Figure 1.2: (a) Transverse intensity profile and (b) cross-sectional intensity profile of a Gaussian beam.

1.4 Higher-order Gaussian beams

1.4.1 Standard Gaussian beams

Hermite-Gaussian (HG) and Laguerre-Gaussian (LG) beams are higher-order solutions of the paraxial wave equation that are separable in Cartesian and cylindrical coordinates, respectively. Standard HG beam mode and LG beam mode are the eigenmodes of this equation, in which the Gaussian part has a complex argument while the Hermite or Laguerre part is real [4].

The complex field amplitude of the HG mode is given in cartesian coordinates by [4]

$$u_{m,n}(x,y,z) = \frac{w_0}{w(z)} H_m\left(\frac{\sqrt{2}x}{w(z)}\right) H_n\left(\frac{\sqrt{2}y}{w(z)}\right) \exp\left(\frac{-(x^2+y^2)}{w^2(z)}\right) \times \exp\left(i\frac{k(x^2+y^2)}{2R(z)}\right) \exp(-i\Phi(m,n,z)) \tag{1.19}$$

$w(z)$ and $R(z)$ are defined as for the Gaussian beam and $\Phi(m,n,z)$ is the Gouy phase for the HG mode given by $\Phi(m,n,z) = (m+n+1)\arctan(z/z_R)$. H_m and H_n are Hermite polynomials. The indices m and n are the transverse electric field distribution mode index in the horizontal and vertical direction, respectively.

The transverse intensity profiles of the HG beam for various values of m and n is exhibited in Fig. 1.3. The lowest beam mode is the Gaussian beam when $m = n = 0$.

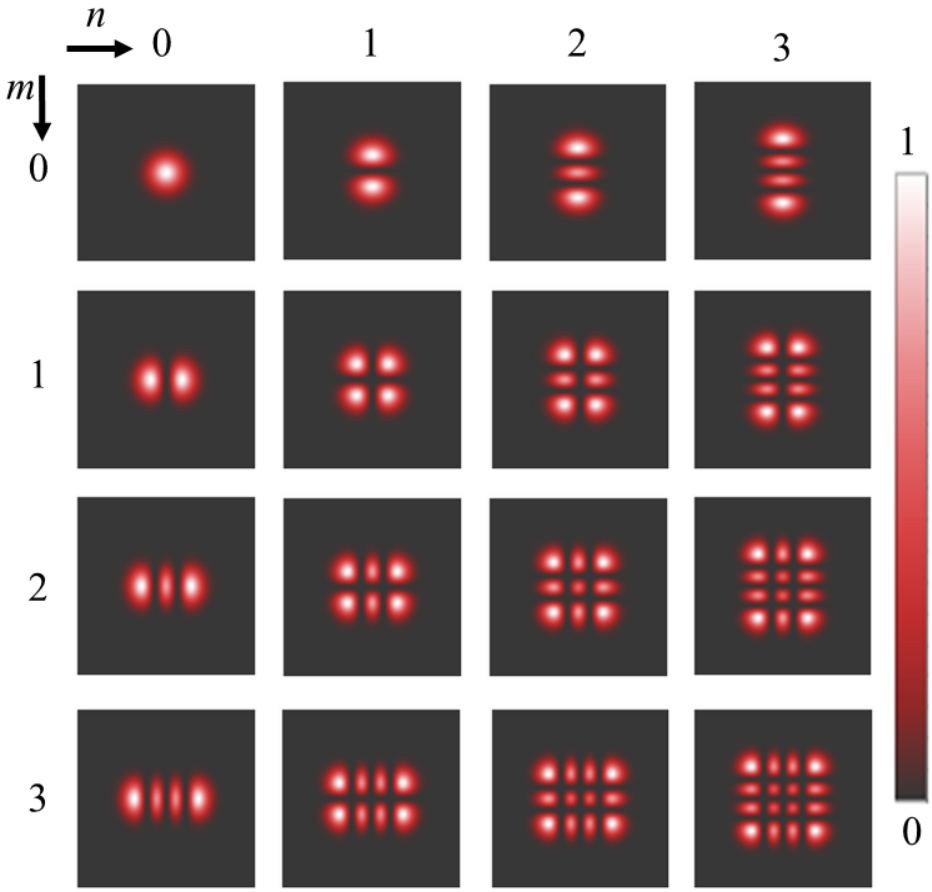

Figure 1.3: Transverse intensity profiles of higher order Hermite Gaussian beams with different mode indices.

The complex field amplitude of the LG mode is given in cylindrical coordinates by [4]

$$u_{p,l}(r,\theta,z) = \frac{1}{w(z)}\sqrt{\frac{2p!}{\pi(|l|+p)!}}\left(\frac{\sqrt{2}r}{w(z)}\right)^{|l|}\exp\left(\frac{-r^2}{w^2(z)}\right)L_p^{|l|}\left(\frac{2r^2}{w^2(z)}\right) \times \exp\left(i\frac{kr^2}{2R(z)}\right)\exp(il\theta)\exp(-i\Phi(p,l,z)) \tag{1.20}$$

$w(z)$ and $R(z)$ are defined as for the Gaussian beam and $\Phi(p,l,z) = (2p+l+1)\arctan(z/z_R)$ is the Gouy phase for the LG mode. $L_p^{|l|}$ is the Laguerre polynomial.

The LG modes are characterized by two indices l and p corresponding to the azimuthal and radial indices respectively. $u_{l,p}$ has a central dark spot,whos radius increases with

increasing l, and p dark nodal rings.

Examples of the LG beams intensity profiles are plotted in Fig. 1.4. The lowest beam mode is the Gaussian beam when $p = l = 0$.

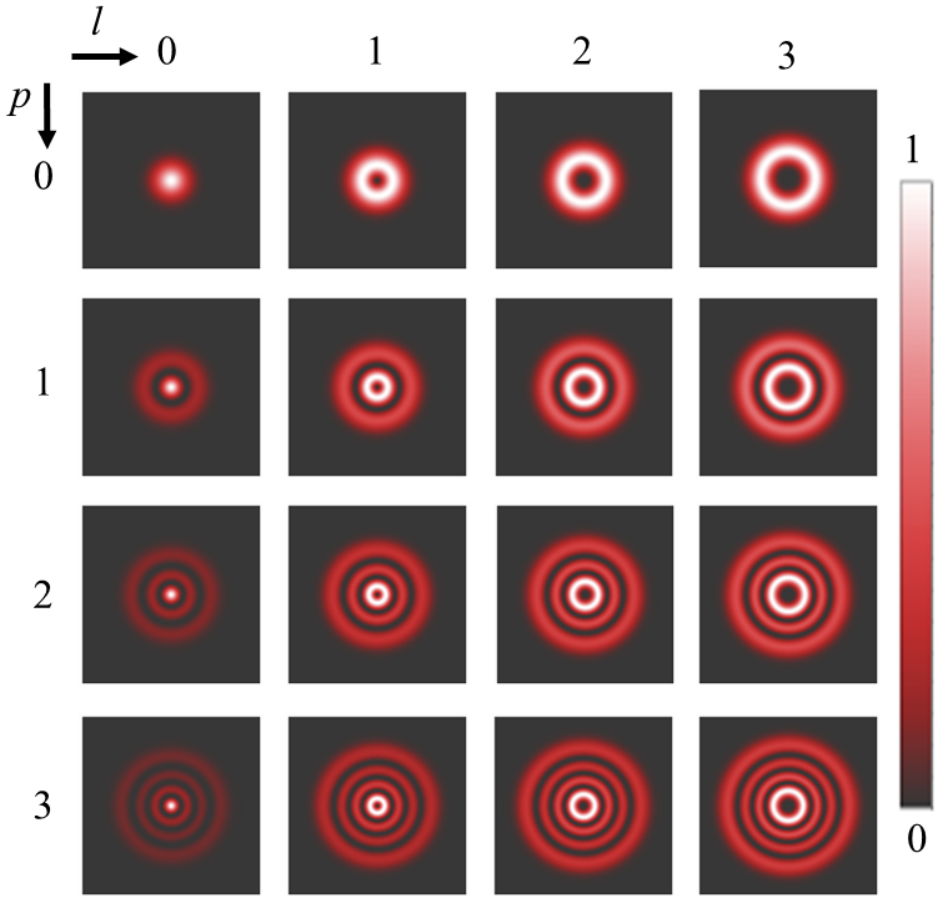

Figure 1.4: Transverse intensity profiles of higher order Laguerre Gaussian beams with different radial and azimuthal mode indices.

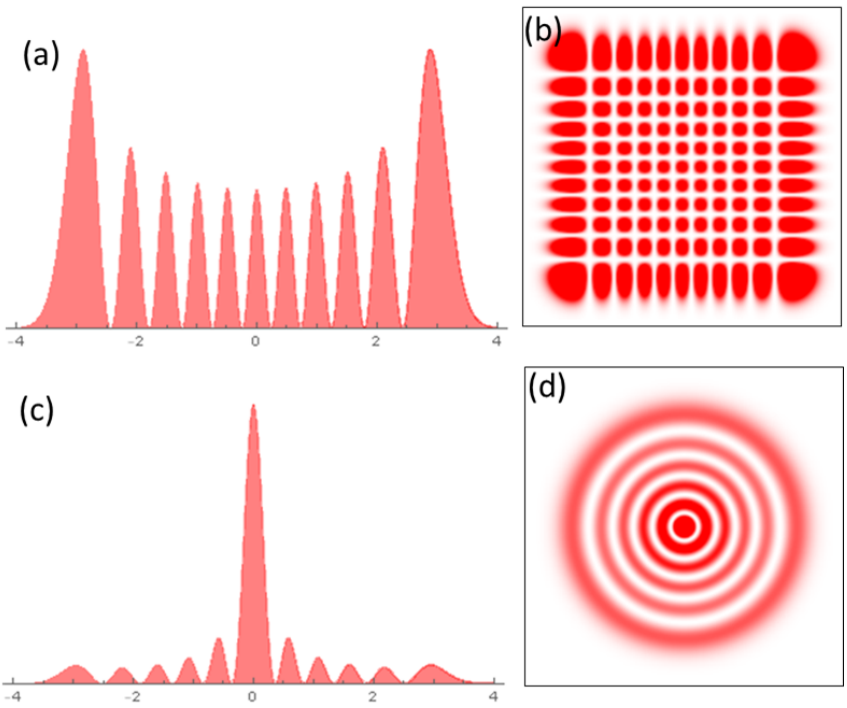

Figure 1.5: (a, c) Cross-sectional profile and (b, d) transverse profile of intensity of (a, b) a Hermite Gaussian beam ($n = m = 10$) and (c, d) a Laguerre Gaussian beam ($p = 5, l = 0$).

1.4.2 Elegant Gaussian beams

Alongside the well-known solutions of standard Hermite and Laguerre Gaussian beams, elegant Gaussian beams have been introduced, with a more symmetrical form, as alternative solutions to the paraxial wave equation [5–7]. In the elegant version, both the Gaussian function and Hermite or Laguerre polynomials have a complex argument, in contrast to the standard version, leading the transverse beam profile to change during the propagation.

The following Fig. 1.6 presents an exemple of the cross-sectional (Fig. 1.6 (a, c)) and transverse intensity profiles (Fig. 1.6 (b, d)) for the elegant HG beam of order $m = n = 10$ in Fig. 1.6 (a,b) and the elegant LG beam of order $p = 5$, $l = 0$ in Fig. 1.6 (c, d) .

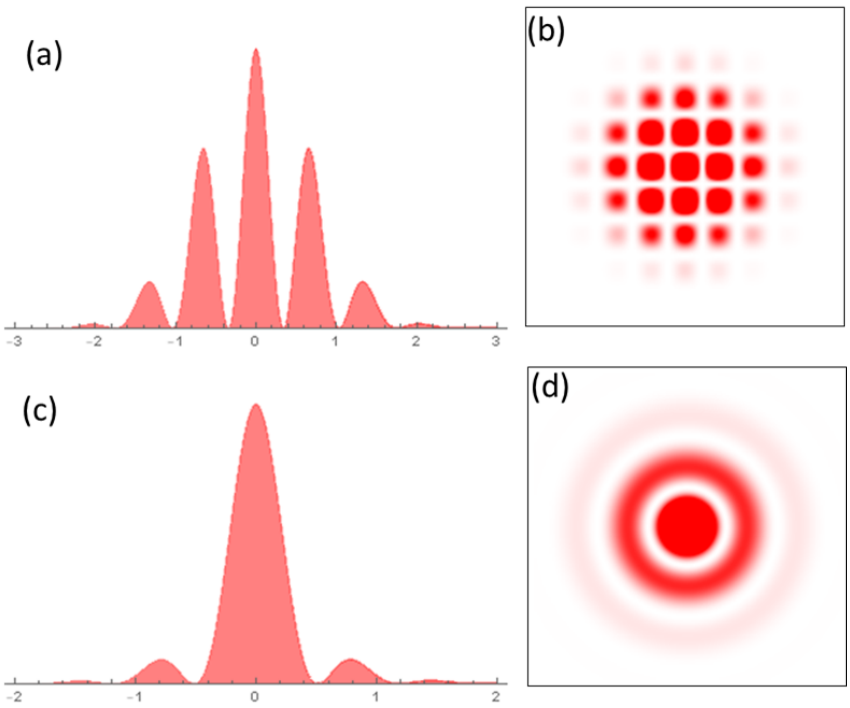

Figure 1.6: (a, c) Cross-sectional profile and (b, d) transverse profile of intensity of (a, b) an elegant HG beam ($n = m = 10$) and (c, d) an elegant LG beam ($p = 5, l = 0$).

1.4.3 Free-diffraction beams

Free-diffraction beams or non-diffracting beams, whose transverse intensity profile and scale remain unchanged in the longitudinal direction, are also solutions to the Helmholtz wave equation.

Ideal non-diffracting beams carry an infinite energy and their transverse intensity remains constant from $-\infty$ to $+\infty$, thus they cannot be exactly realized. For that reason, a modified version of the non-diffracting beams by adding a Gaussian factor, known as pseudo-nondiffracting beams, has been introduced, which can be realized experimentally to a very good approximation with the same properties of the idealized version over some finite region (finite power).

One of the simplest solutions, in circular cylindrical coordinates, is the Bessel Gauss (BG) beam, which is in the form of a Bessel function enveloped by a Gaussian profile. Its field

is described as [8]

$$u(r,\theta,z) = \frac{w_0}{w(z)} \exp\left[\left(\frac{-1}{w^2(z)} + \frac{ik}{2R(z)}\right)\left(r^2 + \frac{k_r^2 z^2}{k^2}\right)\right] J_l\left(\frac{k_r r}{(iz/z_R)}\right) \times \exp\left[iz\left(k - \frac{k_r^2}{2k}\right) + il\theta - i\Phi(z)\right] \tag{1.21}$$

Another pseudo-nondiffracting solution in Cartesian coordinates is the cosine-Gauss (CG) field, given by [9]

$$u(y,z) = \cos(k_y y) \exp\left(\frac{-y^2}{w^2(z)}\right) \exp(-ik_z z) \tag{1.22}$$

J_l is the l^{th}-order Bessel function, k_r (k_y) and k_z are the transverse and longitudinal wave-vectors and w_0 is the initial beam waist. The parameters $w(z)$, z_R, $R(z)$ and $\Phi(z)$ have the same definition as for those presented above. The propagation constant k and the parameters k_r and k_z are related by $k^2 = k_r^2 + k_z^2$.

The cross-sectional (Fig. 1.7 (a, c)) and transverse intensity profiles (Fig. 1.7 (b, d)) of the BG beam and the CG beam are illustrated in Fig. 1.7 (a,b) and Fig. 1.7 (c, d), respectively.

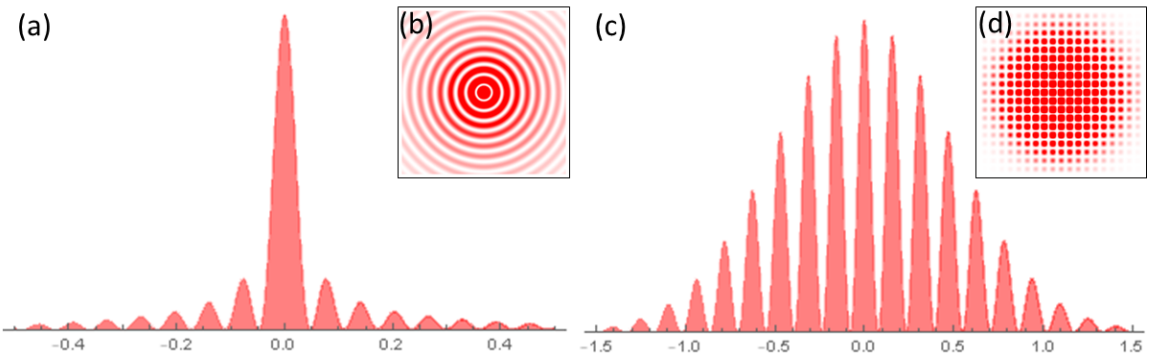

Figure 1.7: (a, c) Cross-sectional profile and (b, d) transverse profile of intensity of (a, b) a Bessel Gaussian beam and (c, d) a Cosine Gaussian beam.

1.5 Spatial Light Modulator (SLM)

The SLMs [10–12] are opto-electronic devices that impose a transverse spatial modulation, as the name implies, on a beam of light using either phase, amplitude, or both. Such a device, which implements liquid crystal (LC) technology for the construction of digital holograms, is a pixelated display formed by several hundreds of thousands of individual liquid crystal filled cells that can be controlled independently. The advantage of these devices is the ease of using it, where they can be controlled by a computer using appropriate programs. A computer generated grey-level images (holograms) are used to engineer arbitary light fields digitally. There are two distinct types of SLMs; an optically addressed and an electrically addressed SLM. The image in the latter, which was used in our case, is created and altered electronically, where the input is typically received from a VGA (Video Graphics Array) or DVI (Digital Video Interface) input.

The liquid crystal display (LCD), which is the crucial component in the SLM of our case, composes of 2D-array of spacing pixels. This little spacing makes the LCD operates as a 2D grating, leading the light to be diffracted into many orders.
As with any tool, the SLM users face efficiency problems due to its LCD structure. This latter causes loss of a part in the illuminated light (the absorbed part by the space between pixels so the incident beam doesn't all diffracted), where the quality of the diffracted order (the first order) is affected because of its overlap with the un-diffracted one (the zero order). In order to overcome this problem, a grating is added onto the computer-generated hologram so as to separate the diffracted from un-diffracted order and avoid the interference between the two components. This grating might be a blazed grating (a linear phase ramp) that makes 100% of the light is diffracted into the desired order or sinusoidal grating, which diffract light almost evenly across all orders[10–12] .

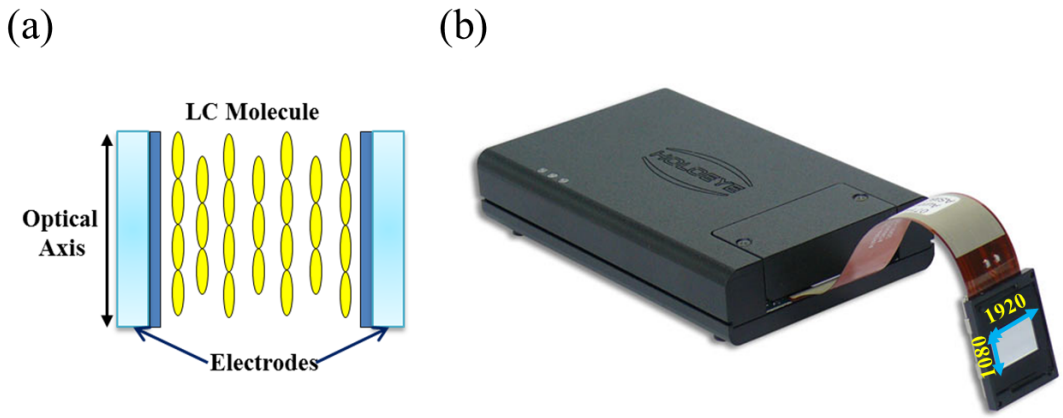

Figure 1.8: (a) Illustration of an individual pixel in the liquid crystal display. The pixel (liquid crystal filled cell) is electrically adjusted with an applied voltage. (b) Holoeye SLM. The number of pixels is determined by the resolution of the SLM screen.

1.5.1 Digital holograms

The generation of any arbitrary complex optical field is based on the use of computer-generated holograms displayed by the SLM.

Consider an incoming optical field, written in terms of amplitude and phase, $u_1(x) = u_a(x)\exp(i\phi_1(x))$, will be transformed into a new field, say $u_2(x) = u_b(x)\exp(i\phi_2(x))$. The optical element executing this change have a transfer function [12] , given by

$$T = \frac{u_2(x)}{u_1(x)} = \frac{u_b(x)}{u_a(x)}\exp[i(\phi_2(x) - \phi_1(x))] \tag{1.23}$$

where x denotes the transverse spatial coordinates that could be $(x,\ y)$ for Cartesian coordinates or $(r,\ \theta)$ for cylindrical coordinates.

Phase-only holograms

When $u_a(x) = u_b(x)$, the amplitude term of the transmission function is 1, indicating that only the phase of the incoming beam is altered whilst leaving the original amplitude

untouched. The SLM applies the following transmission function to the incoming field u_1,

$$T(x) = \exp(i\Psi(x)) \tag{1.24}$$

where $\Psi = \phi_2 - \phi_1$ is the phase screen that we display on the SLM.

For phase-only modulation, we need to look at the far-field to obtain the desired modulated field $(u_1(x) \cdot T(x))$, which is most easily accomplished by looking at the focal plane of a lens.

Complex amplitude holograms

The used SLM in the experimental work found in this thesis is a phase-only device, (1.8), while the studied beam field, experimentally, has both amplitude and phase terms; Thus requiring complex amplitude modulation to convert one beam's amplitude and phase into that of another (convert from a phase-only device response to full amplitude-phase response).

The complex amplitude modulation using a phase-only SLM is proposed by Arrizón et al. in [13]. The idea is to encode amplitude information in a phase screen, where it be a function of the desired beam's amplitude and phase, as follows

$$T(x) = \exp(i\Psi(A, \psi)) = A(x)\exp(i\psi(x)) \tag{1.25}$$

where $A(x) \in [0, 1]$ and $\psi(x) \in [-\pi, \pi]$.

The encoded phase modulation $\Psi(A, \psi)$ is determined from the following ansatz $\Psi(A, \psi) = f(A)\sin(\psi)$, where the function $f(A)$ is obtained by numerical inversion of $J_1[f(A)] = 0.58A$ with J_1 is the first-order Bessel function. This technique allows the generation of modes with purity higher than 0.96 as demonstrated by Ando et al. in [14].

As opposed to phase-only modulation where the desired field is obtained at the far-field, in complex amplitude modulation the desired field is created at the plane of the SLM screen.

Chapter 2

Characterizing the diffraction of the Laguerre-Gauss beams by an aperture and an opaque disk

The present chapter contains extracts from a publication by *Chabou et al* [15].

2.1 Introduction

The natural phenomenon that occurs when the waves encounter obstacles is called diffraction defined as the bending of waves around the edges of an obstacle. Spatial characteristics of the diffraction pattern depend on the incident wave field, as well as on the geometry, the kind, and the size of the obstacle.

In this chapter, we will describe the diffraction properties of LG beams passing through two kinds of circular obstructions; an aperture, in which the outer part of the beam is blocked, and an opaque disk, in which the central part of the beam is blocked, based on two key parameters; the focal shift effect and the beam propagation factor M^2. The focal shift phenomenon occurs when an optical beam is focused by a lens, or truncated by an obstacle, and the usual geometric focal plane shifts toward the incoming beam, where the

amount of this shift is strongly related to the focusing lens or to the obstacle size [16–21]. While the M^2 factor is strongly related to aberrations and diffraction effects [22–31] which in turn affects the overall propagation characteristics of the beam. We will perform a full theoretical and experimental study, by measuring transverse and axial intensities, focal plane shifts, beam radius and beam quality factor M^2, where we will demonstrate that the type of obstruction significantly influences the beam's features. Furthermore, we will demonstrate that the diffraction of LG beams by an opaque disk can reveal an interesting feature, which is the self-healing ability that will be explained by borrowing concepts from image analysis, not usually associated with self-healing of structured light.

2.2 LG beam diffraction

In this section, we introduce the studied optical system for describing the diffracted LG beams, outline the concept of the self-healing property, and the concept that we present to evaluate this property, which is the spatial filtering (Abbe experiment).

In order to examine the effect of the aperture and the opaque disk on the LG beam propagation, we simulated the optical system shown in Figure 2.1. In which, we are interested in the propagation of the beam after the lens, particularly at the Fourier plane ($z = f$), and the so-called shifted plane at $z = z_0$.

In this chapter, the shifted plane is defined as the plane corresponding to the position of minimum beam width, that is, the waist position of the distorted beam. Both planes are shown in Figure 2.1 as dashed vertical lines.

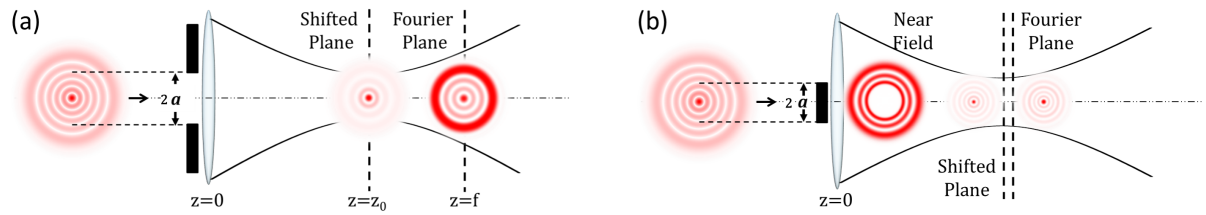

Figure 2.1: Schematic Conceptualizing the diffraction of radial LG beam by (a) an aperture and (b) an opaque disk, and then focused with a lens. The incident beam is partially blocked at the lens plane ($z = 0$) by an obstruction of some radius, selected to coincide with the zeros of the initial beam. The output beam is investigated both at the geometrical focal plane (Fourier plane) of the lens and at the shifted focal plane (shifted plane in short), which corresponds to the plane where the second moment width of the output beam is minimum.

The electric field of an incident LG beam of radial index p and azimuthal index l can be written in the cylindrical coordinates, at its waist $z = 0$, as

$$u_{in}(r,\theta,z=0) = \frac{1}{w(z)}\sqrt{\frac{2p!}{\pi(|l|+p)!}}\left(\frac{\sqrt{2}r}{w(z)}\right)^{|l|}\exp\left(\frac{-r^2}{w^2(z)}\right)L_p^{|l|}\left(\frac{2r^2}{w^2(z)}\right)\exp(il\theta) \quad (2.1)$$

where $w^2(z) = w_0^2[1+(z/z_R)^2]$ is the beam width, $z_R = \pi w_0^2/\lambda$ is the Rayleigh length, w_0 is the Gaussian waist radius, and L_p^l is a Laguerre polynomial of order p and l. We visualize the radial LG beam (of radial index p and azimuthal index $l = 0$) bypass two obstructions, which are with a circular structure, characterized by transmittance functions

$$\tau_{AP}(r) = \begin{cases} 1 & r \le a \\ 0 & r > a \end{cases}, \quad (2.2)$$

and

$$\tau_{OD}(r) = \begin{cases} 0 & r \le a \\ 1 & r > a \end{cases}, \quad (2.3)$$

with a the radius of the obstruction for the aperture (AP) and opaque disk (OD), respec-

tively. In the case of the aperture, a corresponds to the radius of the hole, and in the case of the opaque disk, to the radius of the obstruction itself.
In all our study cases, radii were chosen to coincide with the zeros of the beam's intensity with the aim to keep the disturbance of spatial frequencies to a minimum, acting as a filter for some predetermined number of rings, or equivalently, some predetermined spatial frequencies.

From the Fresnel-Kirchhoff diffraction theory, the propagated electric field at a distance z is given by [32]

$$u_{out}(\xi,\eta,z) = \left(\frac{1}{i\lambda z}\right)^{1/2} \exp(ikz) \int_{-\infty}^{+\infty}\int_{-\infty}^{+\infty} u_{in}(x,y,z=0) \exp\left[\frac{ik}{2z}\left((\xi-x)^2+(\eta-y)^2\right)\right] dxdy. \tag{2.4}$$

By setting $x = r\cos\theta$, $y = r\sin\theta$, $\xi = \rho\cos\phi$, $\eta = \rho\sin\phi$; Eq. 2.4 becomes

$$u_{out}(\rho,\phi,z) = \frac{1}{i\lambda z} \exp(ikz) \int_{0}^{\infty}\int_{0}^{2\pi} u_{in}(r,\theta,z=0) \exp\left[\frac{ik}{2z}\left(\rho^2+r^2-2\rho r\cos(\theta-\phi)\right)\right] rdrd\theta. \tag{2.5}$$

Using the following integral formula [33, 34]

$$\int_0^{2\pi} \exp\left[\frac{ik}{z}\rho r\cos(\theta-\phi)\right] \exp(-il\theta)d\theta = 2\pi J_0\left(\frac{k}{z}\rho r\right)\exp(-il\phi) \tag{2.6}$$

with $k = 2\pi/\lambda$ and J_0 is the Bessel function of order zero.

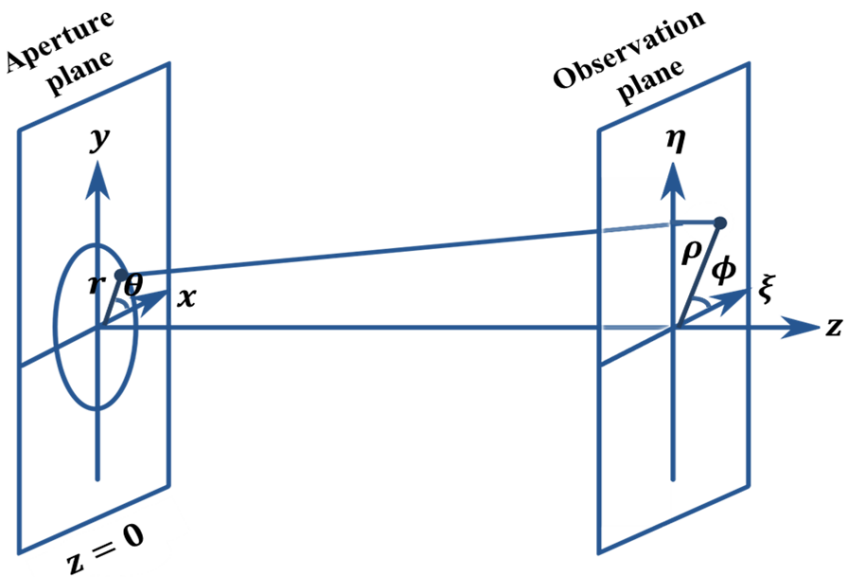

Figure 2.2: Diffraction geometry, showing the object plane and the image plane.

The propagation of the studied LG beam at a distance z in cylindrical coordinates system can be given by

$$u_{out}(\rho, z) = \frac{i2\pi}{\lambda z} \exp\left(i\frac{2\pi}{\lambda}\left(z + \frac{\rho^2}{2z}\right)\right) \int_0^\infty u_{in}(r, z=0)\tau(r) J_0\left(\frac{2\pi}{\lambda z}\rho r\right) \exp\left[\frac{i\pi r^2}{\lambda}\left(\frac{1}{z} - \frac{1}{f}\right)\right] r dr, \tag{2.7}$$

where ρ is the radial distance to the propagation axis. $\exp(-ikr^2/2f)$ is the transmittance function of the lens, with f is the focal length of the lens.

Figure 2.3 shows density plots in the ξz-plane of the propagated beam for unobstructed (Figure 2.3a), obstructed by an aperture (Figure 2.3b) and obstructed by an opaque disk (Figure 2.3c). The vertical axis corresponds to the transverse ξ-axis, normalized to the beam's Gaussian waist (w_0), while the horizontal axis is the propagation z-axis, normalized to the focal length, f. For all images, the Fourier plane is marked by a vertical blue dotted line. Figure 2.3 presents on the bottom the transverse cross-sections at the shifted plane $z = z_0$, where the unobstructed beam is shown in black and the obstructed one in red. By comparing Figures. 2.3b and c to Fig. 2.3a, it can be seen that while the beam

shape and width are significantly affected by the aperture, the beam is barely modified by the opaque disk at the shifted plane. This is further illustrated in the intensity profiles, where it is seen that the beam recovers its shape only when obstructed by an opaque disk. This indicates clearly that the type of obstruction greatly influences the effect it has on the beam.

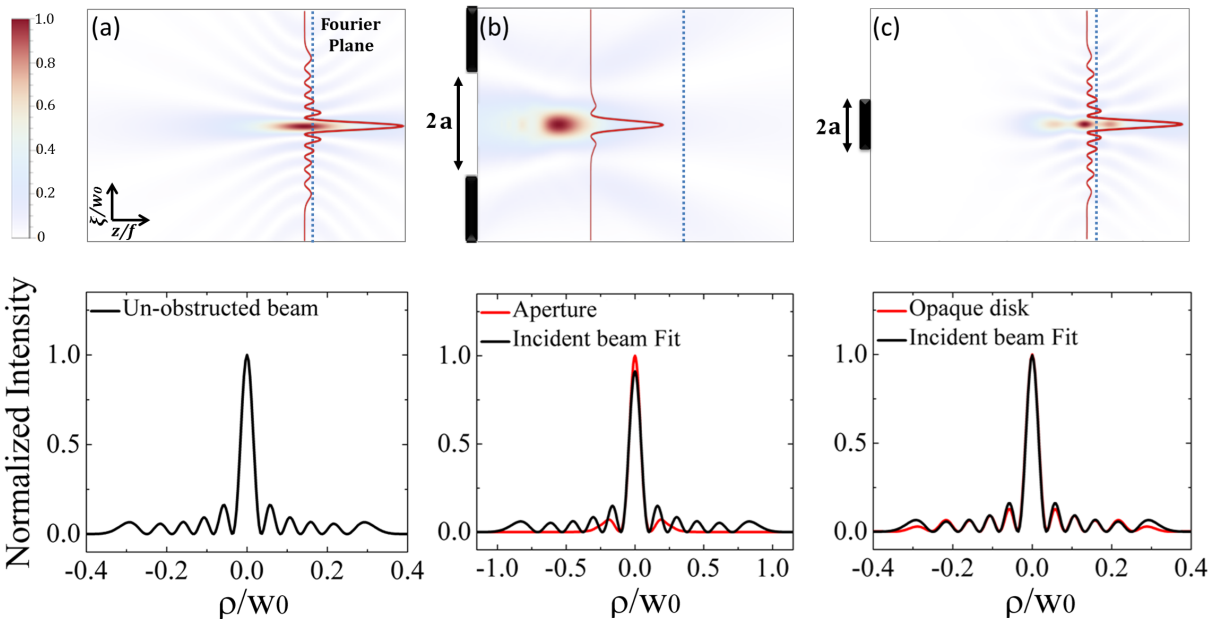

Figure 2.3: Numerical simulation for an LG_{50} beam. Density plots in the ξz-plane (top row) and profiles along the ξ-axis (bottom row) of the intensity distribution of the beam for (a) an unobstructed beam, the beam after passing through (b) an aperture, and (c) an opaque disk.

2.3 Self-healing concept

One of the most fascinating properties of diffraction-free optical fields is their ability to reconstruct if they are partially obstructed in their propagation path, both classically and in the quantum regime. In this section, we introduce an overview of the concept behind the self-healing process.

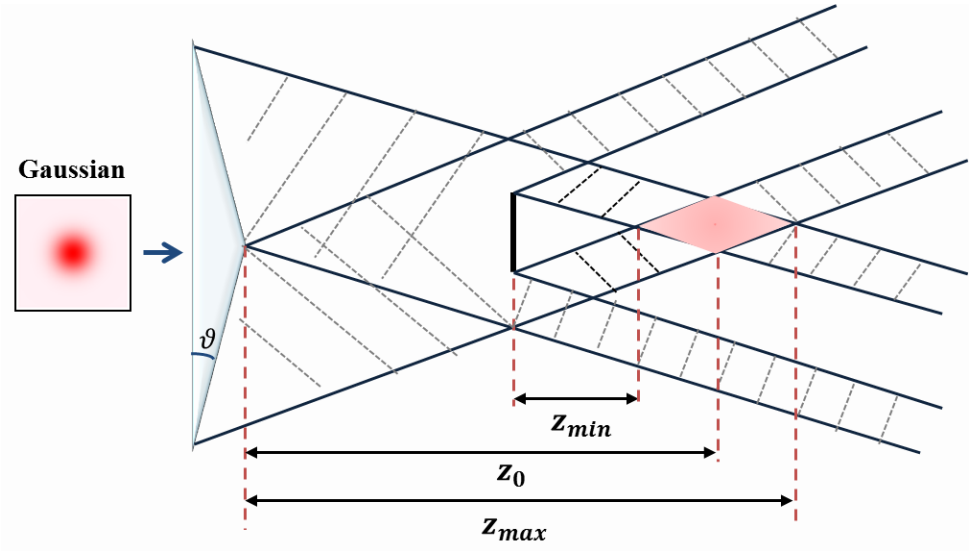

Figure 2.4: Self-healing principle of BG beams. Conical waves, that formed by refracting plane waves incident on axicon, form a BG beam in the region z_{max}. An opaque obstruction placed at$1/2z_{max}$ blocks a part of waves while allowing the other part (unblocked waves) to interfere at a short distance behind the obstruction, i.e., after z_{min}. The region where the beam is predicted to self-heal totally is the plane z_0.

The self-healing ability has been explained as the interference of unobstructed conical waves [35, 36]. The mechanism underlying this process is simple and can be seen in Figure. 2.4. In which the conical waves bypass the obstruction producing a shadow region, after this region the conical waves that missed the obstruction (not affected by the obstruction) overlap, and by interference reconstruct the original Bessel beam, albeit it with less power and over a limited range in both the transverse and propagation planes.

Self-healing has been long time considered as a distinctive feature of nondiffracting beams [37]; most prominently of Bessel beams [38–41], although also Airy [42], caustic [43], and Mathieu and Weber [44] beams have been examined. It was subsequently realized that some diffracting beams, including the whole family of scaled propagation invariant beams [45], as well as angular self-healing of orbital angular momentum(OAM) beams [46], polarization self-healing of vector beams [47, 48], and even the recovery of entanglement in quantum states [49, 50], can self-reconstruct.

There is a good reason for the extensive studies that persist even today: self-healing

beams have used in a variety of applications including multiple plane micro-manipulation [51], robust optical communication [52], reduced scattering in imaging microscopy [53], enhanced laser machining [54] and quantum key distribution through obstacles [49, 50].

In this chapter, our study reveals the LG beam ability to self-heal, where we adopt the beam profile and the beam spatial characteristics (beam propagation factor and focal shift effect) to evaluate this ability. As well as introducing its physical interpretation based on spatial frequency filtering following Abbe.

2.4 Abbe experiment and spatial filtering

In this section, we outline a well-known concept in optics, which is spatial filtering, in order to qualitatively explain the physics behind the self-healing of LG beams. The spatial filtering [55, 56] was done almost one hundred years ago by Ernst Abbe's when he performed his famous experiments in support of his Fourier theory of image formation, Figure 2.5, where he found that the resolution of the image depends on the number of spatial frequencies that are passed through the imaging system [57]. Based on this, in the image processing context, it is conventionally to perform spatial filtering by removing specific frequency ranges (blocking the components of a diffraction pattern at the transform plane). For instance, a low-pass filter will reduce high-frequency noise and has an overall "smoothing" effect, while a high-pass filter will emphasize fine details in the image and enhance edges.

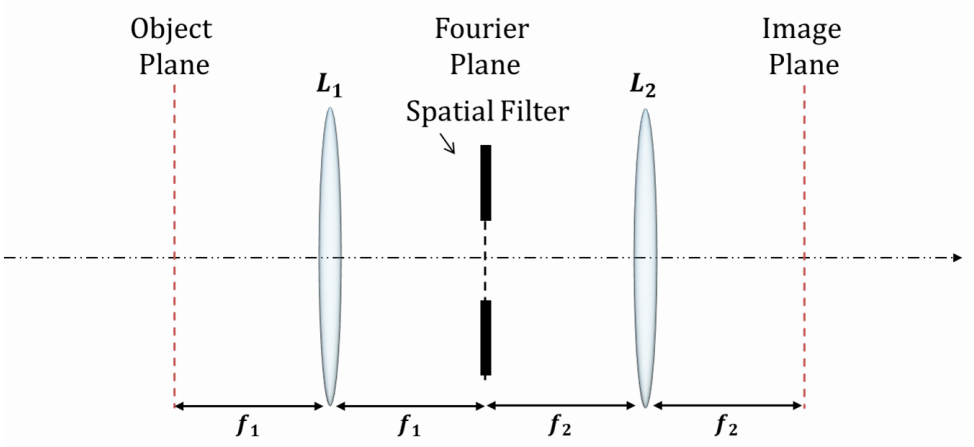

Figure 2.5: Spatial filtering. $4f$ optical imaging system perform a Fourier transform followed by an inverse Fourier transform. The Fourier components of the object are separated by the first lens into spatial fraquencies at the Fourier plane. The object Fourier transformed is multiplied by the transmittance of the spatial filter, then the second lens reconstructs the image (inverse Fourier transform of the filtred version).

We now consider this in the context of complex light rather than imaging. The spatial filtering process allows us to hypothesize that the most of the beam's information is found in the high-frequency content, that is, in the outermost region. This implies that removing this spatial frequency content will have a stronger effect on the beam in comparison to removing the lower frequency content. In other words, an obstruction of the higher frequencies (an aperture) will have a severe impact on the beam, while obstruction of the lower frequencies (an opaque disk) will have less of an effect. This is precisely the behavior we observe in the numerical simulations in Figure 2.3.

2.5 Experimental realisation of diffracted LG beams

An established and ubiquitous tool for the realization of complex beams that have been introduced in the previous chapter is spatial light modulators (SLMs). Our experimental realization of an LG beam involved encoding on the SLM a hologram of the following

form

$$\Psi_{SLM} = f_{LG} \sin(\psi_{LG} + G_x X + G_y Y) \tag{2.8}$$

Where f_{LG} is obtained by numerical evaluation as

$$J_1[f_{LG}] = A_{LG} \tag{2.9}$$

with A_{LG} and ψ_{LG} are the amplitude and the phase, respectively, of LG beam as follows

$$A_{LG} = \frac{1}{w(z)} \sqrt{\frac{2p!}{\pi(|l|+p)!}} \left(\frac{\sqrt{2}r}{w(z)}\right)^{|l|} \exp\left(\frac{-r^2}{w^2(z)}\right) L_p^{|l|}\left(\frac{2r^2}{w^2(z)}\right) \tag{2.10}$$

$$\psi_{LG} = \exp\left(i\frac{kr^2}{2R(z)}\right) \exp(il\theta) \exp\left(-i(2p+|l|+1)\arctan\left(z/z_R\right)\right) \tag{2.11}$$

J_1 the first order Bessel function. $G = 1/L$ is the grating frequency, where L is the grating period (in the x and y directions).

It's worth noting that for encoding this hologram we use a blazed grating, $\exp(i2\pi G_x x)$, so that the desired beam is generated in the first diffraction order of the grating[58]. Besides the generation of LG beams, the SLM can also be used for the realization of any chosen kind of obstacle (aperture and opaque disk an our case) of defined radius a in the $z = 0$ plane. Examples of the encoded image onto the SLM is shown in Figure 2.6, the two first row, which was incorporated into the experimental set up as described in Figure 2.7.

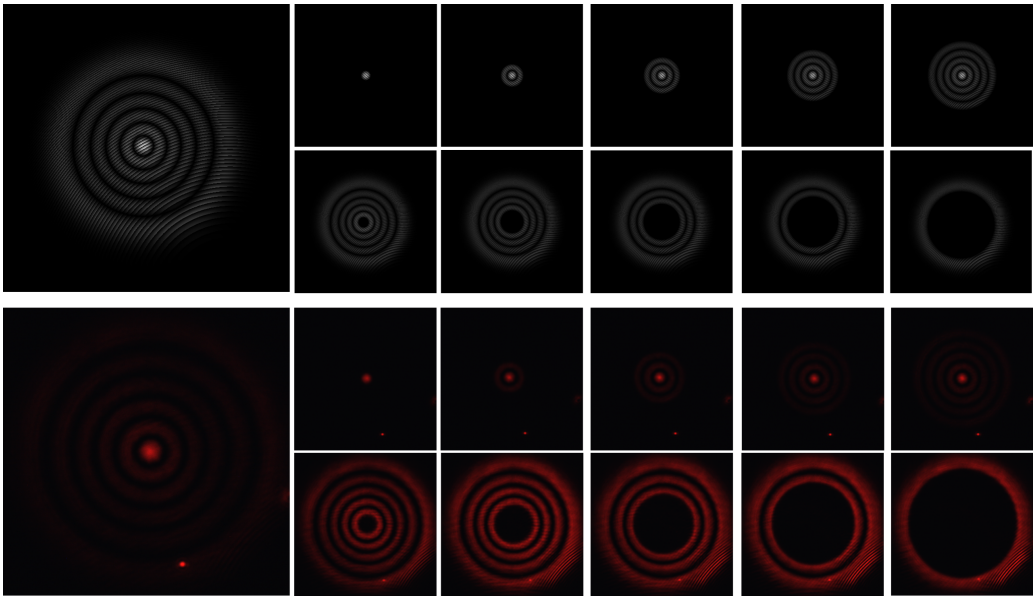

Figure 2.6: Holograms encoded on the SLM (top) and experimental intensity profiles (bottom) of Laguerre-Gaussian beam of order $p = 5$. The first column presents the unobstructed case, the first and third row show the obstruction case by an aperture, and the second and fourth row show the obstruction case by an opaque disk.

Figure 2.7 is a schematic representation of the experimental setup used to confirm the numerical predictions. Light from a He-Ne laser operating at a wavelength of $\lambda = 632.8$ nm was expanded and collimated using a telescope (lenses L1, $f_1 = 50$ mm, and L2, $f_2 = 500$ mm) for illumination of a phase-only spatial light modulator (SLM - HOLOEYE PLUTO) displaying a computer-generated hologram (CGH). The CGHs were created by complex amplitude modulation [11, 12], as referred above, and designed to simultaneously encode the LG beam, the lens ($f = 250$ mm) and the obstruction (aperture or opaque disk). A 4f system (lenses L3, $f_3 = 250$ mm, and L4, $f_4 = 250$ mm) imaged the SLM plane to the back focal plane of lens L4, and simultaneously filtered out unwanted diffraction orders with an iris at the Fourier plane of L3. Finally, a CCD camera (Point Grey Firefly) was mounted onto a guiding rail along the propagation axis to obtain a series of images of the beam intensity at different propagation distances. Crucially, encoding the lens into the hologram enabled us to measure the beam intensity near $z = 0$ without any physical limitation.

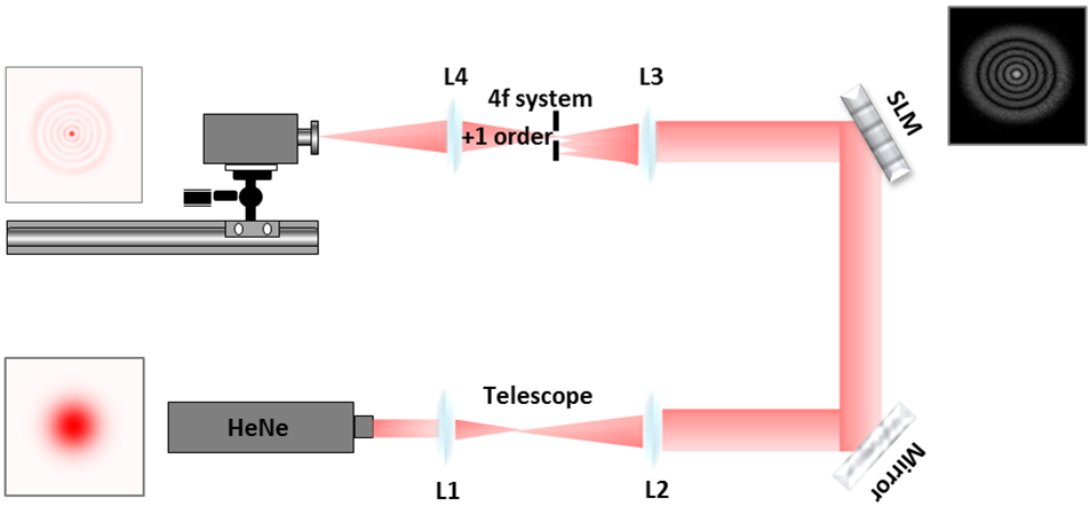

Figure 2.7: Schematic of the experimental setup used to study the diffraction of an LG beam ($p = 5$) by an aperture or an opaque disk. The SLM simultaneously generates the obstructed beam and encodes the lens.

2.6 Experimental results versus numerical simulations

2.6.1 Diffraction patterns

In order to study the diffraction behavior of LG beams, illustrative examples of the intensity patterns and their profiles for the obstructed LG beam of order $p = 5$ are presented in this section.

With the aim of having a reference point to compare the obstructed beams against, we start by showing the beam intensity of the unobstructed beam at the shifted (Figure 2.8 (a)) and Fourier (Figure 2.8 (b)) planes. It can be seen they are very similar, since, in this particular case, the above-mentioned planes are very near to each other (Figure 2.3 (a)).

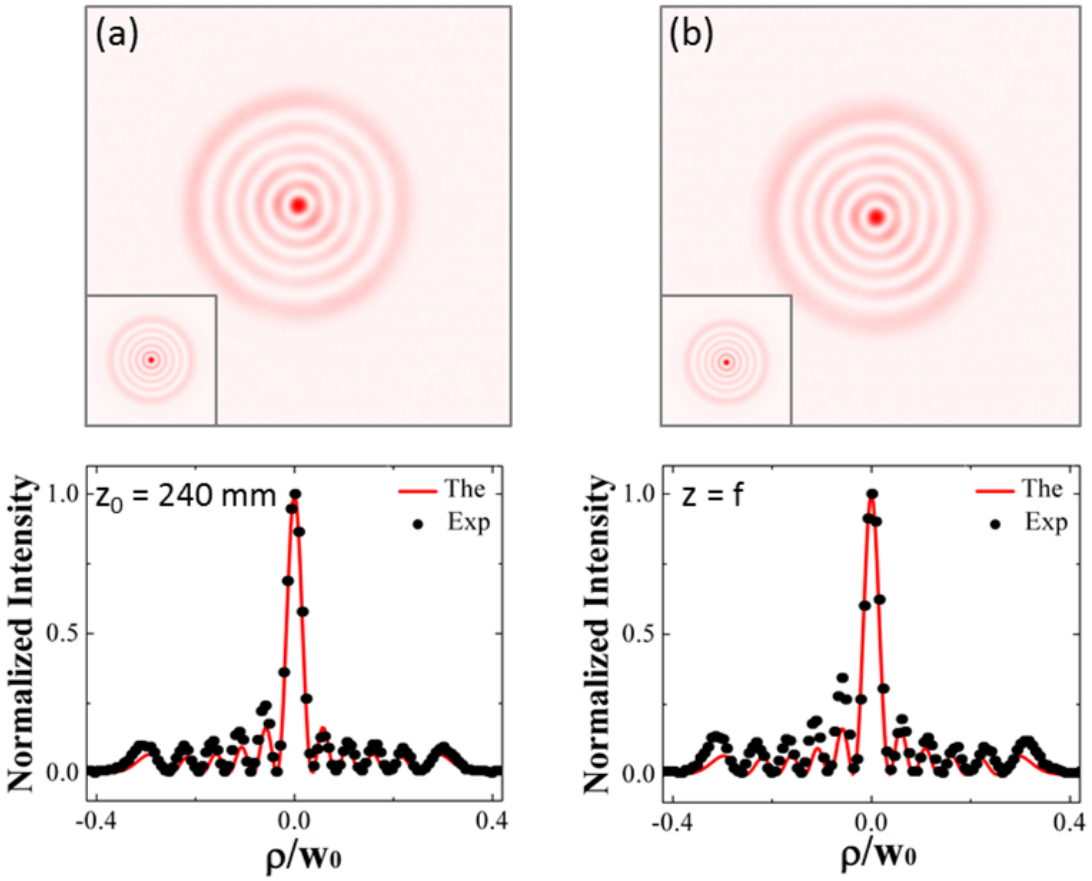

Figure 2.8: Experimental and theoretical (insets) intensity patterns and the corresponding cross-sectional profiles for non-obstructed LG beam of order $p = 5$, at (a) the shifted plane and (b) the geometric focal plane (Fourier plane).

We begin with an LG beam of order $p = 5$ as an illustrative example and consider the diffraction patterns evolution to examine the beam's self-healing ability. The experimental results for the aperture are shown in Figure 2.9 at both the shifted (top row) and Fourier (bottom row) planes, for three different aperture radii. It is worth noting that the position of the shifted plane strongly depends on the aperture size, therefore the specific value for z_0 is different for each case. The insets show the corresponding theoretical predictions to experimental measurements. While below each image we show the cross-sectional intensity profile.

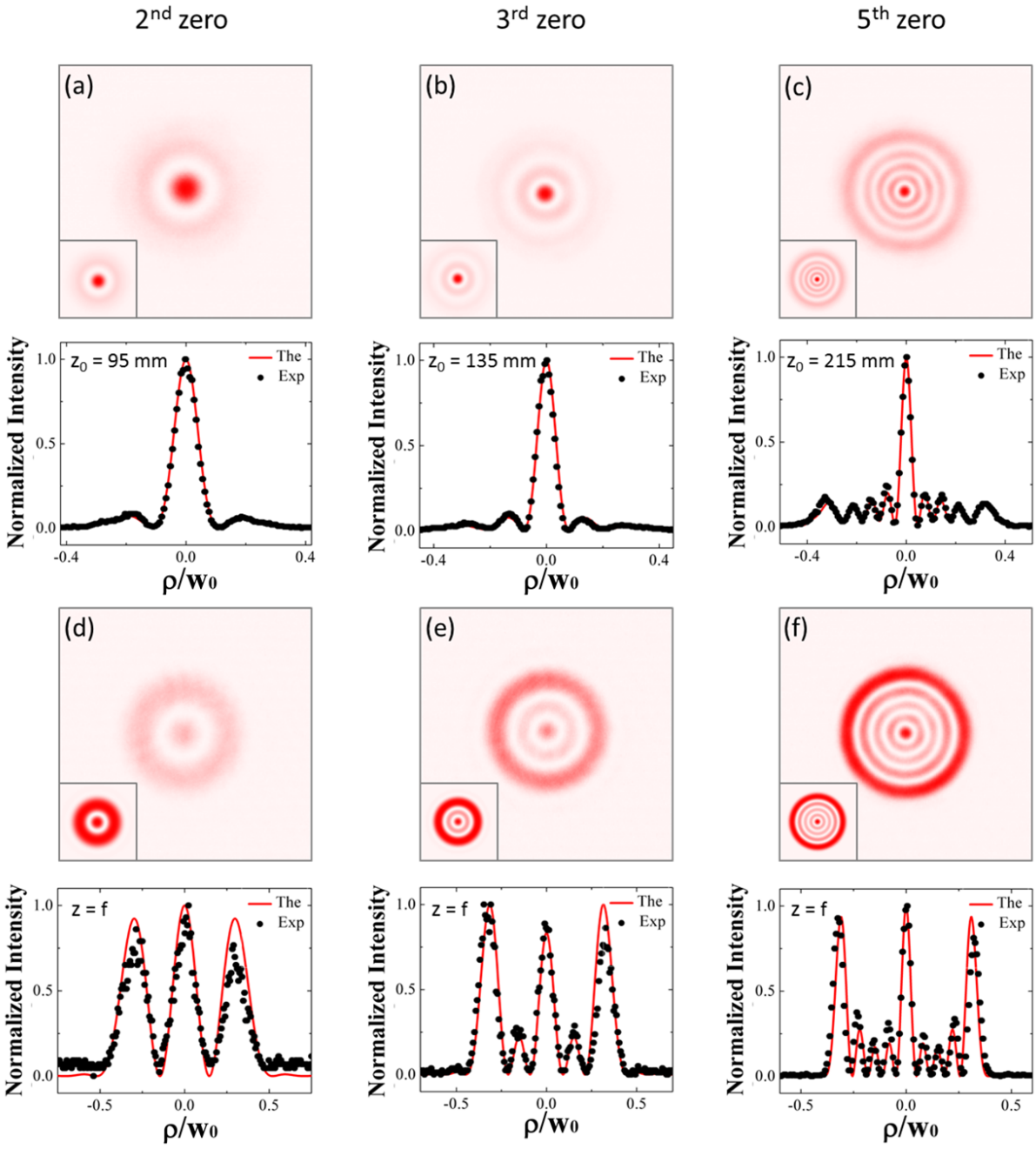

Figure 2.9: Experimental and theoretical (insets) intensity patterns (top) and the corresponding cross-sectional profiles (bottom) for an obstructed LG_{50} beam by an aperture, on (a), (d) its second intensity zero, (b), (e) third intensity zero, and (c), (f) fifth intensity zero, at the shifted plane (a), (b) and (c) and at the Fourier plane (d), (e) and (f).

One notices that the obstructed intensity patterns differ from the unobstructed ones, particularly when a large portion of the beam is blocked. The beam never recovers its initial profile at any plane, even in the far field, revealing that the beam does not self-heal

after it is blocked by an aperture.

In contrast to this is the more conventional case of obstruction by an opaque disk, with experimental results shown in Figure 2.10. The intensity distributions are shown at a plane just after the opaque disk $z = 10$ mm, and at the shifted plane $z = z_0$; note that for these beam parameters the Fourier plane and the shifted plane are very close and therefore their intensity patterns are almost identical, hence we only show the intensity at the shifted plane. As before, we used an LG beam of order $p = 5$ and the opaque disks blocked the beam up to its second, third and fifth intensity zeros (counting from the beam's center). Figures 2.10 (a)-(c) clearly show the effect of the opaque disk on the beam in the near-field, in such a way that the inner rings disappear as the disk radius increases, as one would expect. On the other hand, comparing the unobstructed beam from Figure 2.8 against the blocked beam in Figures. 2.10 (d)-(f), it can be seen that the the blocked part is reconstructed at the shifted plane in all examples. The reconstruction is almost perfect in the first case, good in the second, and differences are more noticeable in the third. However, considering the extent of the obstruction in the latter case, it is remarkable how similar the propagated beam is to the unobstructed one at the shifted plane.

As it is well-known, it is worth noting that it has been point out in many previous works [35, 59] that the distance of the self-healing process depends on the opaque disk size, which means that the quality of the reconstructed beam in the second and the third case will be better after the shifted plane when the self-healing process is completed.

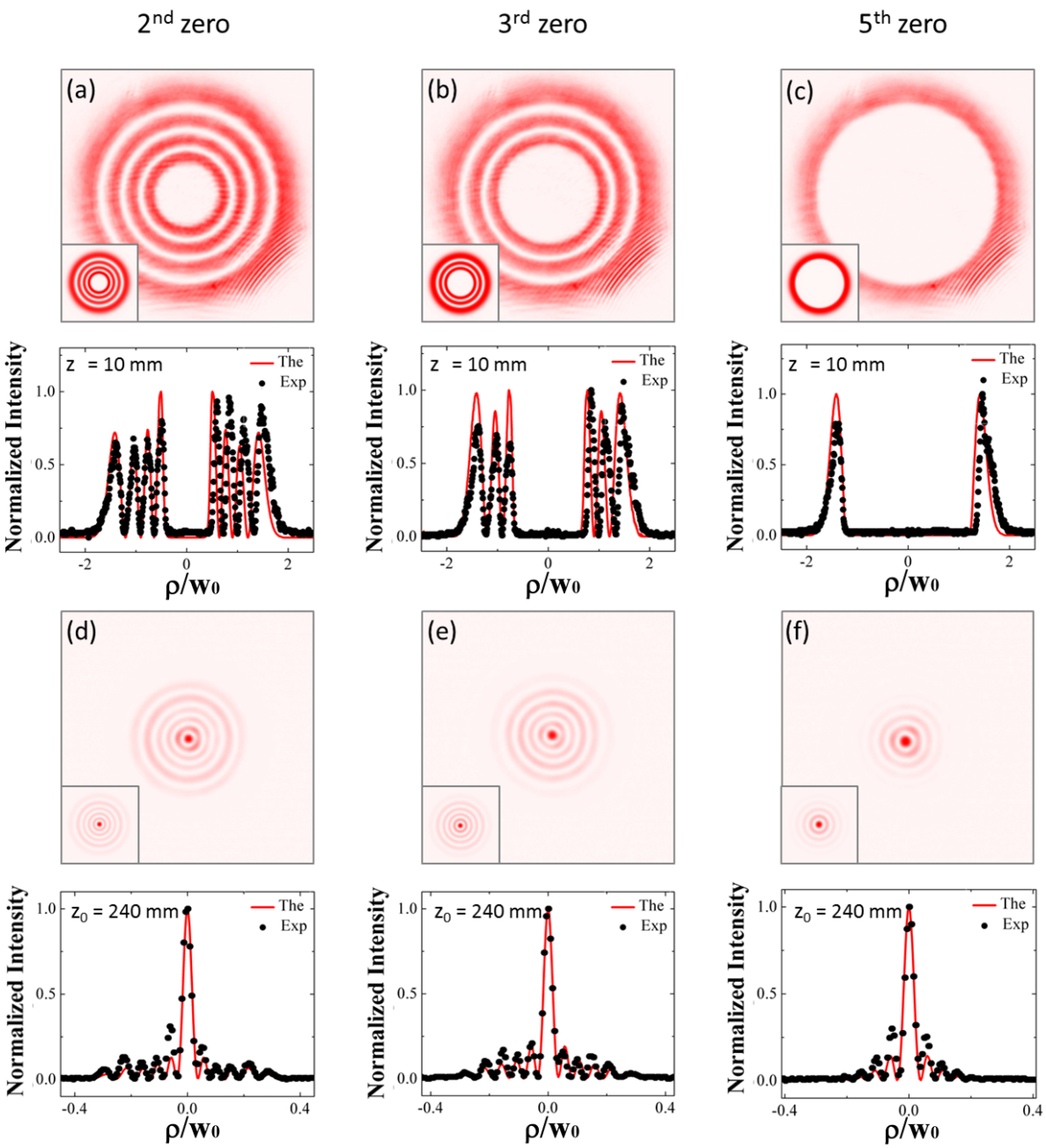

Figure 2.10: Experimental and theoretical (insets) intensity patterns (top) and associated cross-sectional profiles (bottom) for an obstructed LG_{50} beam by an opaque disk, on (a), (d) its second intensity zero, (b), (e) third intensity zero, and (c), (f) fifth intensity zero, at the near field $z = 10$ mm (a), (b) and (c) and at the shifted plane (d), (e) and (f).

To quantify the diffraction patterns evolution in terms of reconstruction degree, we measure the similarity, which has been used extensively in the context of self-healing Bessel

beams [59], between the behavior of the un-obstructed LG beam of radial index p = 5 and the behavior of the obstructed one along the propagation path. The optical fields of the beam with and without obstruction are denoted by $u_1(\xi, \eta, z)$ and $u_2(\xi, \eta, z)$, respectively. In Hilbert space $u_1(\xi, \eta, z)$ and $u_2(\xi, \eta, z)$ can be considered as two infinite-dimensional complex vectors. The angle between the two infinite-dimensional complex vectors is described mathematically as the division between their inner product and the product of the norm, which is the length, of each one.

$$\cos(u_1, u_2) = \frac{(u_1, u_2)}{||u_1||||u_2||}, \tag{2.12}$$

with $(u_1, u_2) = \int\int u_1(\xi, \eta, z)u_2^*(\xi, \eta, z)d\xi d\eta$ and $||u|| = \sqrt{\int\int u(\xi, \eta, z)u^*(\xi, \eta, z)d\xi d\eta}$. u^* denotes the complex conjugate of u.

The used similarity, named S, in this study can be defined as

$$S = \cos(|u_1|, |u_2|) = \frac{(|u_1|, |u_2|)}{||u_1||||u_2||} = \frac{\int_0^\infty u_{1out}(\rho, z)u_{2out}^*(\rho, z)\rho d\rho}{\sqrt{\int_0^\infty u_{1out}(\rho, z)u_{1out}^*(\rho, z)\rho d\rho}\sqrt{\int_0^\infty u_{2out}(\rho, z)u_{2out}^*(\rho, z)\rho d\rho}}, \tag{2.13}$$

Numerical simulations of Eq. 2.13 are shown in Figure 2.11, where the similarity of both apertured and blocked LG_{50} beams are plotted at the plane $z = z_0$, corresponding to the shifted plane of the unobstructed beam as a function of obstacle sizes. As seen from Figure 2.11, the similarity degree for the blocked beam at the plane $z = z_0$ decreases as the opaque disk size increases. While the similarity degree for the apertured beam at the same plane ($z = z_0$) increases with increasing of the aperture size.

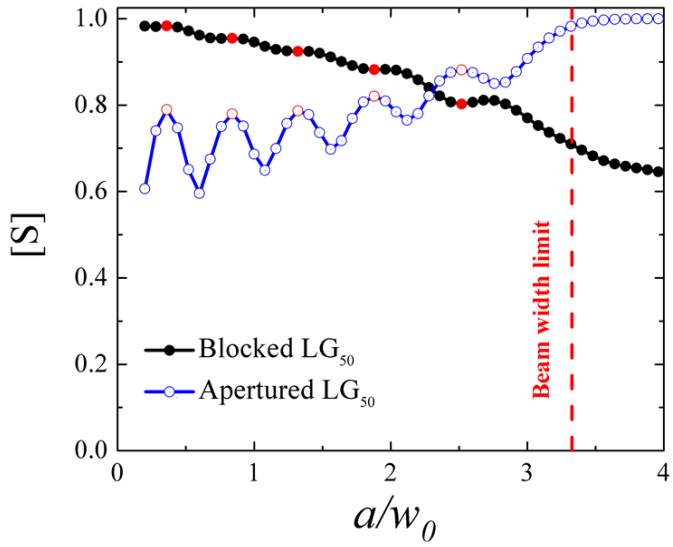

Figure 2.11: Similarity, S, of both blocked (opaque disk) and apertured LG_{50} beams as a function of the normalized obstruction size, a/w_0. The red dots indicate the positions of the intensity zeros of the LG_{50} beam.

2.6.2 Diffraction spatial characteristics (beam propagation factor and the focal shift effect)

This section provides a deep quantitative analysis of the obstructed LG beams performance, specifically the self-healing, through two important parameters are the beam propagation factor, M^2, and focal shift.

The M^2 factor, sometimes called the beam quality factor or beam propagation factor, is one of the most common parameters describing the overall propagation features of a laser beam, encompassing both the beam width and its divergence, which in turn can be used to define the brightness of the beam, and how tightly it might be focused. It is easily calculated as [60, 61]

$$M^2 = \frac{\pi}{\lambda} w_\rho \theta_\rho \tag{2.14}$$

where the beam width, w_ρ, and divergence, θ_ρ, are defined as second moments of the

intensity [62, 63]:

$$\langle w_\rho^2 \rangle = \frac{2\pi}{P_0} \int_0^\infty \tau(r) |u_{in}(r,0)|^2 r^3 dr \,, \tag{2.15}$$

$$\langle \theta_\rho^2 \rangle = \frac{2\pi}{k^2 P_0} \int_0^\infty \tau(r) |u'_{in}(r,0)|^2 r dr + \frac{32\pi}{3k^2 P_0} |u_{in}(a,0)|^2 \,, \tag{2.16}$$

where P_0 is the total power contained in the beam

$$P_0 = 2\pi \int_0^\infty \tau(r) |u_{in}(r,0)|^2 r dr \,, \tag{2.17}$$

and $u'_{in}(r,0)$ is the first derivative of the amplitude $u_{in}(r,0)$ of the LG beam at plane $z = 0$, given by

$$\begin{aligned} |u'_{in}(r,0)|^2 =& \frac{2}{w_0^2} \sum_{b_1=0}^{p} \sum_{b_2=0}^{p} (-1)^{b_1+b_2} \frac{(p!)^2}{(p-b_1)!(p-b_2)!(b_1!)^2(b_2!)^2} \\ & \left(\left(2\frac{r^2}{w_0^2} \right)^2 - 2(b_1+b_2) \left(2\frac{r^2}{w_0^2} \right) + 4b_1 b_2 \right) \left(2\frac{r^2}{w_0^2} \right)^{b_1+b_2-1} \exp\left(-2\frac{r^2}{w_0^2} \right), \end{aligned} \tag{2.18}$$

Using the following integral formulae, and the series expansion of Laguerre function [64]

$$\int_0^a x^\nu \exp(-sx) dx = \frac{\nu!}{s^{\nu+1}} - \exp(-as) \sum_{h=0}^{\nu} \frac{\nu!}{h!} \frac{a^h}{s^{\nu-h+1}} \tag{2.19}$$

$$L_p \left(2\frac{r^2}{w_0^2} \right) = \sum_{b=0}^{p} (-1)^b \frac{p!}{(p-b)!(b!)^2} \left(2\frac{r^2}{w_0^2} \right)^b \tag{2.20}$$

After tedious integral calculations, Eq. 2.15, which corresponds to the beam width, be-

comes

$$\begin{aligned}\langle w_\rho^2\rangle =&\frac{w_0^4\pi}{2P_0}\sum_{b_1=0}^{p}\sum_{b_2=0}^{p} g(b_1,b_2,p)\left(\exp(-2\delta_1^2)\sum_{h=0}^{N+1}\frac{(N+1)!}{h!}(2\delta_1^2)^h-\right.\\ &\left.\exp(-2\delta_2^2)\sum_{h=0}^{N+1}\frac{(N+1)!}{h!}(2\delta_2^2)^h\right),\end{aligned} \tag{2.21}$$

And Eq. 2.16 that corresponds to the divergence, becomes

$$\begin{aligned}\langle\theta_\rho^2\rangle =&\frac{2\pi}{k^2P_0}\sum_{b_1=0}^{p}\sum_{b_2=0}^{p} g(b_1,b_2,p)\left(\left(\exp(-2\delta_1^2)\sum_{h=0}^{N+1}\frac{(N+1)!}{h!}(2\delta_1^2)^h-\exp(-2\delta_2^2)\sum_{h=0}^{N+1}\frac{(N+1)!}{h!}(2\delta_2^2)^h\right)\right.\\ &-2N\left(\exp(-2\delta_1^2)\sum_{h=0}^{N}\frac{N!}{h!}(2\delta_1^2)^h-\exp(-2\delta_2^2)\sum_{h=0}^{N}\frac{N!}{h!}(2\delta_2^2)^h\right)+4b_1b_2\times\\ &\left(\exp(-2\delta_1^2)\sum_{h=0}^{N-1}\frac{(N-1)!}{h!}(2\delta_1^2)^h-\exp(-2\delta_2^2)\sum_{h=0}^{N-1}\frac{(N-1)!}{h!}(2\delta_2^2)^h\right)+\\ &\left.\left.\frac{16}{3}\left(\left(2(\delta_2^2-\delta_1^2)\right)^N\exp\left(-2(\delta_2^2-\delta_1^2)\right)\right)\right)\right),\end{aligned} \tag{2.22}$$

where the total power contained in the beam, P_0,

$$P_0=\pi w_0^2\sum_{b_1=0}^{p}\sum_{b_2=0}^{p} g(b_1,b_2,p)\left(\exp(-2\delta_1^2)\sum_{h=0}^{N}\frac{N!}{h!}(2\delta_1^2)^h-\exp(-2\delta_2^2)\sum_{h=0}^{N}\frac{N!}{h!}(2\delta_2^2)^h\right), \tag{2.23}$$

Based on Eqs. (2.14),(2.21), and (2.22), the analytical expression for the beam propagation factor M^2 of an LG beam diffracted by an annular aperture as a function of the beam

truncation parameters δ_1, δ_2 is given as follow

$$
\begin{aligned}
M^2 = &\left[\sum_{b_1=0}^{p}\sum_{b_2=0}^{p} g(b_1,b_2,p)\left(\exp(-2\delta_1^2)\sum_{h=0}^{N}\frac{N!}{h!}(2\delta_1^2)^h - \exp(-2\delta_2^2)\sum_{h=0}^{N}\frac{N!}{h!}(2\delta_2^2)^h\right)\right]^{-1}\times \\
&\left[\sum_{b_1=0}^{p}\sum_{b_2=0}^{p} g(b_1,b_2,p)\left(\exp(-2\delta_1^2)\sum_{h=0}^{N+1}\frac{(N+1)!}{h!}(2\delta_1^2)^h - \exp(-2\delta_2^2)\sum_{h=0}^{N+1}\frac{(N+1)!}{h!}(2\delta_2^2)^h\right)\right]^{\frac{1}{2}}\times \\
&\left[\sum_{b_1=0}^{p}\sum_{b_2=0}^{p} g(b_1,b_2,p)\left(\left(\exp(-2\delta_1^2)\sum_{h=0}^{N+1}\frac{(N+1)!}{h!}(2\delta_1^2)^h - \exp(-2\delta_2^2)\sum_{h=0}^{N+1}\frac{(N+1)!}{h!}(2\delta_2^2)^h\right)\right.\right. \\
&-2N\left(\exp(-2\delta_1^2)\sum_{h=0}^{N}\frac{N!}{h!}(2\delta_1^2)^h - \exp(-2\delta_2^2)\sum_{h=0}^{N}\frac{N!}{h!}(2\delta_2^2)^h\right) + 4b_1b_2\times \\
&\left(\exp(-2\delta_1^2)\sum_{h=0}^{N-1}\frac{(N-1)!}{h!}(2\delta_1^2)^h - \exp(-2\delta_2^2)\sum_{h=0}^{N-1}\frac{(N-1)!}{h!}(2\delta_2^2)^h\right) + \\
&\left.\left.\frac{16}{3}\left(\left(2(\delta_2^2-\delta_1^2)\right)^N\exp\left(-2(\delta_2^2-\delta_1^2)\right)\right)\right)\right]^{\frac{1}{2}}
\end{aligned}
\tag{2.24}
$$

where $g(b_1,b_2,p) = (-1)^{b_1+b_2}\left((p!)^2/(p-b_1)!(p-b_2)!(b_1!)^2(b_2!)^2\right)$, $\delta_1 = a_1/w_0$, and $\delta_2 = a_2/w_0$. $N = b_1 + b_2$.

For the extreme case (un-diffracted case) of $a_1 \to 0$ and $a_2 \to \infty$, Eq. 2.24 reduces

$$
\begin{aligned}
M^2 = &\left[\sum_{b_1=0}^{p}\sum_{b_2=0}^{p} g(b_1,b_2,p)N!\right]^{-1}\left[\sum_{b_1=0}^{p}\sum_{b_2=0}^{p} g(b_1,b_2,p)(N+1)!\right]^{\frac{1}{2}}\times \\
&\left[\sum_{b_1=0}^{p}\sum_{b_2=0}^{p} g(b_1,b_2,p)\left((N+1)! - 2NN! + 4b_1b_2(N-1)!\right)\right]^{\frac{1}{2}}
\end{aligned}
\tag{2.25}
$$

When $a_1 \to 0$, Eq. 2.24 reduces to the M^2 expression of the diffracted LG beam by a

circular aperture of radius a_2

$$
\begin{aligned}
M^2 = & \left[\sum_{b_1=0}^{p}\sum_{b_2=0}^{p} g(b_1,b_2,p)\left(N! - \exp(-2\delta_2^2)\sum_{h=0}^{N}\frac{N!}{h!}(2\delta_2^2)^h\right)\right]^{-1} \times \\
& \left[\sum_{b_1=0}^{p}\sum_{b_2=0}^{p} g(b_1,b_2,p)\left((N+1)! - \exp(-2\delta_2^2)\sum_{h=0}^{N+1}\frac{(N+1)!}{h!}(2\delta_2^2)^h\right)\right]^{\frac{1}{2}} \times \\
& \left[\sum_{b_1=0}^{p}\sum_{b_2=0}^{p} g(b_1,b_2,p)\left(\left((N+1)! - \exp(-2\delta_2^2)\sum_{h=0}^{N+1}\frac{(N+1)!}{h!}(2\delta_2^2)^h\right)\right.\right. \\
& -2N\left(N! - \exp(-2\delta_2^2)\sum_{h=0}^{N}\frac{N!}{h!}(2\delta_2^2)^h\right) + 4b_1b_2 \times \\
& \left.\left.\left((N-1)! - \exp(-2\delta_2^2)\sum_{h=0}^{N-1}\frac{(N-1)!}{h!}(2\delta_2^2)^h\right) + \frac{16}{3}\left(\left(2\delta_2^2\right)^N \exp\left(-2\delta_2^2\right)\right)\right)\right]^{\frac{1}{2}}
\end{aligned}
\tag{2.26}
$$

When $a_2 \to \infty$, Eq. 2.24 reduces to the M^2 expression of the diffracted LG beam by an opaque disk of radius a_1

$$
\begin{aligned}
M^2 = & \left[\sum_{b_1=0}^{p}\sum_{b_2=0}^{p} g(b_1,b_2,p)\left(\exp(-2\delta_1^2)\sum_{h=0}^{N}\frac{N!}{h!}(2\delta_1^2)^h\right)\right]^{-1} \times \\
& \left[\sum_{b_1=0}^{p}\sum_{b_2=0}^{p} g(b_1,b_2,p)\left(\exp(-2\delta_1^2)\sum_{h=0}^{N+1}\frac{(N+1)!}{h!}(2\delta_1^2)^h\right)\right]^{\frac{1}{2}} \times \\
& \left[\sum_{b_1=0}^{p}\sum_{b_2=0}^{p} g(b_1,b_2,p)\left(\left(\exp(-2\delta_1^2)\sum_{h=0}^{N+1}\frac{(N+1)!}{h!}(2\delta_1^2)^h\right)\right.\right. \\
& \left.\left.-2N\left(\exp(-2\delta_1^2)\sum_{h=0}^{N}\frac{N!}{h!}(2\delta_1^2)^h\right) + 4b_1b_2\left(\exp(-2\delta_1^2)\sum_{h=0}^{N-1}\frac{(N-1)!}{h!}(2\delta_1^2)^h\right)\right)\right]^{\frac{1}{2}}
\end{aligned}
\tag{2.27}
$$

On the other hand, the amount of the focal shift, which is mentioned above in the intro-

duction, can be given by :

$$\Delta z = f - z_0 \tag{2.28}$$

with f is the geometric focal length and z_0 denotes the shifted plane.

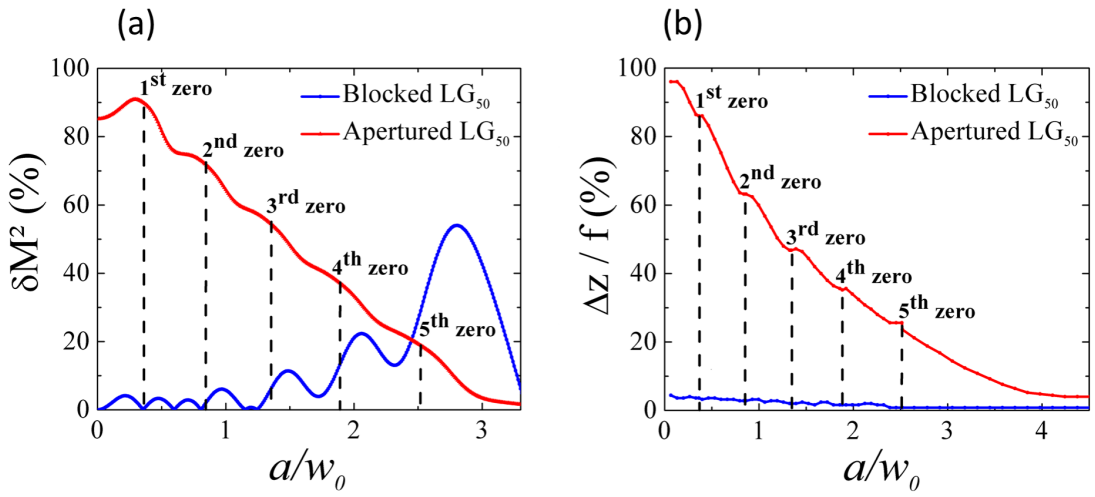

Figure 2.12: The percentage change in (a) the beam quality factor and (b) focal shift of the obstructed beam as compared to the unobstructed beam, calculated as a function of the normalized obstruction size for an aperture and an opaque disk (blocked). All calculations assumed an initial LG_{50} beam with an $M^2 = 2p + 1$.

Figure 2.12 shows numerical simulations for the percentage change in M^2, defined as $\delta M^2 = (M^2 - (2p+1))/(2p+1)$, and the percentage change in the focal shift, defined as $\Delta z/f = (z - z_0)/f$ for diffracted (apertured and blocked) LG_{50} beams as a function of the normalized obstruction parameter (the ratio of the obstacle size to the Gaussian waist, w_0). Not surprisingly, strongly apertured beams show a large change in M^2, decreases continuously until the aperture is open and the beam becomes unobstructed, where its propagation behavior is recovered. In contrast, the beam blocked by an opaque disk has an oscillatory response, with small changes near the zero's of the LG_{50} intensity. These results are supported by the equivalent focal shift curves, where the rate change of the focal shift for the blocked beam is negligible, while the rate change for the apertured beam is very high, confirming that the beam recovers against opaque disks but not against aper-

tures.

In order to confirm these theoretical results, we measure the full propagation of the field along the z-axis in order to extract the M^2 and the focal shift parameters. We illustrate one such example in Figure 2.13, measured for the test LG_{50} beam (apertured and blocked) on its third ring compared to the unobstructed one. From the experimental results we can extract the M^2 factor, the new waist location z_0 and the new waist size w_0 from [63, 65]:

$$w^2(z) = w_0^2 + M^4 \frac{\lambda^2}{\pi^2 w_0^2}(z - z_0)^2 \,. \tag{2.29}$$

Figure 2.13 shows the measured and simulated beam radii, normalized to the Gaussian beam width, as a function of propagation distance, z, normalized to the focal length, for an unobstructed beam (Figure 2.13a), an obstructed beam on its third intensity zero by an aperture (Figure 2.13b) and an opaque disk (Figure 2.13c). The predicted propagation is in agreement with the measured dynamics. The small difference ($\approx 15\%$) between the theoretical and experimental results in M^2 are likely due to the sensitivity of the second moment measurement to background noise. We see that the shifted planes of the unobstructed beam and the blocked beam by an opaque disk lie very close to the Fourier plane $z = f$, to within about 4%. However the apertured beam is significantly shifted. Specifically, the shifted plane of the obstructed beam by an aperture is located at a position somewhat close to the obstruction (aperture) plane. We can understand the physics of this by considering the Fresnel number, $F = a^2/\lambda f$, of the system. In the truncated case, the aperture limits the beam size so the Fresnel number changes with the aperture size, thus affecting the focal shift. However, for the blocked case with an opaque disk, the outer spatial beam extent remains unchanged and thus the Fresnel number remains unchanged. For that reason, the focal shift phenomenon in apertured beams is different from the traditional blocked cases studied yet.

These theoretical and experimental results confirm the ability of the LG beam to self-heal when encountering opaque disks but not when encountering apertures, where the LG beam self-heals if the opaque disk lets some light (rings) bypass the obstruction. By considering the outer rings as the higher spatial frequency components of the field, this result can be interpreted based on the spatial frequency filtering argument, that any high pass filtered image can be reconstructed by the interference of the remaining non filtered high frequencies. Or in the context of structured light that means there is enough information in the higher spatial frequencies to reconstruct the entire field.

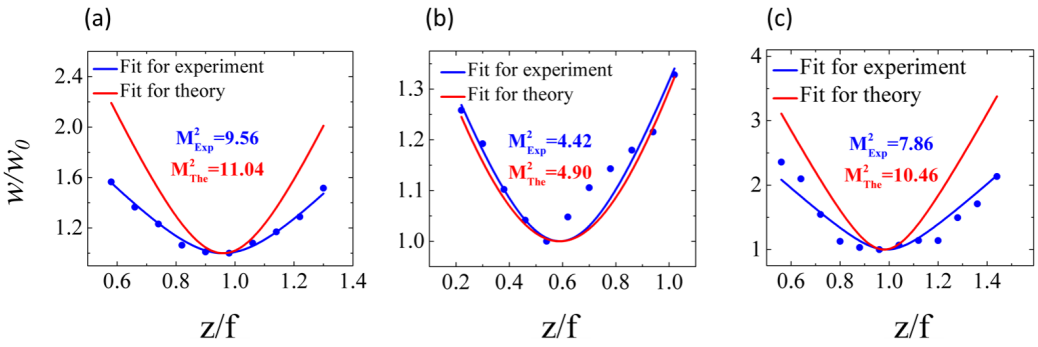

Figure 2.13: Theoretical and experimental beam radius as a function of normalized propagation distance for (a) unobstructed, and obstructed by (b) an aperture, and (c) an opaque disk. In all cases the initial beam was an LG_{50} obstructed at its third intensity zero. The measured and predicted M^2 values are given in the insets.

2.7 Conclusion

In this chapter, we have studied the diffraction spatial characteristics of radial LG beams, passing through two kinds of obstructions, that have shown the self-healing property of such beams. Our results have illustrated that the self-healing abilities of an LG beam are strongly dependent on the type of obstruction and less pronounced on its size. We have noticed that the LG beams are rather robust to the opaque disk radii, where attaining high-quality reconstruction even when a relatively large part of the beam is blocked. In

addition, we have demonstrated that the obstructed beam by an opaque disk keeps almost the same characteristics of the unobstructed beam, which was not the case when the beam is obstructed by an aperture. Altogether, our results have shown that the LG beam is more capable of self-healing when obstructed by an opaque disk than when blocked by an aperture.

Moreover and considering the nature of the obstacle from a high-pass filter to a low-pass filter, we have adopted an elegant way to interpret physically the diffraction behavior or rather the self-reconstruction of these beams based on the concept of spatial frequency filtering; considering the LG beams as images and the different rings of the beam as different spatial frequencies (since these beams are scaled propagation invariant). We have found that when the beam is blocked by an aperture, it loses its high-frequency information, and when it is blocked by an opaque disk, it losses its low-frequency information. Therefore, based on the spatial filtering concept, the beam is able to reconstruct itself only when its higher spatial frequency content is preserved.

Chapter 3

Modeling the diffraction of the Laguerre-Gauss beams by an aperture and an opaque disk

The current chapter contains extracts from a publication by *Bencheikh, Chabou, and Boumeddine* [66].

3.1 Introduction

The interest concerning LG beams, which are the eigenmodes of propagation where they propagate infinitely without changing their shape, is now rising rapidly thanks several modern applications especially in the field of optical trapping [67, 68], optical communication [69, 70], and quantum studies [71, 72].

In this chapter, we will provide, within certain conditions, a new analytical description for the far-field of the diffracted LG beams, that was characterized in the previous one. We will demonstrate that the Laguerre-Gaussian beams of order p (LGB_p) are asymptotically equivalent to the Bessel beams (BB) only in the inner multi-ring part. Thus, we will

suggest another beam, which is a sum of what we will call "ring shifted-Gaussian beams", that could replace its outer multi-ring part. Such peer-to-peer comparison of the LGB_p will help us to solve analytically the diffraction of such beams at the far-field, for which no exact analytical solution is known.

3.2 Comparison between Laguerre-Gauss beam and Bessel beam

In this section, we show the connection between the LG beam and BB based on the previous work of Mendoza-Hernández, Job, et al [73], where it has been demonstrated that they could be equivalent under some circumstances based on the asymptotic behavior of the Laguerre polynomial for higher-order p given as follows

$$\left(\frac{\sqrt{2}r}{w(z)}\right)^{|l|} L_p^{|l|}\left(\frac{2r^2}{w^2(z)}\right) e^{-r^2/w^2(z)} \approx \frac{\Gamma(p+|l|+1)}{p!(p+(|l|+1)/2)^{|l|/2}} \times J_l\left(2\sqrt{2p+|l|+1}\frac{r}{w(z)}\right). \tag{3.1}$$

where $\Gamma(.)$ is the gamma function and J_l is the Bessel function of order l. p and l are the radial and azimuthal indexes, respectively. The following study is limited only to radial modes, it means $l = 0$

Eq. (3.1) determines the relation between all main parameters of both beams; LGB and BB.

Figure 3.1 and Figure 3.2 displays, respectively, the transverse and the longitudinal intensity patterns, of an LGB and the corresponding BB for $(p, l) = (10, 0)$. It can be seen from Figure 3.1 (a), which shows the comparison of their 1D transverse intensity distributions,

that the transverse cross-sections of the two beams overlap only in the inner multi-ring part in contrast to the outer multi-ring part that behaves differently. Figures 3.1 (b) and (c) present the 3D intensity profiles of LGB and BB, respectively.

In contrast, in Figure 3.2(a), which shows the comparison of their on-axis intensity distributions, the LGB and its equivalent BB are significantly different. The ideal BB continues propagating as a nondiffracting beam for an important distance $z \geq 2z_R$, then it is transformed into a ringed beam in the far-field (as known from BB theory). While the LGB propagates as a scaled invariant beam, where it's keeping its on-axis intensity important for just one Rayleigh length z_R, then it continues propagating to infinity even with a small intensity. Figures 3.2(b) and (c), which present the propagation of LGB and BB, respectively, in the plane $\xi - z$, illustrate the difference in the longitudinal plane.

The obtained results led us to truncate both beams, the LGB as well as the BB, and examine their behavior. The second row in Figure 3.1 and Figure 3.2 depicts, respectively, the transverse and the longitudinal intensity patterns of the truncated two beams. It is evident that the LGB and the BB are perfectly the same and are indistinguishable. That means we can use one rather than the other.

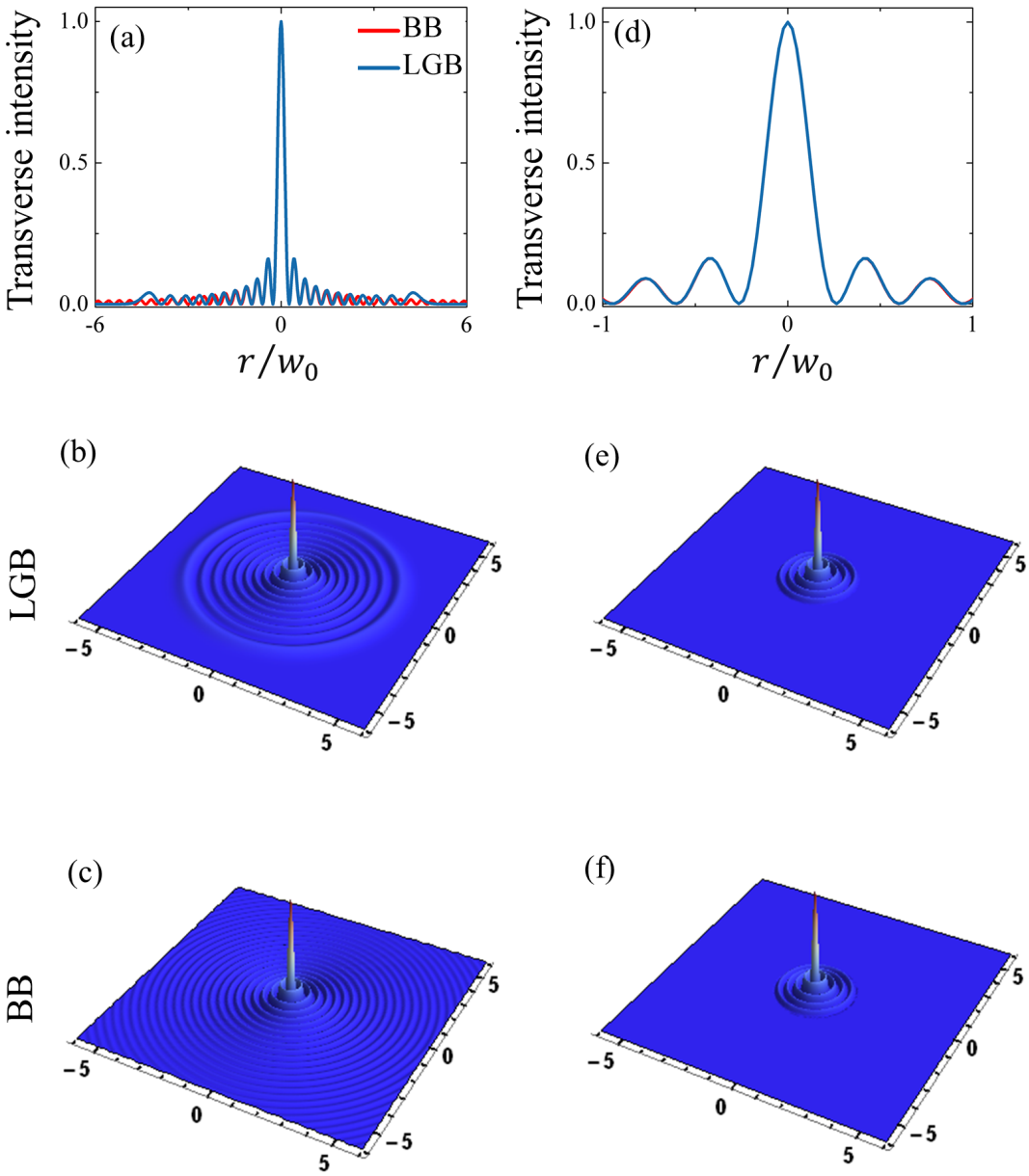

Figure 3.1: The transverse cross sections and the intensity profiles of the LGB_n and its equivalent BB (top), for a beam order $p = 10$, showing the truncated versions (bottom).

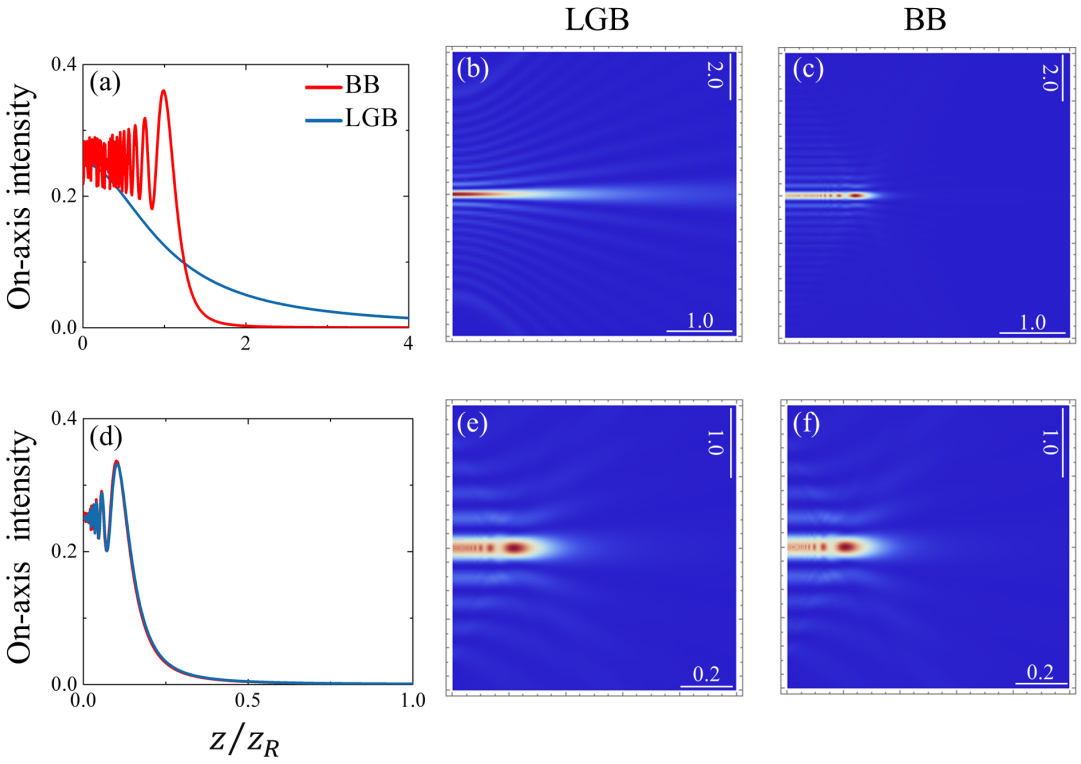

Figure 3.2: The on-axis intensty (first column) and the propagation in the $\xi - z$ (second and third column) of the LGB_p and its equivalent BB (top), for a beam order $p = 10$, showing the truncated versions (bottom).

The electric fields, that will be used next, of the LGB_p and its equivalent the BB at the initial plane $z = 0$, can be written as follows

$$u_{LGB_p}(r, z = 0) = L_p\left(2\frac{r^2}{w_0^2}\right)\exp\left(-\frac{r^2}{w_0^2}\right), \tag{3.2}$$

$$u_{BB}(r, z = 0) = J_0\left(2\sqrt{2p+1}\frac{r}{w_0}\right). \tag{3.3}$$

In order to investigate the truncation effect on the similarity between the LGB_p and the BB, we present in Figure 3.3 the variation of the similarity degree S as a function of the truncation parameter $\delta = a/w_0$ for different beam orders p. As mentioned in the previous

chapter the similarity between two functions is given by

$$S = \cos(|u_1|, |u_2|) = \frac{(|u_1|, |u_2|)}{||u_1||||u_2||} \tag{3.4}$$

with u_1 and u_2 , for this chapter, denotes the optical fields of the LGB_p and BB (Eq. 3.2 and Eq. 3.3), respectively, for this chapter.

Eq. 3.4 becomes

$$S = \frac{\int_0^a u_{LGB_p}(r, z=0) u^*_{BB}(r, z=0) r dr}{\sqrt{\int_0^a u_{LGB_p}(r, z=0) u^*_{LGB_p}(r, z=0) r dr} \sqrt{\int_0^a u_{BB}(r, z=0) u^*_{BB}(r, z=0) r dr}}, \tag{3.5}$$

$(*)$ denotes the complex conjugate.

For $(0 \leq \delta \leq 2)$, $S = 1$, the two beams overlap perfectly for all beam orders p. In the following sections, based on this result, we will consider the LGB_p and the BB as the same, which will allow us to evaluate the Kirchhoff-Fresnel diffraction integral that have referred to in the previous chapter of the diffracted LGB_p, analytically.

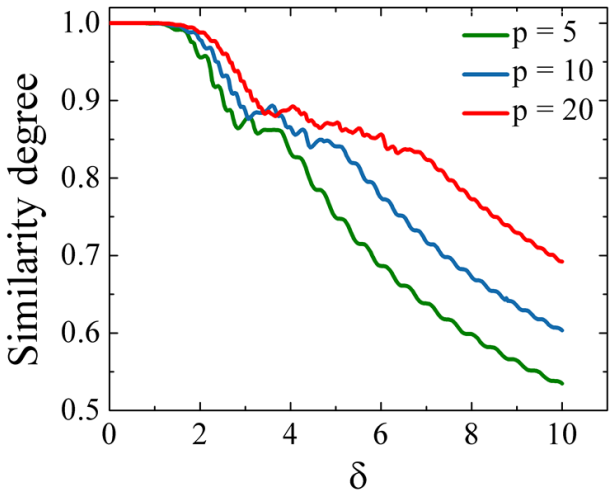

Figure 3.3: The similarity degree between LGB_p and its equivalent BB as a function of the truncation parameter δ, for different beam orders p.

As a last part of the comparison between the LGB_p and the BB, we exhibit in Figure 3.4 the intensity profiles of the LGB_{10} and its equivalent BB, for different cases. Figures 3.4(a-b) show the LGB_{10} and BB for no truncation or obstruction, while Figures. 3.4(c-d) show the LGB_p and BB with truncation ($\delta = 2$,). It can be seen that after truncation the two beams become indistinguishable. Figures 3.4(e-f) show the remaining parts from the truncated beams.

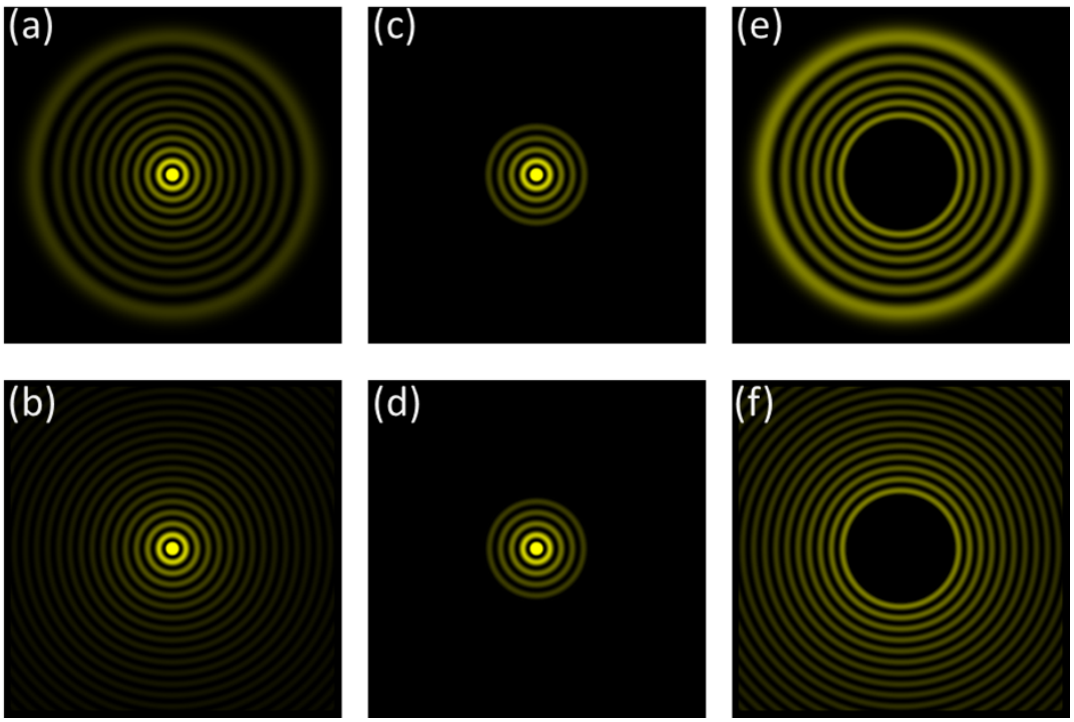

Figure 3.4: The LGB_p versus the BB. (a) and (b), represent respectively the unobstructed LGB_{10} and BB. (c) and (d), represent respectively the truncated LGB_{10} and BB. (e) and (f), represent the remaining outer multi-ring part of the truncated LGB_{10} and BB shown in (c) and (d).

The significant difference between the LGB_p and BB in the outer multi-ring part, motivated us to seek another peer to the LGB_p. Figure 3.5(a) shows the outer multi-ring part of the LGB_{10}, while Figures 3.5(b) shows the new beam we suggest to replace the outer multi-ring part of the LGB_{10}, it is composed of many rings represented by different colors. The details regarding the new beam will be discussed in the next section.

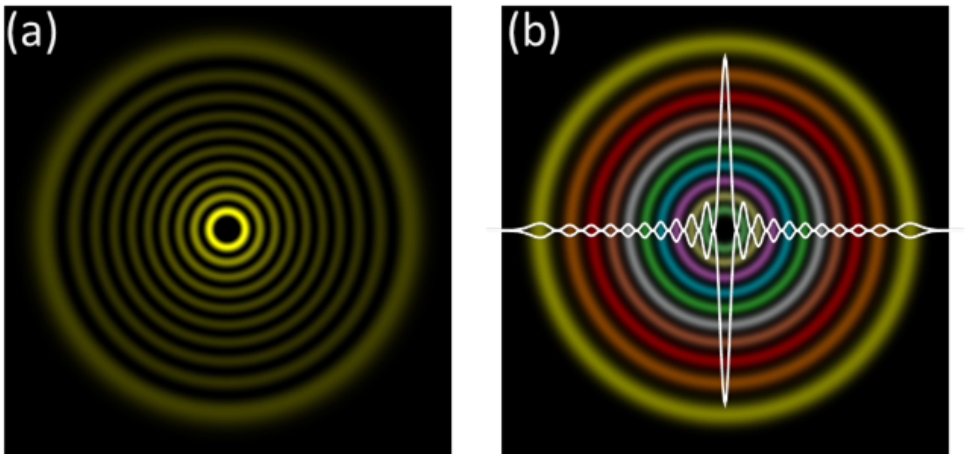

Figure 3.5: The new modeling representation of the outer multi-ring part of the LGB_{10}. (a) The outer multi-ring part of the LGB_{10}, (b) A sum of rings represented by different colors located at the same LGB_{10} rings. The white profiles correspond to the LGB_{10} intensity distribution.

3.3 Analytical description of diffracted LG beam

In this section, we describe the far-field (the focal plane of a lens) of the diffraction of LGBs focusing on the opaque disk case, analytically, where we base on the comparison performed in the previous section.

The Fresnel Khichhoff diffraction integral, mentioned in the previous chapter, of the propagated field at a focal plane of the lens ($z = f$) in cylindrical coordinates system can be written as follows

$$u_{out}(\rho, z) = \frac{i2\pi}{\lambda z} \exp\left(i\frac{2\pi}{\lambda}\left(z + \frac{\rho^2}{2z}\right)\right) \int_0^\infty u_{in}(r, z = 0)\tau(r) J_0\left(\frac{2\pi}{\lambda z}\rho r\right) r dr, \tag{3.6}$$

with $\tau(r)$ is the transmittance function of the obstacle.

It's worth noting that using a lens means making a Fourier transform. The Fourier

transform in the cylindrical coordinates is known as the Hankel transform.

3.3.1 Far-field of the diffracted LGB by small apertures

As we demonstrated above, the LGB is similar to BB only in the truncated version of small obstacles. Thus we consider the BB in place of the LGB in order to obtain the far-field of diffracted LGB by an aperture, which has no analytical expression in contrast to the BB. The analytical expression for the far-field of truncated BB has been demonstrated before by many authors, it is given by [74–76]

$$\begin{aligned}\int_0^a u_{LGB_p}(r, z=0) J_0\left(\frac{2\pi}{\lambda f}\rho r\right) r dr &= \int_0^a u_{BB}(r, z=0) J_0\left(\frac{2\pi}{\lambda f}\rho r\right) r dr \\ &= a^2 \frac{\beta J_1(\beta) J_0(D) - D J_1(D) J_0(\beta)}{\beta^2 - D^2}\end{aligned} \tag{3.7}$$

where r and ρ are the transverse field amplitude coordinates at the input and Fourier planes, respectively. $\beta = 2\sqrt{2p+1} \times a/w$, $D = 2\pi a\rho/\lambda f$. $2a$ is the aperture diameter, λ the wavelength, and f is the focal length of a lens.

The expression in Eq. (3.7) allows as to describe the far-field of diffracted LGB by small apertures analytically ($\delta < 2$).

Figure 3.6 presents the far-field intensity distributions of the diffracted LGB by an aperture having a diameter lying between $\delta = 0.60$ in Fig. 3.6(a), and $\delta = 2.04$ in Figure 3.6(f), where the blue line corresponds to the numerical simulation of LGB and the red line corresponds to the analytical expression of BB. It's visible that the two beams are practically the same for the three first truncation parameters (Figure 3.6(a), (b), and (c)), while for the other three ones (Figure 3.6(d), (d), and (f)), in general, they good overlap.

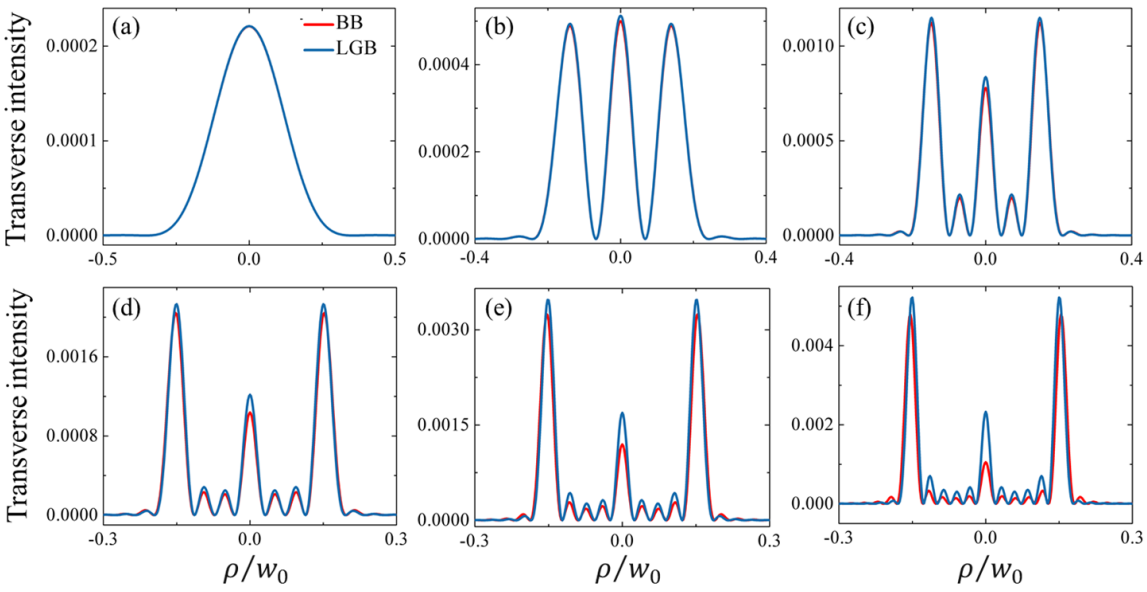

Figure 3.6: The intensity distribution at the focal plane of a lens ($f = 100mm$) of the apertured LGB_{10}, from, on its second intensity's zero in (a) to on its sixth intensity's zero in (i); numerical integration (in red) versus analytical expression (in blue).

3.3.2 Far-field of the diffracted LGB by an opaque disk

In this section, we study the analytical description of the diffracted LGB by an opaque disk through two parts, wherein for small sizes we adopt the BB approximation shown above while for the big ones the remaining part of the beam will be considered as a sum of ring shifted-Gaussian beams.

Considering LGB as BB for small opaque disks

The far-field of the diffracted LGB beam by an opaque can be obtained via the Babinet principle [32] which states that the sum of the diffracted fields by two complementary obstacles is the propagated field without obstacle, as follows

$$\begin{aligned}&\int_a^{\infty} u_{LGB_p}(r, z=0) J_0\left(\frac{2\pi}{\lambda f}\rho r\right) r dr = \\ &\int_0^{\infty} u_{LGB_p}(r, z=f) J_0\left(\frac{2\pi}{\lambda f}\rho r\right) r dr - \int_0^{a} u_{LGB_p}(r, z=f) J_0\left(\frac{2\pi}{\lambda f}\rho r\right) r dr.\end{aligned} \tag{3.8}$$

The Hankel transform of the propagated LGB_p without obstacle (un-diffracted LGB_p) is straightforward, which can be obtained from the table of integrals, it is given by [77]

$$\int_0^\infty u_{LGB_p}(r, z=0) J_0\left(\frac{2\pi}{\lambda f}\rho r\right) r dr = (-1)^p \left(\frac{w_0^2}{2}\right) L_p\left(2\frac{\rho^2}{(\lambda f/\pi w_0)^2}\right) \exp\left(-\frac{\rho^2}{(\lambda f/\pi w_0)^2}\right). \tag{3.9}$$

While the diffracted LGB_p by a small aperture is given above by the Eq. 3.7 using the approximation of LGB_p to BB.

By substituting Eqs. (3.9) and Eqs. (3.7) into Eq. (3.8), the far-field of the diffracted LGB_p by an opaque disk can be written analytically as follows

$$\begin{aligned} u_{LGB_p}(\rho, z=f) \approx & (-1)^p \left(\frac{w_0^2}{2}\right) L_p\left(2\frac{\rho^2}{(\lambda f/\pi w_0)^2}\right) \exp\left(-\frac{\rho^2}{(\lambda f/\pi w_0)^2}\right) \\ & - a^2 \frac{\beta J_1(\beta) J_0(D) - D J_1(D) J_0(\beta)}{\beta^2 - D^2}. \end{aligned} \tag{3.10}$$

In order to validate the obtained analytical expression, some simulations of the Eq. (3.10) are shown in Figure 3.7. As an example, we plot the diffracted LG_{10} by different opaque disks having a diameter lying between $\delta = 0.60$ in Figure 3.7(a), and $\delta = 3.87$ in Figure 3.7(i). It can be seen, from Figure 3.7(a) to Figure 3.7(e)($\delta = 2.04$), that the obtained LGB_{10} far-field intensities using the analytical expression of Eq. (3.10) (in blue) overlap perfectly with that obtained by the first integral of Eq. (3.8) (in red) in the case of small opaque disks ($\delta \leq 2$). These presented simulations are consistent with those demonstrated by the similarity degree shown in Figure 3.3.

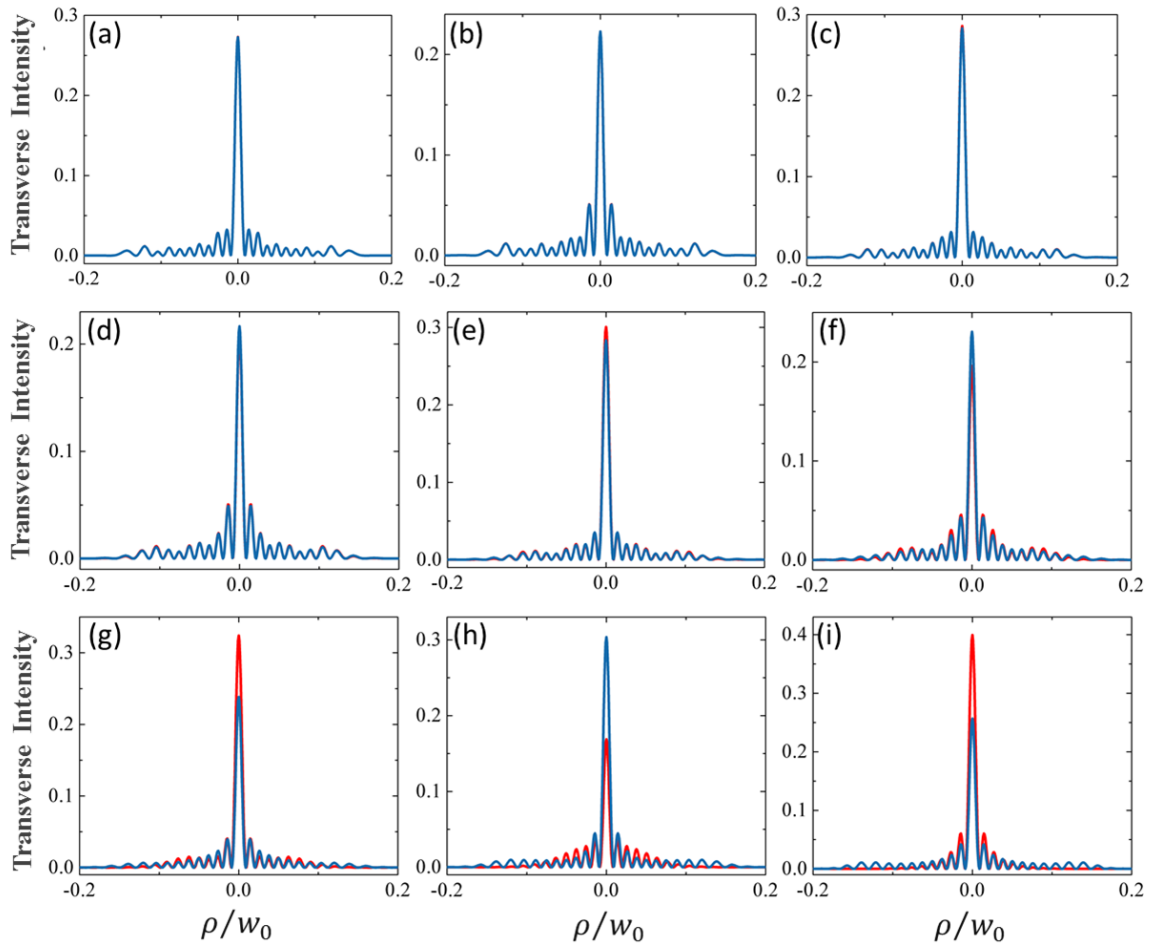

Figure 3.7: The intensity distribution at the focal plane of a lens ($f = 100mm$) of the obstructed LGB_{10}, from, on its second intensity's zero in (a) to on its last intensity's zero in (i); numerical integration (in red) versus analytical expression (in blue).

Considering LGB as BB for big opaque disks

In this section, we investigate the LGB_p that undergoing big opaque disks, where the BB is not a good approximation. The remaining rings after the similar rings to BB could be modeled as a sum of a ring shifted-Gaussian beams expressed by $(-1)^i a_i \exp[-((r - r_{0_i})/w_{0_i})^2]$. Each ring of the un-equivalent LGB_p part to BB corresponds to one ring shifted-Gaussian beam. Here r_{0_i} is the center position of the i ring and w_0 represents the ring width. The $(-1)^i$ term ensures a pi phase shift between two consecutive rings (as in LGB_p), and a_i expresses the pic intensity ratios between the different i rings compared to those of real LGB_p.

To model the remaining rings of the LGB_p by ring shifted-Gaussian beams, we adopt the zeroes positions of the LGB_p intensity (here r_i is the i^{th} zero of the LGB_p intensity calculated numerically using Mathematica). We consider the difference between two consecutive zeroes as the width $w_{0_i} = (r_{i+1} - r_i)/2 = \Delta r_i$ of the ring i, and the quantity $r_{0_i} = (r_{i+1} + r_i)/2$ stays for the half diameter of the i ring. The a_i values of i ring shifted-Gaussian beams could be extracted directly from the peak's intensity ratios of ideal LGB_p. Figure 3.8 presents an illustrative schema for the different parameters of ring shifted-Gaussian beams.

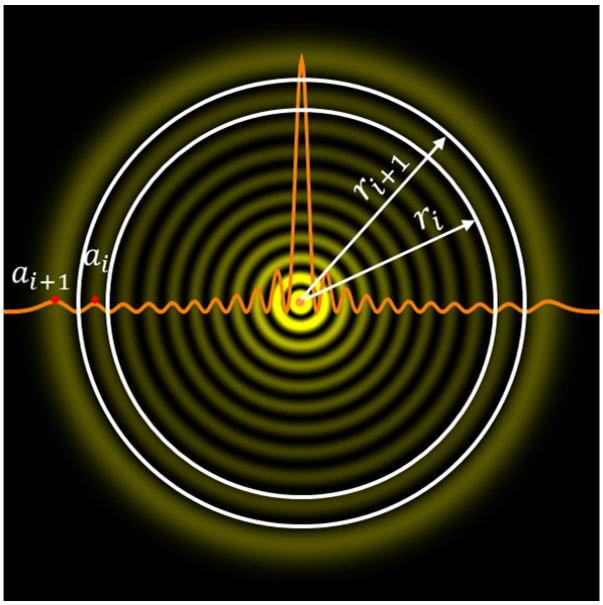

Figure 3.8: Schema illustrating the different parameters of ring shifted-Gaussian beams.

In order to test the validity of our new modeling concerning the sum of ring shifted-Gaussian beams, we simulate in Figure 3.9 the obstructed LGB_{10} by two opaque disks having two different sizes. Figure 3.9 (a) shows the sum of five rings using the model of ring shifted-Gaussian beams, the latter was plotted employing the LGB_{10} profile. Figure 3.9(b) shows simultaneously the intensity profile of the diffracted LGB_{10} by an opaque disk and its equivalent two rings shifted-Gaussian beam, where it's visible that they overlap perfectly. Figure 3.9(c) displays the density plot of two rings modeled using two ring

shifted-Gaussian beams, where it's overlap with the LGB_{10} intensity profile (white plot). Figure 3.9(d) shows the intensity profiles of the obstructed LGB_{10} by an opaque disk and its equivalent two ring shifted-Gaussian beams, evident they are perfectly the same.

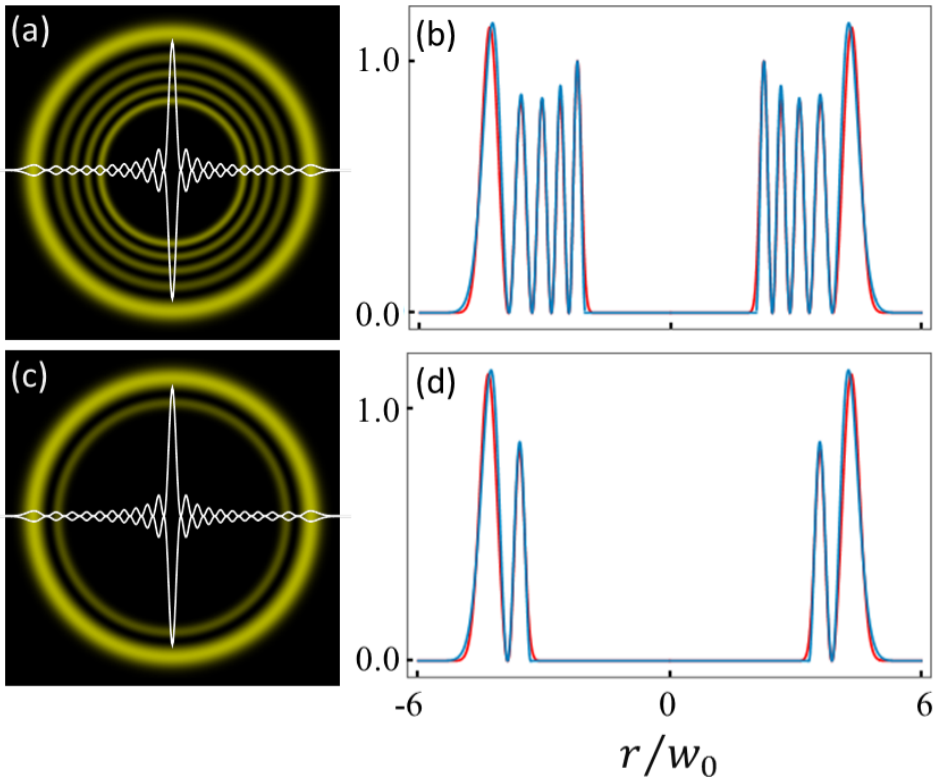

Figure 3.9: Density plots (a,c) and transverse intensities (b,d) of obstructed LGB_p (in blue) modeled as a sum of ring shifted-Gaussian beams (in red). The white curve represents LGB_{10} profile, while the yellow five rings are ring shifted-Gaussian beams located at the same positions as the LGB_{10} rings.

As Figure 3.9 is demonstrated, the obstructed LGB_p by an opaque disk and its equivalent ring shifted-Gaussian beams are almost the same at a given input plane $z = 0$. In Figure 3.10, we plotted the on-axis intensity as a function of the normalized propagation distance for the same beams of Figure 3.9. It seems that the obstructed LGB_{10}, and their equivalent, the ring shifted-Gaussian beams, sustain their overlapping during propagation.

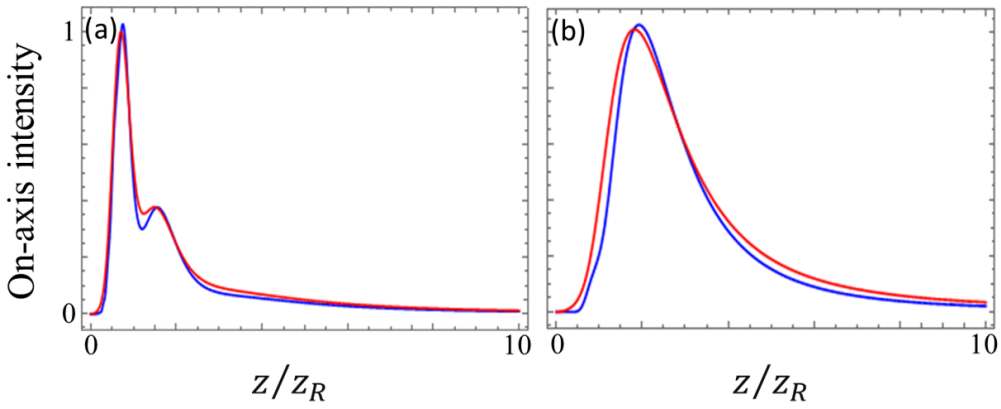

Figure 3.10: The on-axis intensity of the obstructed LGB_{10} as a function of the normalized propagation distance. (a) obstructed LGB_{10} (in blue) with its equivalent five ring shifted-Gaussian beam (in red), (b) the obstructed LGB_{10} with its equivalent two rings shifted-Gaussian beam.

In order to quantitatively validate the suggested model, the ring shifted-Gaussian beams, Figure 3.11 presents a quantitative (Figure 3.11 (a)) and qualitative (Figure 3.11 (b)) comparison between the obstructed LGB_{10} and the corresponding ring shifted-Gaussian beams. In Figure 3.11 (a), whatever the number of the remaining rings, the similarity degree $S \approx 1$, indicates that the two beams are the same. As well, Figure 3.11 (b) shows that they are completely identical. Thus, that confirms that this second approximation can be used for all obstacle sizes greater than the central peak. It is worth noting that there is no constraint related to the beam order, for that reason we have plotted the similarity degree for just one beam order $p = 10$.

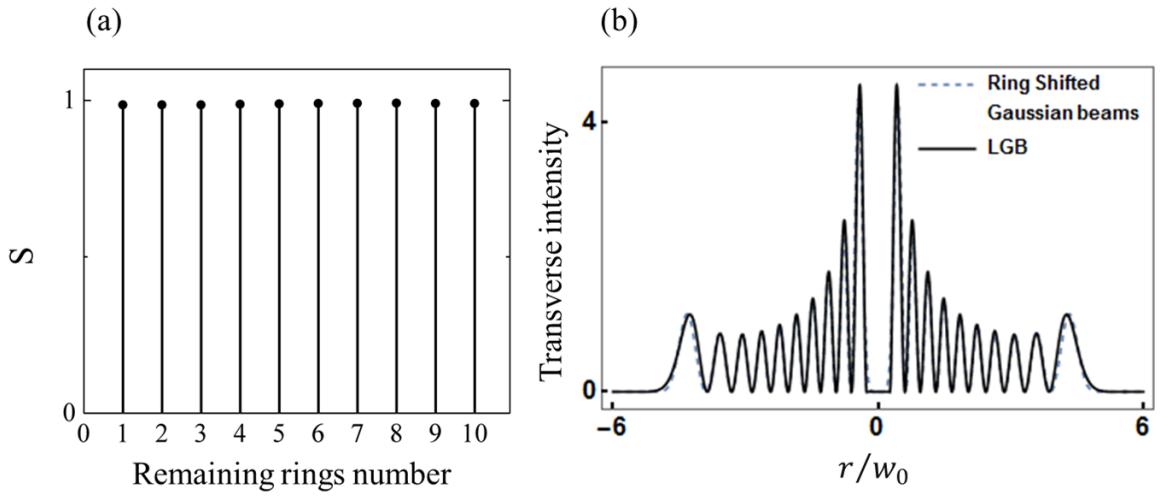

Figure 3.11: (a)The similarity degree between the obstructed LGB_{10} and its equivalent ring shifted-Gaussian beams for a different number of the remaining rings. (b) The transverse cross-sections of the obstructed LGB_{10} on its centrale lobe and the corresponding ring shifted-Gaussian beams.

The far-field or rather the Hankel transform of the diffracted LGB_p by an opaque disk using the ring shifted-Gaussian beams approximation is given by

$$\int_a^{\infty} u_{LGB_p}(r, z=0) J_0\left(\frac{2\pi}{\lambda f}\rho r\right) r dr \approx \int_0^{\infty} \sum_i^p (-1)^i a_i \exp\left[-\left(\frac{r-r_{0_i}}{\Delta r_i}\right)^2\right] J_0\left(\frac{2\pi}{\lambda f}\rho r\right) r dr. \tag{3.11}$$

In order to evaluate the integral of Eq. (3.11), we use the properties of the Delta Dirac function and the convolution operator [55], so, it can be written as follows

$$\int_a^{\infty} u_{LGB_p}(r, z=0) J_0\left(\frac{2\pi}{\lambda f} r\rho\right) \rho d\rho \approx \sum_i^p FT(-1)^i a_i \left[\exp\left[-\left(\frac{r}{\Delta r_i}\right)^2\right] * \delta(r-r_{0_i})\right]. \tag{3.12}$$

The sum of Eq. (3.12) is calculated as follows

$$FT\left[\exp\left[-\left(\frac{r}{\Delta r_i}\right)^2\right] * \delta(r-r_{0_i})\right] = FT\left[\exp\left[-\left(\frac{r}{\Delta r_i}\right)^2\right]\right] FT\left[\delta(r-r_{0_i})\right]. \quad (3.13)$$

Using Hankel transform, of the Gaussian and the shifted Delta Dirac functions, Eq. (3.13) becomes

$$FT\left[\exp\left[-\left(\frac{r}{\Delta r_i}\right)^2\right]\right] FT\left[\delta(r-r_{0_i})\right] = \frac{1}{\lambda f} r_{0_i} \Delta r_i J_0[k_r \rho] \exp\left[-\left(\frac{\rho}{w_{0_f}}\right)^2\right], \quad (3.14)$$

where $k_r = 2\pi r_{0_i}/\lambda f$ and $w_{0f} = \lambda f/\pi \Delta r_i$.

The far-field of the diffracted LGB_p by an opaque disk, using the ring shifted-Gaussian beams approximation, can be written analytically as follows

$$\int_a^\infty u_{LGB_p}(r, z=0) J_0\left(\frac{2\pi}{\lambda f} r\rho\right) r dr \approx \sum_i^p (-1)^i a_i \frac{1}{\lambda f} r_{0_i} \Delta r_i J_0[k_r \rho] \exp\left[-\left(\frac{\rho}{w_{0_f}}\right)^2\right]. \quad (3.15)$$

To investigate the far-field intensity of the diffracted LGB_p by an opaque disk, we use the ring shifted-Gaussian beams plotted with their equivalent LGB_{10} in Figure 3.12. The intensity distributions of the input diffracted LGB_{10} by an opaque disk are presented on the left column and their corresponding far-field intensities on the right column. It can be seen that for bigger obstructions, where few LGB_p rings remain, the ring shifted-Gaussian beams and their equivalent obstructed LGB_p are almost the same. The slight difference that appears in Figs. 3.12(h) and (j) results from the cumulative error of the contribution of many rings.

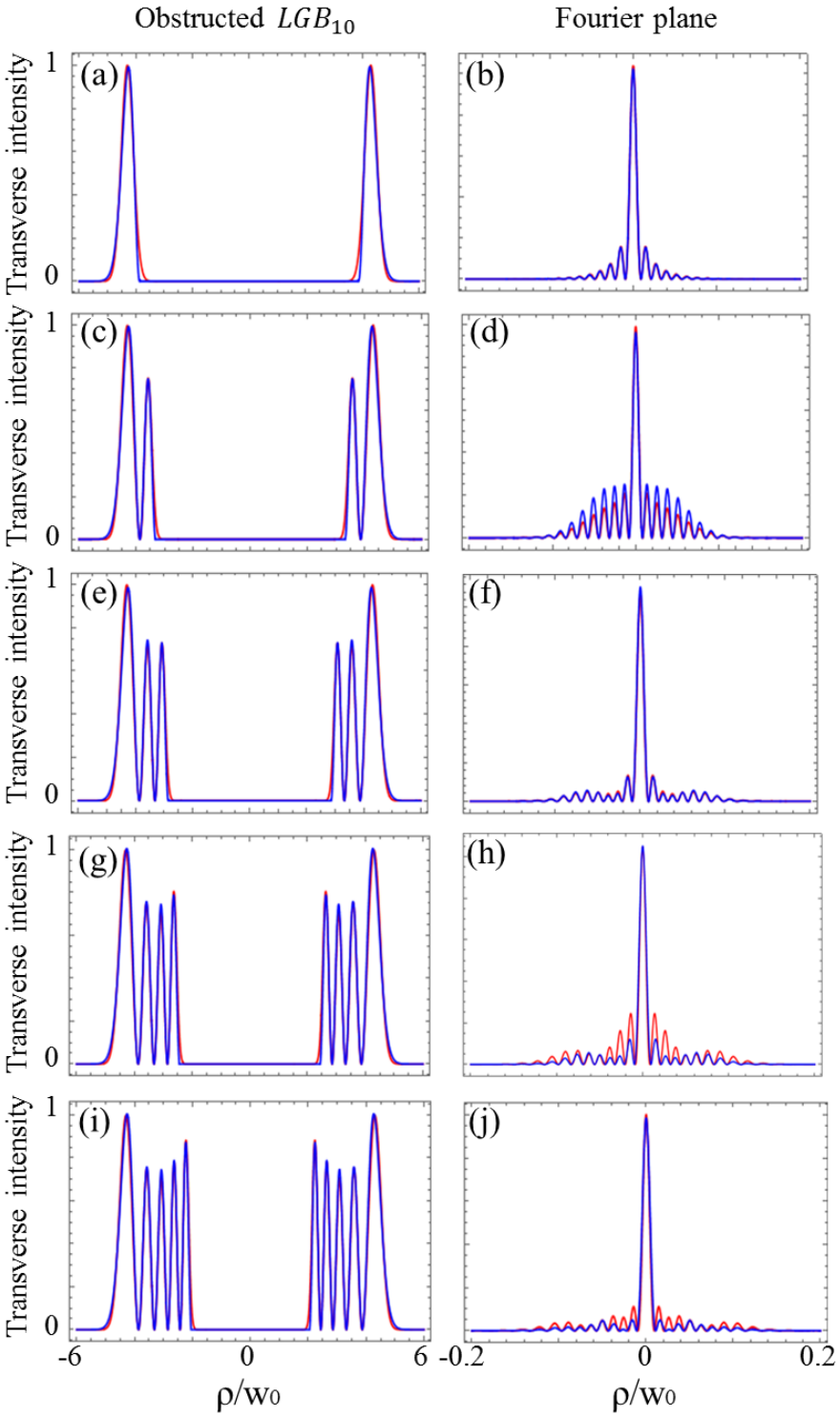

Figure 3.12: The intensity distributions of the obstructed LGB_{10} (blue line) and the shifted-ring Gaussian beams (red line), at the input plane on the left and the Fourier plane on the right.

3.4 conclusion

In this chapter, we have provided mathematical modelings of the diffracted LGB by an aperture and opaque disks of defined sizes; at the far-field. We have demonstrated based on an asymptotic formula that the LGB is identical to BB only in the inner part, where they have similar truncated behavior. Therefore, we have suggested a new similar beam structure for the outer rings of the LGB (the remaining rings that are not similar to BB) that we have called ring shifted-Gaussian beams. These two approximations of LGB led to split its modeling study into two parts; BB for small sizes and ring shifted-Gaussian beams for big sizes. The obtained analytical modelings are in good agreement with the numerical simulations.

Chapter 4

Spatial and propagation properties of the Cosine-Gauss beams

The present chapter contains extracts from a publication by *Bencheikh, Chabou, et al* [78].

4.1 Introduction

Diffraction of light was first reported by Leonardo da Vinci (1452–1519) [79]. Grimaldi observed systematically the diffraction of light about 1660 and coined the word "diffraction" [80, 81]. So, the first steps to its understanding were only made in the 17^{th} (Huygens, Hook, Newton) and 18^{th} centuries (Fresnel, Young) [32, 82–86]. Then, Stratton first derived expressions for invariant beams [87]. In 1987 Durnin [37, 88] was the first to point out that one could obtain a set of solutions for the free-space scalar wave equation that was diffraction free (propagation invariant), called Bessel beam.

So the Bessel beam which has cylindrical symmetry was the first non-diffracting beam introduced. Since then, many other geometries [89–91], including arbitrarily shaped non-diffracting fields [92], have been exploited. Later, one-dimensional and two-dimensional Cosine beams were introduced as a nondiffracting beam in Cartesian coordinates. The

Cosine beams nondiffracting nature was demonstrated for the first time in 1994 [93, 94]. These beams, as Bessel beams, are of infinite transverse extent and energy and thus can not be generated experimentally. For that reason, in 1997, Jiang proposed the truncated-Cosine beams and an apodized version of CB (the super-Gaussian-Cosine beams) [95], in order to overcome the infinite energy problem. Later in 2005, Gutierrez et al demonstrated theoretically that Cosine-Gauss (CG) beams belong to a more general wave family, which is the nondiffracting Helmholtz-Gauss waves [9]. Due to their nondiffracting and self-healing natures, Cosine beams have attracted a large community of researchers, where they have been used in light sheet microscopy [96–99], optical wireless communication [100–102], Plasmonics [103], and even in hydrodynamics for studying water waves [104].

In this chapter, we discuss theoretically, providing analytical expressions, the spatial and propagation properties of the Cosine-Gauss beams of fundamental and higher-order.

4.2 Theory of Cosine beam

The ideal Cosine beam, which is an exact solution to the Helmholtz equation in cartesian coordinates, is a standing wave that could be obtained from the superposition of two oppositely oblique plane waves. Its complex amplitude can be expressed as follows

$$u(y,z) = \cos\left(k_y y\right) \exp\left(-ik_z z\right), \tag{4.1}$$

where k_z and k_y are, respectively, the longitudinal and the transverse wave vectors, they are related by $\sqrt{k_y^2 + k_z^2} = k = 2\pi/\lambda$, and λ is the wavelength.

The intensity distribution of the CB is proportional to $|u(y,z)|^2$ and is independent of the propagation distance z; therefor, the CB is a nondiffracting beam. However, as in the case of the Bessel beam, the total energy and the extent at any transverse plane

is infinite, and thus the ideal CB beam can not be physically realized. The physically practical approximation of this beam is generated using apodization functions. In the present section, we discuss the propagation of the apodized CB by a window function (rectangular) and a gaussian function, which are expressed as follows

$$P_{rect}(y) = rect\left(\frac{y}{a}\right) = \begin{cases} 1 & |y| \leq a \\ 0 & |y| \geq a, \end{cases} \tag{4.2}$$

$$P_{Gauss}(y) = \exp\left(-\frac{y^2}{w_0^2}\right), \tag{4.3}$$

where $2a$ is the window width, and $2w_0$ is the Gaussian function width.

By applying an apodization, the CB becomes of limit energy and extent, it is given by

$$u_{AC}(y, z = 0) = \cos\left(k_y y\right) P(y), \tag{4.4}$$

AC indicate the apodized Cosine beam.

The most simple and effective way of the fundamental Cosine beam generation is using an illuminated Fresnel biprism by a Gaussian beam. An alternative method for the CB generation is the use of diffractive optical elements (DOE). Figure 4.1 shows a schematic of the CB generation. The finite distance, z_{max}, after the axicon, in which a Cosine beam is found, is determined from the wave vectors of the CB. This maximum distance (non-diffracting range of the beam) can be estimated geometrically to be

$$z_{max} = a\frac{k}{k_y}, \tag{4.5}$$

where $2a$ is the apodized Cosine beam width.

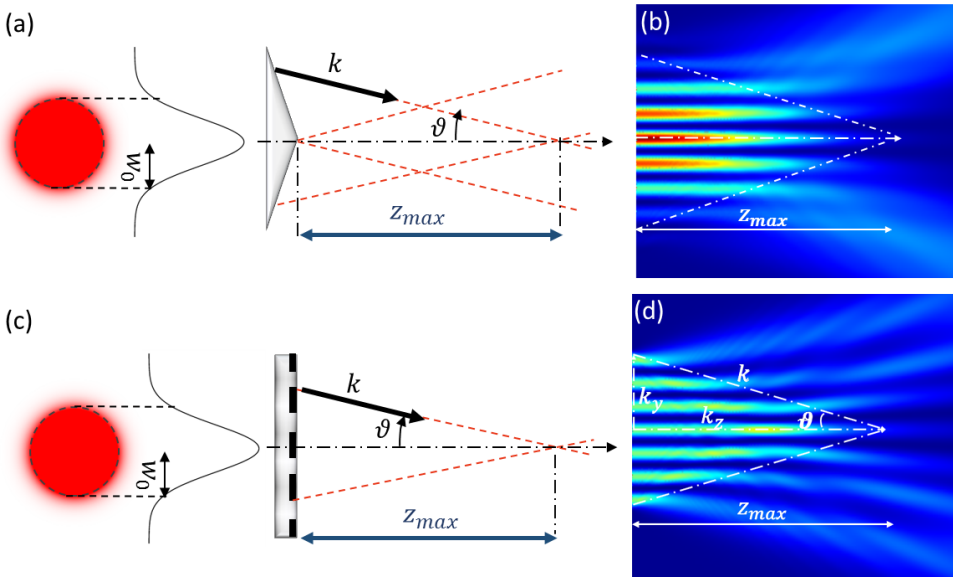

Figure 4.1: Cosine beams Generation using (a) an axicon [1] and (b) a diffractive optical element (DOE) or a Spatial light modulator (SLM). (b) and (d) Numerical simulations. $\sin(\vartheta) = k_y/k$ and $\tan(\vartheta) = a/z_{max}$

It is worth recalling that the schematic shown in Figure 4.1 is the same as that used in reference [105], where it seems that for the DOE (SLM) the nondiffracting range is greater than that of the axicon. In reality they are the same and the nondiffracting range given by Eq. (4.5) depends only on the initial spatial extent and the beam wavelength.

The numerical simulations in this chapter are based on Gaussian beam waist of $w_0 = 1mm$ and a wavelength of $\lambda = 1.064\mu m$.

4.3 Diffraction-free nature of Cosine-Gauss beams

Most laser beams tend to spread due to diffraction as they propagate, causing the beam radius to increase. One of the things that make the non-diffracting beams of great interest is that it is to a large extent resistant to this diffractive spreading, where they keep its initial size and shape. For pseudo-nondiffracting beams, it retains these only up to some maximum distance z_{max}, illustrated in Figure 2.4 of the second chapter, at which point

the beam begins to deteriorate. Up until the vicinity of z_{max} is reached, the field is approximately transverse-invariant along the z-axis. This means that any transverse plane should look like any other transverse plane.This transverse-invariant is another way of saying that the beam is diffraction-free; the beam does not spread or become distorted in the transverse direction. In this section, we investigate this property for the fundamental and higher-order Cosine-Gauss beams by examining the z_{max} region, referred to in the previous section, analytically.

4.3.1 Propagation characteristics of apodized-Cosine beam

In this section, we investigate the spatial properties of apodized Cosine beam by focusing on that apodized by a Gaussian function, where we define analytically the range where the Cosine-Gauss beam being non-diffracting starting from its spatial extent (beam width).

The propagated field of the apodized Cosine beam can be described using the Kirchhoff-Fresnel diffraction integral, referred in the second chapter, given by

$$u_{out}(\eta, z) = \sqrt{\frac{1}{i\lambda z}} \int_{-\infty}^{+\infty} u_{AC}(y, z = 0) \exp\left(\frac{i\pi}{\lambda z}(\eta - y)^2\right) dy, \tag{4.6}$$

Figure 4.2 displays the propagation of apodized Cosine beam showing its characteristics. Figure 4.2 (a) shows the Cosine beam apodized by a rectangular window, where it can be seen that the sharp truncation of the window causes some ripples manifested at the vicinity of the window edges, as well as during propagation. While Figure 4.2(b) shows the Cosine beam apodized by a Gaussian function (Cosine-Gauss beam), in which the smooth apodization ensures a smooth beam profile during propagation (no ripples). The same spatial extent ($a = w_0$) for two apodized beams gives the same z_{max} distance.

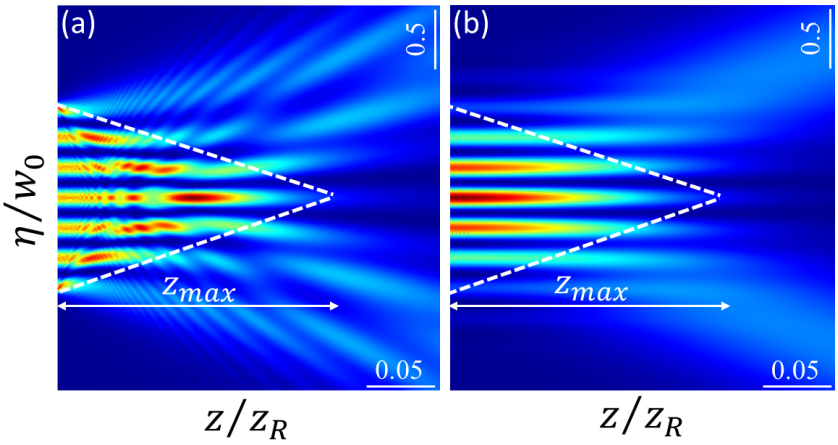

Figure 4.2: Propagation characteristics of apodized Cosine beam. (a) Windowed-Cosine beam. (b) Cosine-Gauss beam. (Both beams have the same width $w_0 = 1mm$).

In the following, we will adopt the Gaussian apodization function that yields from the Gaussian spatial extent of laser beams, it is more practical. So, let's start examining the non-diffracting range z_{max} of the Cosine-Gauss beam, to do that we need first to calculate the beamwidth using the second-order moment, which is useful to mathematically define the radius of an arbitrary laser beam profile. In the second-order moment, the beamwidth is defined by

$$W_{CG} = 2\sqrt{\frac{\int_{-\infty}^{+\infty} y^2 I(y,z)dy}{\int_{-\infty}^{+\infty} I(y,z)dy}}, \tag{4.7}$$

where $I(y,z) = u_{AC}(y,z=0)u^*_{AC}(y,z=0)$ is the intensity distribution of CG beam in our case, and the asterisk being for the complex conjugate.

Substituting the intensity expression of CG beam in Eq. (4.7), with
$\cos(x) = (\exp(ix) + \exp(-ix))/2$ [64]

$$W_{CG} = 2\sqrt{\frac{\int_{-\infty}^{+\infty} y^2 \left(\exp\left(ik_y y - y^2/w_0^2\right) + \exp\left(-ik_y y - y^2/w_0^2\right)\right)^2 dy}{\int_{-\infty}^{+\infty} \left(\exp\left(ik_y y - y^2/w_0^2\right) + \exp\left(-ik_y y - y^2/w_0^2\right)\right)^2 dy}}, \tag{4.8}$$

After simplification Eq. (4.8) becomes:

$$W_{CG} = 2\sqrt{\frac{\int_{-\infty}^{+\infty} y^2 \left(\exp\left(2ik_y y - 2y^2/w_0^2\right) + \exp\left(-2ik_y y - 2y^2/w_0^2\right) + 2\exp\left(-2y^2/w_0^2\right)\right) dy}{\int_{-\infty}^{+\infty} \left(\exp\left(2ik_y y - 2y^2/w_0^2\right) + \exp\left(-2ik_y y - 2y^2/w_0^2\right) + 2\exp\left(-2y^2/w_0^2\right)\right) dy}}, \tag{4.9}$$

By using the following integrals formulas [64] for the numerator of Eq. (4.9)

$$\int_{-\infty}^{+\infty} x^{\nu} \exp(-px^2 + 2qx) dx = \frac{1}{2^{\nu-1}p}\sqrt{\frac{\pi}{p}}\frac{d^{\nu-1}}{dq^{\nu-1}}\left[\mathrm{q}\,\exp(q^2/p)\right]. \tag{4.10}$$

and

$$\int_{-\infty}^{+\infty} x^{2\nu} \exp(-qx^{2h}) dx = \frac{\Gamma(\nu)}{hq^{\nu}}. \tag{4.11}$$

and the following one for the denominator [64]

$$\int_{-\infty}^{+\infty} \exp(-p^2x^2 + qx) dx = \frac{\sqrt{\pi}}{p}\exp(q^2/4p^2), \tag{4.12}$$

The CG beam width W_{CG}, of a transverse wave number k_y and a Gaussian beam width w_0, can be expressed as follows

$$W_{CG}(k_y, w_0) = w_0\sqrt{\frac{1 - k_y^2 w_0^2 + \exp(k_y^2 w_0^2/2)}{1 + \exp(k_y^2 w_0^2/2)}}. \tag{4.13}$$

In order to simplify Eq. (4.13), we use the dimensionless parameter $\alpha = k_y w_0$ and we normalize the CG beam width to the Gaussian beam width $W(\alpha) = W_{CG}/w_0$. Eq. (4.13)

becomes

$$W(\alpha) = \sqrt{1 - \frac{\alpha^2}{1 + \exp(\alpha^2/2)}}. \tag{4.14}$$

Eq. (4.14) show that the normalized beamwidth of the CG beam is always less than one. It seems that the Gaussian envelope modulation with another higher frequency varying function reduces the width (based on the second-order intensity moment) of the resulting modulated function. Its value depends only on the CG beam parameter $\alpha = k_y w_0$.
Since the range of nondiffracting Cosine-Gauss beam depends on the beam width, we substitute Eq. (4.14) into Eq. (4.5) and divided by the Rayleigh range z_R, the final expression of normalized z_{max} is given by

$$\frac{z_{max}}{z_R} = \frac{2}{\alpha}\sqrt{1 - \frac{\alpha^2}{1 + \exp(\alpha^2/2)}}. \tag{4.15}$$

Figure 4.3 displays the normalized CG beam width variation $W(\alpha)$ and the normalized distance z_{max}/z_R, as a function of the parameter α. Figure 4.3(a) indicates that the normalized beam width $W(\alpha)$ shows an interesting behavior. In which one can distinguish two stages, at first where $0 \leq \alpha \leq 4$ the $W(\alpha)$ decreases with increasing of the parameter α until it reaches a critical value equal to 1.6. This value is calculated from the derivative of $W(\alpha)$. Then, $W(\alpha)$ increases to reach a saturated value, at $\alpha \geq 4$, equals 1.
In Figure 4.3(b) the normalized nondiffracting range z_{max}/z_R is always decreasing when α parameter is increasing.

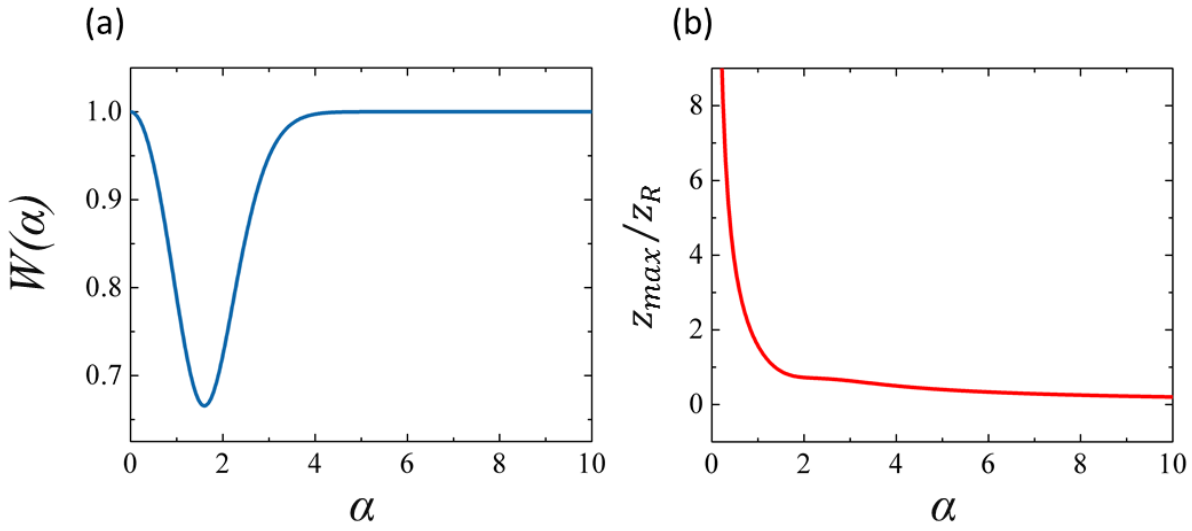

Figure 4.3: (a) The normalized CB width and (b) the normalized nondiffracting distance, as a function of CG parameter α.

As it is shown above, from the $W(\alpha)$ curve, it is possible to reduce the Gaussian beam width by modulating it using oscillating functions. For our case, a Gaussian beam having a width w_0 could be reduced to $0.67w_0$ using a cosine modulating function.

To illustrate the effect of k_y on the spatial extent of CG beam, we plot in Figure 4.4 the CG beam intensity profiles for different values of k_y. As shown in Figure 4.3, the Gaussian beam (obtained for $k_y = 0$) has the largest normalized beam width equals 1. However, at the critical value $\alpha = 1.6$, the CG beam resulting from two superposed oblique Gaussian beams shows the smallest spatial extent, and the beam width $W(\alpha) = 0.67$. The spatial extents for all k_y values are lying between these two critical values (0.67 and 1).

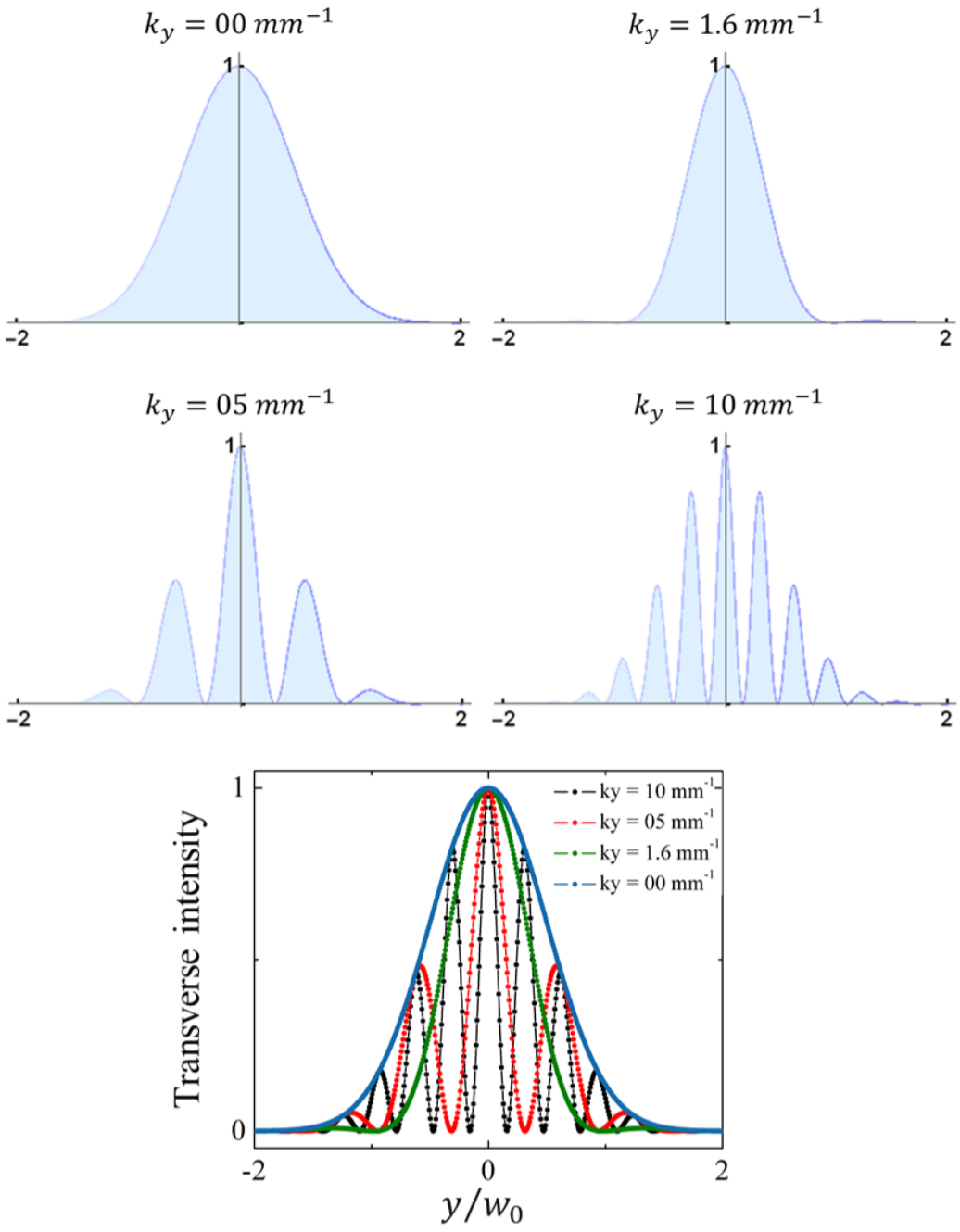

Figure 4.4: CG beam intensity profile showing the effect of k_y on its spatial extent (width).

In order to investigate the α parameter effect on the CG beam propagation, we suggest some density plots showing the CG beam behavior. Figure 4.5 depicts the propagation of CG beam in $(\eta - z)$ plane for α different values, their choice was based on the curves of the Figure 4.4. From Figure 4.5(a), for $\alpha = 0$, the CG beam reduces to a Gaussian beam

and propagates without spreading throughout one Rayleigh range z_R. In Figure 4.5(b), the CG beam, for the critical value $\alpha = 1.6$, gives the tightest CG beam width according to Figure 4.4. The value of this latter is smaller than that of the standard Gaussian beam given by w_0. In Figures. 4.5(c,d), the propagation of CG beam is shown for $\alpha = 5$ and $\alpha = 10$ respectively. It can be seen that the more α increases, more the nondiffracting range of the CG beam decreases, as predicted in Figure 4.3(b). All results concerning the beam range presented in Figure 4.4 and Figure 4.5 are in good agreement.

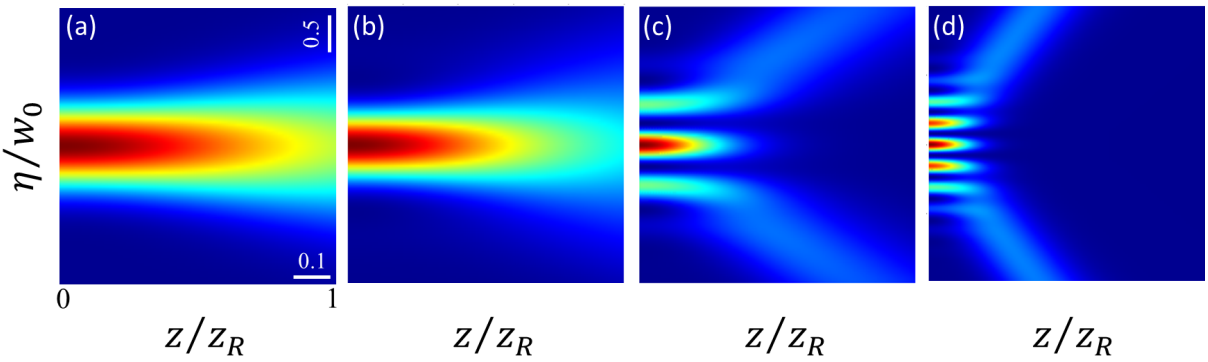

Figure 4.5: CG beam propagation in $(\eta - z)$ plane for different values of α; (a) $\alpha = 0$, (b) $\alpha = 1.6$, (c) $\alpha = 5$, and (d) $\alpha = 10$.

4.3.2 Propagation characteristics of higher-order Cosine-Gauss beam

In this section, we present an efficient but straightforward method for generating higher-order Cosine-Gauss beams from the interference of two oppositely oblique higher-order Hermite-Gauss beams of order n (HG_n) using a prism. The resulting interference pattern gives rise to a standing wave. The latter is nondiffracting in a range defined by the beam width and the angle between the two interfering beams. Moreover, we extend the performed analysis in the previous section to these higher-order beams.

To simulate physically the superposition of HG_n beams and the birth of the standing

wave, we use a prism of apex angle Θ. The schematic layout is presented in Figure 4.6.

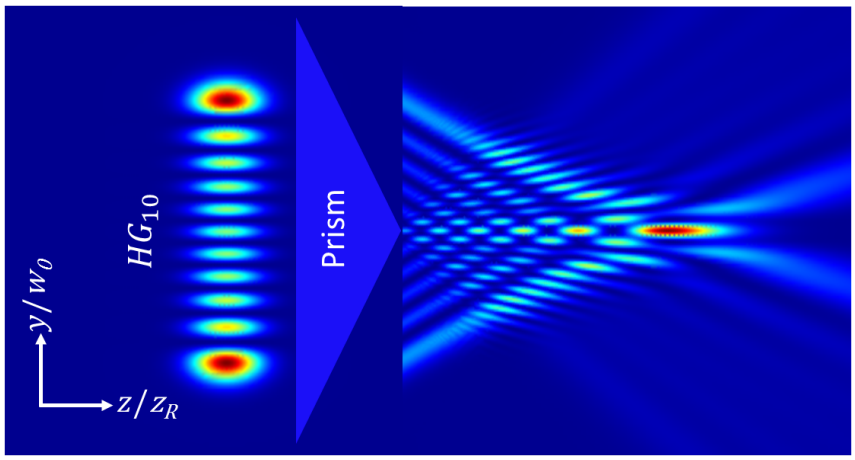

Figure 4.6: Generation of higher order Cosine-Gauss HCG_n beam with $n = 10$ using a prism.

To mathematically describe the propagation of the Hermite-Cosine-Gauss beams of order n (HCG_n) created by a prism, we use the Fresnel Kirchhoff diffraction integral. Thus, the propagated electric field is given as follows

$$\begin{aligned} u_{HCG_n}(\eta, z) = &\int_{-\infty}^{0} u_{HG_n}(y) \exp(-ik_\eta y) \exp\left(-\frac{ik}{2z}(y^2 - 2y\eta)\right) dy \\ &+ \int_{0}^{+\infty} u_{HG_n}(y) \exp(+ik_\eta y) \exp\left(-\frac{ik}{2z}(y^2 - 2y\eta)\right) dy, \end{aligned} \tag{4.16}$$

with $u_{HG_n}(y) = H_n(\sqrt{2}y/w_0)\exp(-y^2/w_0^2)$, H_n is the Hermite polynomial of order n, and w_0 stays for the Gaussian beam width.

The amplitude of the output electric field could be approximated by a Hermite-Cosine-Gauss beam, inferring from a previous work that demonstrated the Gaussian beam conversion into cosine beam using axicon [95], as follows

$$u_{HCG_n}(\eta, z = 0) = H_n\left(\sqrt{2}\frac{\eta}{w_0}\right)\cos(k_\eta \eta)\exp\left(-\frac{\eta^2}{w_0^2}\right). \tag{4.17}$$

Figure 4.7 illustrates a simulation for HCG_{10} beam propagation in $(\eta - z)$ plane using; (a) the numerical calculation of Eq. (4.16) and (b) the expression of Eq. (4.17). The two patterns of Figure 4.7 are the same in the region where the superposition of the two oblique beams occurs. In what follows, we will use the HCG_n beam function given by Eq. (4.17), where it's more practical when implemented on a spatial light modulator (SLM). The latter ensures that HCG_n beam patterns start from $z = 0$, however, in the case of axicon the HGC_n beam occurs only in the region where the two beams are superposed. Therefor, Figure 4.7(b) depicts the case of DOE (diffractive optical element) that simulated usually on SLMs.

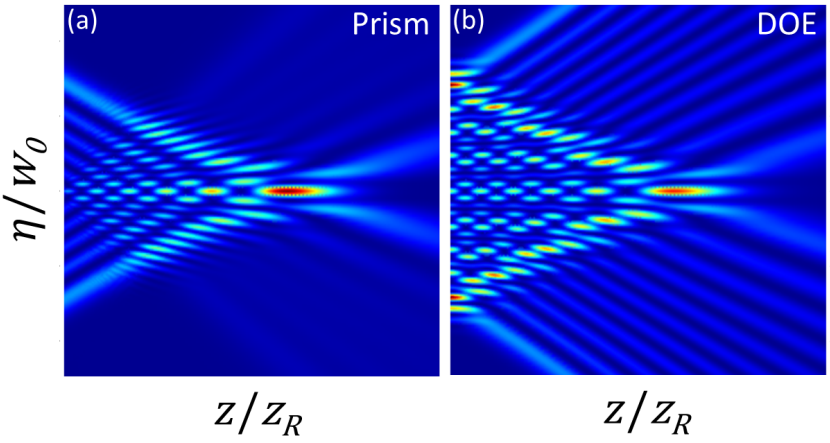

Figure 4.7: Simulations of generated higher order Cosine-Gauss beam using: (a) prism and (b) DOE.

The HCG beam depends on three key parameters; the beam order n, the Gaussian beam width w_0, and the Cosine function parameter k_η. It is a standing wave resulting from the superposition of two traveling oblique waves. Thus, It exhibits a nondiffracting behavior in some regions that depends on the angle between the two skewed beams and on the spatial extent of the HCG_n beam.

As mentioned in the previous section above, the spatial extent or rather the beam width

is calculated using the second-order intensity moments. So, we substitute Eq. (4.17) in Eq. (4.7)

$$W_{HCG_n} = 2\sqrt{\frac{\int_{-\infty}^{+\infty} \eta^2 \left(H_n\left(\sqrt{2}\eta/w_0\right)\right)^2 \left(\exp\left(ik_\eta\eta - \eta^2/w_0^2\right) + \exp\left(-ik_\eta\eta - \eta^2/w_0^2\right)\right)^2 d\eta}{\int_{-\infty}^{+\infty} \left(H_n\left(\sqrt{2}\eta/w_0\right)\right)^2 \left(\exp\left(ik_\eta\eta - \eta^2/w_0^2\right) + \exp\left(-ik_\eta\eta - \eta^2/w_0^2\right)\right)^2 d\eta}}, \tag{4.18}$$

The nominator of Eq. 4.18 becomes

$$\underbrace{\int_{-\infty}^{+\infty} \eta^2 H_n^2\left(\sqrt{2}\eta/w_0\right) \exp\left(2ik_\eta\eta - 2\eta^2/w_0^2\right) d\eta}_{I_1} + \underbrace{\int_{-\infty}^{+\infty} \eta^2 H_n^2\left(\sqrt{2}\eta/w_0\right) \exp\left(-2ik_\eta\eta - 2\eta^2/w_0^2\right) d\eta}_{I_2}$$
$$+ \underbrace{\int_{-\infty}^{+\infty} 2\eta^2 H_n^2\left(\sqrt{2}\eta/w_0\right) \exp(-2\eta^2/w_0^2) d\eta}_{I_3}, \tag{4.19}$$

Applying a partial integration, for I_1 and I_2, $\int udv = uv - \int vdu$, with

$$u = \eta^2 \longrightarrow du = 2\eta$$
$$dv = H_n^2\left(\sqrt{2}\eta/w_0\right) \exp\left(2ik_\eta\eta - 2\eta^2/w_0^2\right) \longrightarrow v = \int H_n^2\left(\sqrt{2}\eta/w_0\right) \exp\left(2ik_\eta\eta - 2\eta^2/w_0^2\right), \tag{4.20}$$

Then, applying a change of variables

$$\frac{\eta'^2}{w_0^2} = \left(\sqrt{2}\frac{\eta}{w_0} \mp \frac{i\alpha}{\sqrt{2}}\right)^2 \Longrightarrow \frac{\eta'}{w_0} = \sqrt{2}\frac{\eta}{w_0} \mp \frac{i\alpha}{\sqrt{2}} \Longrightarrow \sqrt{2}\frac{\eta}{w_0} = \frac{\eta'}{w_0} \pm \frac{i\alpha}{\sqrt{2}} \tag{4.21}$$

and using the following recursion formulae of Hermite polynomials and Laguerre polynomials [106]

$$H_{n+1}(x) = 2xH_n(x) - 2nH_{n-1}(x), \tag{4.22}$$

$$(p+1)L_{p+1}^{l}(x) = (2p+l+1-x)L_p^l(x) - (p+l)L_{p-1}^{l}(x), \tag{4.23}$$

$$L_p^l(x) = L_p^{l+1}(x) - L_{p-1}^{l-1}(x), \tag{4.24}$$

where L_p^l are Laguerre polynomials of order p and index l.

also, using the following integral formula [107]

$$\int_{-\infty}^{+\infty} exp(-x^2)H_m(x+y)H_n(x+z)dx = 2^n\pi^{1/2}m!z^{n-m}L_m^{n-m}(-2yz), \tag{4.25}$$

while, using the following integral formula, for I_3, [107]

$$\int_{-\infty}^{+\infty} x^2exp(-x^2)H_n(x)H_n(x)dx = 2^n\pi^{1/2}n!(n+1/2), \tag{4.26}$$

On the other hand, the denominator of Eq. 4.18 becomes

$$\underbrace{\int_{-\infty}^{+\infty} H_n^2\left(\sqrt{2}\eta/w_0\right)\exp\left(2ik_\eta\eta - 2\eta^2/w_0^2\right)d\eta}_{I_4} + \underbrace{\int_{-\infty}^{+\infty} H_n^2\left(\sqrt{2}\eta/w_0\right)\exp\left(-2ik_\eta\eta - 2\eta^2/w_0^2\right)d\eta}_{I_5}$$
$$+ \underbrace{\int_{-\infty}^{+\infty} 2H_n^2\left(\sqrt{2}\eta/w_0\right)\exp(-2\eta^2/w_0^2)d\eta}_{I_6}, \tag{4.27}$$

Applying a change of variables of Eq. 4.21 and using the integral formula of Eq. 4.25, for I_4 and I_5.

and using the following integral formula, for I_6, [64]

$$\int_{-\infty}^{+\infty} exp(-x^2)H_n(x)H_n(x)dx = 2^n\pi^{1/2}n!, \tag{4.28}$$

After tedious but straightforward calculations, the analytical expression of the normalized HCG$_n$ beam width ($W_n = W_{HCG_n}/\sqrt{2n+1}w_0$) is obtained, which depends only on the CG parameter ($\alpha = k_\eta w_0$) and the beam order n, it's given by d the beam order n, it's expression is given by

$$W_n(\alpha) = \sqrt{1 - \frac{(\alpha^2 L_n^0(\alpha^2) - 2\alpha^2(L_n^1(\alpha^2) - L_n^2(\alpha^2)))}{(2n+1)(L_n^0(\alpha^2) + \exp(\alpha^2/2))}}. \tag{4.29}$$

In order to study the α parameter effect on the normalized HCG$_n$ beam width, we plot in Figure 4.8 the $W_n(\alpha)$ variation for different beam order n values. Two important levels could be noticed; For the first, there is always a dip or rather a minimal value in the

$W_n(\alpha)$ variation, which depends on the beam order n, then the variation becomes oscillatory around the unity. In the second, the normalized beam reaches a saturated value equal to 1, for also a critical value of α that depends on the beam order n. From Figure 4.8, it can be seen that when α reaches a minimum value depends on the beam order, the HG beam width could be reduced approximately by half due to the interference (yielding a cosine function).That influences significantly the z_{max} range of the non-diffracting beam.

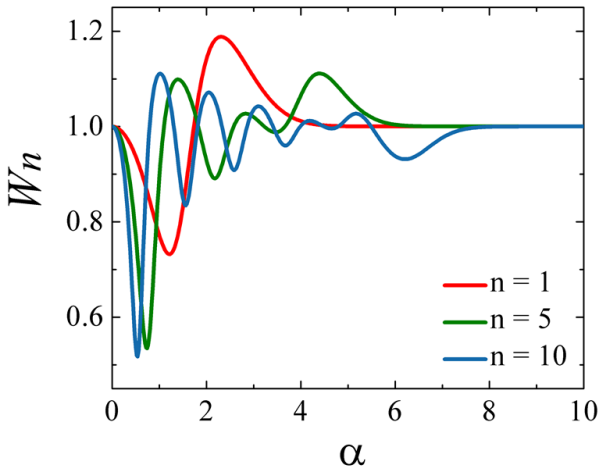

Figure 4.8: The normalized HCG_n beam width as a function of α parameter.

Since the expression of the HCG beam width (the HCG beam spatial extent) is obtained, the z_{max} range could be deduced, substituting Eq. 4.29 into Eq. 4.5, after some algebra as follows

$$\frac{z_{max}}{z_R} = \frac{2}{\alpha}\sqrt{(2n+1) - \frac{\alpha^2 L_n^0(\alpha^2) - 2\alpha^2(L_n^1(\alpha^2) - L_n^2(\alpha^2))}{L_n^0(\alpha^2) + \exp(\alpha^2/2)}}. \tag{4.30}$$

To investigate the nondiffracting range of HCG_n beam, the z_{max}/z_R variation is plotted as a function of CG parameter α for different beam order values ($n = 1$, $n = 5$, and $n = 10$), shown in Figure 4.9 . Then we choose four values of α to present the density plots of HCG_{10} in $(\eta - z)$ plane illustrated in Figure 4.10. The influence of α on the beam range is

evident and it is consistent with the previous results which indicate that the HCG_n beam behavior depends on this value.

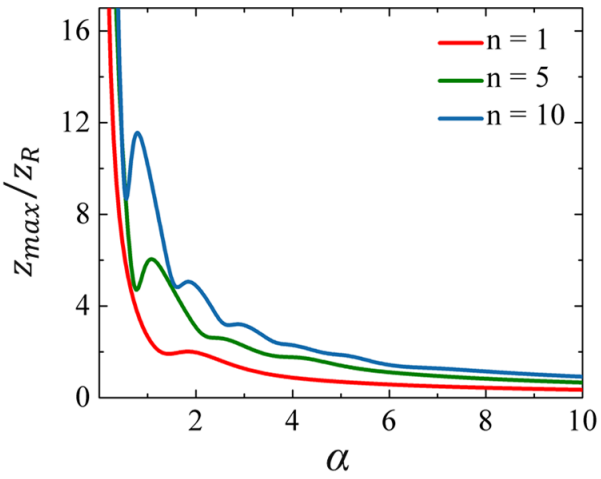

Figure 4.9: The normalized HCG_n beam range as a function of α parameter for different beam order n values.

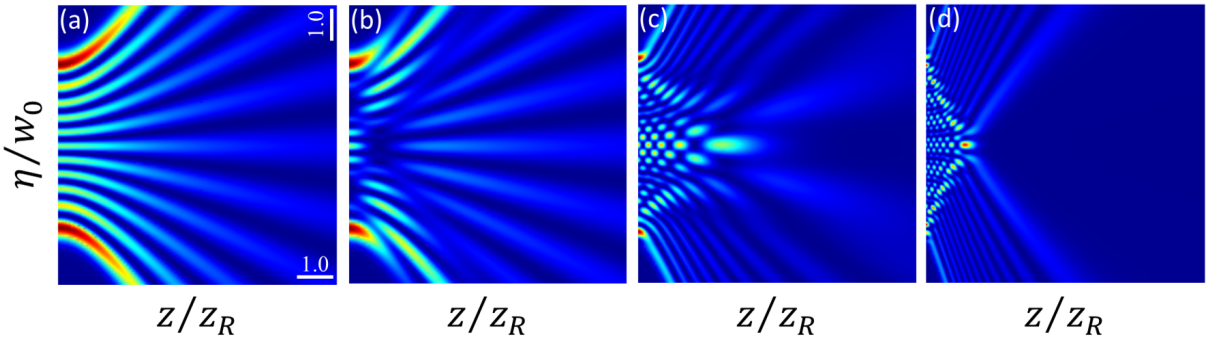

Figure 4.10: HCG beam propagation in $(\eta - z)$ plane for different values of α; (a) $\alpha = 0$, (b) $\alpha = 1$, (c) $\alpha = 5$, and (d) $\alpha = 10$.

4.4 Self-healing property

A peculiar feature of non-diffracting beams is their extreme self-healing properties, discussed in the second chapter, allowing them to reconstruct their original shape, some distance after, even after rather devastating perturbations. This distance is termed the healing distance, it can be determined via simple geometric arguments [35]. To evaluate

the self-healing ability of our studied beams of this chapter, an opaque obstacle is placed at the initial plane, blocking a specific part of the beam, as shown in Figure 4.11. In what follows, we consider the fundamental mode CG beam as a particular case of higher-order HCG beams (HCG_n). Figure 4.11 presents the propagation of obstructed HCG_n, of fundamental order $n = 0$ and of beam order $n = 10$, in the $(\eta - z)$ plane. The influence of the obstruction size, on the beam propagation including the non-diffracting range, is clearly seen from Figure 4.11 (a), (c), and (b), (d).

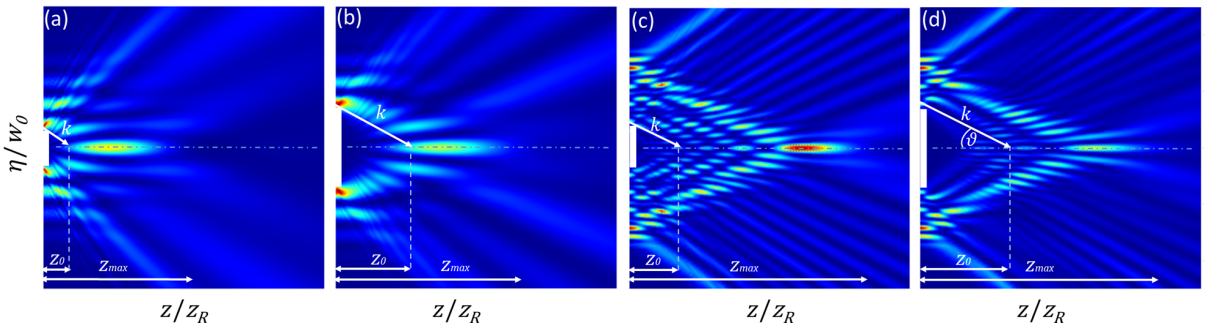

Figure 4.11: Self-healing ability investigation of the HCG_n beams. (a) $n = 0$ with obstruction size 0.25,(b) $n = 0$ with obstruction size 0.5, (c)$n = 10$ with obstruction size 1, and (d)$n = 10$ with obstruction size 2.5.

The minimal distance z_{min} from which the beam begins its profile recovery, depicted in Figure 2.4 of the second chapter, is proportional to the obstruction size, and the first attempt to calculate this distance is purely geometric, as mentioned above. Since we are considering the HCG_n beam as a standing wave resulting from the superposition of two oppositely oblique traveling waves (with angles $+\vartheta$ and $-\vartheta$), we can easily demonstrate an approximation for the distance $z_{min} \leq z_0$ as follows

$$z_0 = 2\delta \frac{z_R}{\alpha}, \tag{4.31}$$

where $\delta = a/w_0$ is the obstacle size.

It is worth noting that the calculation of z_0 expression considers that light propagates in a straight line, ignoring the effect of the light bending due to the diffraction effect. At

least, this is the farthest distance that z_{min} can reach.

To assess the self-healing quality, we use the on-axis intensity for only symmetric HCG_n beams with even order n (because the anti-symmetric HCG_n beams with odd order n posses a null on-axis intensity along propagation axis z). Since all HCG_n beam orders behave in the same manner, the concept is the same. As HCG_n beam exhibits a periodic self-imaging, we suggest using the on-axis intensity. That allows testing the conservation degree of self-imaging periodicity against the different obstacle sizes. In Figure 4.12 we plot the on-axis intensity versus the normalized propagation distance (to z_R), for different obstacle sizes. The conservation of the self-imaging and the periodicity (described here by the intensity maxima) depends strongly on the obstruction size, it can be seen that the more it increases the more intensity pics loses (corresponding to self-imaging planes). In order to make the obstruction size effect on the on-axis intensity more evident, we split the obstruction sizes into two categories. Figure 4.12(a) shows the effect of the small obstruction sizes, while Figure 4.12(b) shows the effect of the big ones. It can be noticed that for small obstruction sizes the on-axis intensity maxima sustain their loci, whereas for big ones, the maxima shifts toward the obstruction plane.

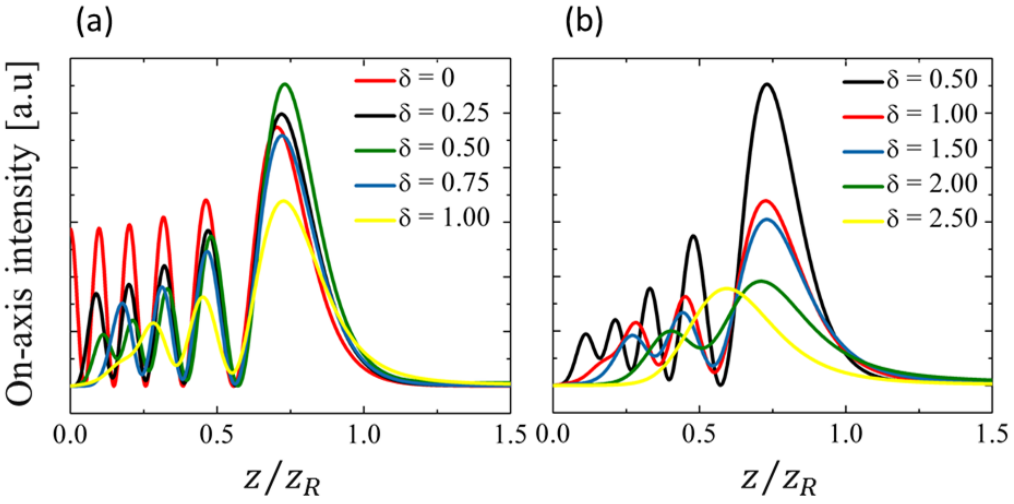

Figure 4.12: Self-healing of obstructed HCG_{10} beam with $\alpha = 10$ undergone different obstacle sizes.

The main interpretation of the Cosine beam family self-healing is based on the superposition of the traveling waves. As long as the two traveling waves are not completely blocked, the interference phenomenon occurs always in some regions, which depends on the size and position of the obstruction.

The HCG_n beam self-healing degree during propagation can be quantitatively described, as a function of obstruction size, using the similarity function, discussed in the second chapter, as follows

$$S(z) = \frac{\int_{-\infty}^{+\infty} u_{HCG_n}^{obs}(\eta, z) u_{HCG_n}^{*}(\eta, z) d\eta}{\sqrt{\int_{-\infty}^{+\infty} \mid u_{HCG_n}^{obs}(\eta, z) \mid^2 d\eta} \sqrt{\int_{-\infty}^{+\infty} \mid u_{HCG_n}(\eta, z) \mid^2 d\eta}}, \tag{4.32}$$

where $u_{HCG_n}^{obs}(\eta, z)$ and $u_{HCG_n}(\eta, z)$ denote respectively, the beam field of the obstructed and unobstructed HCG_n.

Table 4.1: The similarity degree between the obstructed and the un-obstructed HCG_{10} beam, with $\alpha = 10$ in different propagation distances z, for three different values of δ. The underlined values correspond to the distance z_0

z	0.0	0.1	0.2	0.3	0.4	0.5
			$\delta = \mathbf{0.25}$			
S	0.97	<u>0.98</u>	0.99	0.99	0.99	0.99
			$\delta = \mathbf{1}$			
S	0.91	0.92	<u>0.93</u>	0.94	0.94	0.94
			$\delta = \mathbf{2}$			
S	0.78	0.84	0.88	0.91	<u>0.91</u>	0.92

The self-healing of the obstructed HCG_n beam is evaluated in Table 4.1, which presents the similarity degree between the obstructed and unobstructed HCG_{10} beam, of Cosine parameter $\alpha = 10$, for three sizes of obstruction at different planes. It can be seen that the distance z_0 (Eq. (4.31)), which the self-healing process based on, strongly depends on the obstruction size, where is increases with increasing the obstruction size, which in turn affects the similarity degree.

4.5 Conclusion

In this chapter, we have studied the propagation features of the Cosine-Gauss beams. We have demonstrated that the Cosine-Gauss beams from fundamental (CG) to higher orders (HCG_n) are standing nondiffracting beams in a certain region resulting from the interference of two oppositely oblique traveling waves. We have described analytically the z_{max} region where they are considered nondiffracting including their spatial extent W_n, where we have found that they depend on the CG beam parameter α. Since the CG beams are nondiffracting, we have demonstrated their ability to self-heal and recover when encountering obstacles, where we have introduced a simple expression for the farthest

distances from which CG beam would self-reconstruct.

Chapter 5

The diffraction-free nature of elegant Gaussian beams

The current chapter contains extracts from a publication by *Chabou et al* [108].

5.1 Introduction

The diffraction is a limiting issue in many applications when one wishes to have propagation lengths where the transverse dimensions of the light field do not expand appreciably. Only the non-diffracting beams have this immunity to free space diffraction, as discussed in the previous chapter [109].

In this chapter, we will demonstrate that also the elegant Gaussian beams can be considered pseudo-nondiffracting beams under certain circumstances. In which we will show that the elegant Gaussian beams in cartesian (elegant Hermite-Gauss) and cylindrical (elegant Laguerre-Gauss) coordinates are asymptotically equivalent to pseudo-nondiffracting beams (pNDB) in the same coordinates (Cosine-Gauss (CG) and Bessel-Gauss (BG), respectively). We will present a theoretical comparison of their intensities distribution at different planes without and with obstruction, which allows discussing the diffraction-free nature and self-healing property.

5.1.1 The relationship between the pseudo-nondiffracting beams and the elegant-Gaussian beams

In this section, we demanstrate the relation between an elegant Gaussian beam and a pseudo-nondiffracting beam in two coordinates system, the cartesian coordinates (eHG to CG) and the cylindrical coordinates (eLG to BG), based on an asymptotic behavior supported by a quantitative examination.

Let our analysis comparing eGB with pseudo-nondiffracting beams (BGB, CGB) start with the asymptotic expressions of the two famous orthonormal polynomials, the Hermite H_n and Laguerre polynomials $L_p^{|l|}$.

The Hermite polynomials behave asymptotically for large values of n as a cosine function multiplied by a Gaussian, given as follows [110, 111] :

$$H_n(x') \approx 2^{(n+1)/2} n^{n/2} e^{-n/2} e^{-x'^2/2} \cos\left(\sqrt{2n+1}x' - \frac{n\pi}{2}\right) \tag{5.1}$$

with $x' = \sqrt{2}x/w(z)$.

In the other side, the asymptotic representation of the Laguerre polynomials for large p is defined as[73, 110]:

$$\begin{aligned} e^{-r^2/w^2(z)} \left(\frac{\sqrt{2}r}{w(z)}\right)^{|l|} L_p^{|l|}\left(\frac{2r^2}{w^2(z)}\right) \approx \\ \frac{\Gamma(p+|l|+1)}{p!\left(p+\frac{|l|+1}{2}\right)^{|l|/2}} J_l\left(2\sqrt{2\left(p+\frac{|l|+1}{2}\right)}\frac{r}{w(z)}\right) \end{aligned} \tag{5.2}$$

By multiplying both sides of the two previous equations, Eqs. (5.1,5.2), by the Gaussian factor, and after some arrangemment, we get the following asymptotic formulas:

Eq. (5.1) becomes

$$H_n\left(\frac{x}{w'(z)}\right)e^{-x^2/w'^2(z)} \approx \\ 2^{(n+1)/2}n^{n/2}e^{-n/2}e^{-x^2/2w'^2(z)}\cos\left(\sqrt{(2n+1)}\frac{x}{w'(z)}-\frac{n\pi}{2}\right) \tag{5.3}$$

and Eq. (5.2) becomes

$$e^{-r^2/w'^2(z)}\left(\frac{r}{w'(z)}\right)^{|l|}L_p^{|l|}\left(\frac{r^2}{w'^2(z)}\right) \approx \frac{\Gamma(p+|l|+1)}{p!\left(p+\frac{|l|+1}{2}\right)^{|l|/2}} \\ e^{-r^2/2w'^2(z)}J_l\left(2\sqrt{\left(p+\frac{|l|+1}{2}\right)}\frac{r}{w'(z)}\right) \tag{5.4}$$

Here $w'^2(z) = w^2(z)/2$.

It can be noticed, from the two obtained asymptotic formulas Eqs. (5.3,5.4), that the elegant Gaussian beams are asymptotically equal to pseudo-nondiffracting beams.

5.1.2 Propagation path comparison

In the following the Fresnel– Kirchhoff diffraction integral, discussed in the second chapter, is used to investigate the beam propagation in free space and after encountering an obstacle. Its mathematical expression in cartesian and cylindrical coordinates systems, respectively, is given after some simplifications by

$$u_{out}(\xi,z) = \left(\frac{1}{i\lambda z}\right)^{1/2}\int_{-\infty}^{+\infty}u_{in}(x,z=0)\exp\left[\frac{i\pi}{\lambda z}(\xi-x)^2\right]dx \tag{5.5}$$

$$u_{out}(\rho, z) = \frac{1}{i\lambda z}\int_0^\infty u_{in}(r, z=0) J_0\left(\frac{2\pi}{\lambda z}\rho r\right) \exp\left[\frac{i\pi}{\lambda z}\left(r^2+\rho^2\right)\right] r dr \tag{5.6}$$

We consider an eHG beam and an eLG beam, respectively, as inputs (u_{in}), of which their optical fields can be expressed as:

$$u_{in}^{eHG}(x, z=0) = H_n\left(\frac{x}{w'(z)}\right) \exp\left(-\frac{x^2}{w'^2(z)}\right) \tag{5.7}$$

$$u_{in}^{eLG}(r, z=0) = L_p^0\left(\frac{r^2}{w'^2(z)}\right) \exp\left(-\frac{r^2}{w'^2(z)}\right) \tag{5.8}$$

The optical field of their equivalent pseudo-nondiffracting beams can be expressed, respectively, as follows:

$$u_{in}^{CG}(x, z=0) = cos\left(\frac{\sqrt{2n+1}}{w'(z)}x\right) \exp\left(-\frac{x^2}{2w'^2(z)}\right) \tag{5.9}$$

$$u_{in}^{BG}(r, z=0) = J_0\left(\frac{\sqrt{4p+2}}{w'(z)}r\right) \exp\left(-\frac{r^2}{2w'^2(z)}\right) \tag{5.10}$$

Because the on-axis intensity plays an important role in studying nondiffracting beams, we start by comparing it in order to investigate the obtained equality (Eq. 5.3 and Eq. 5.4) between the elegant Gaussian beams and the pseudo-nondiffracting beams. Figure 5.1 shows the behavior of the intensity in the plane $\xi - z$ of the compared beams in the top row and their on-axis intensity distribution in the bottom row for the Cartesian beams on

the left side (eHG and CG) and for the cylindrical beams on the right side (eLG and BG). It can be seen that the behavior of the two compared beams, in both cases, is selfsame.

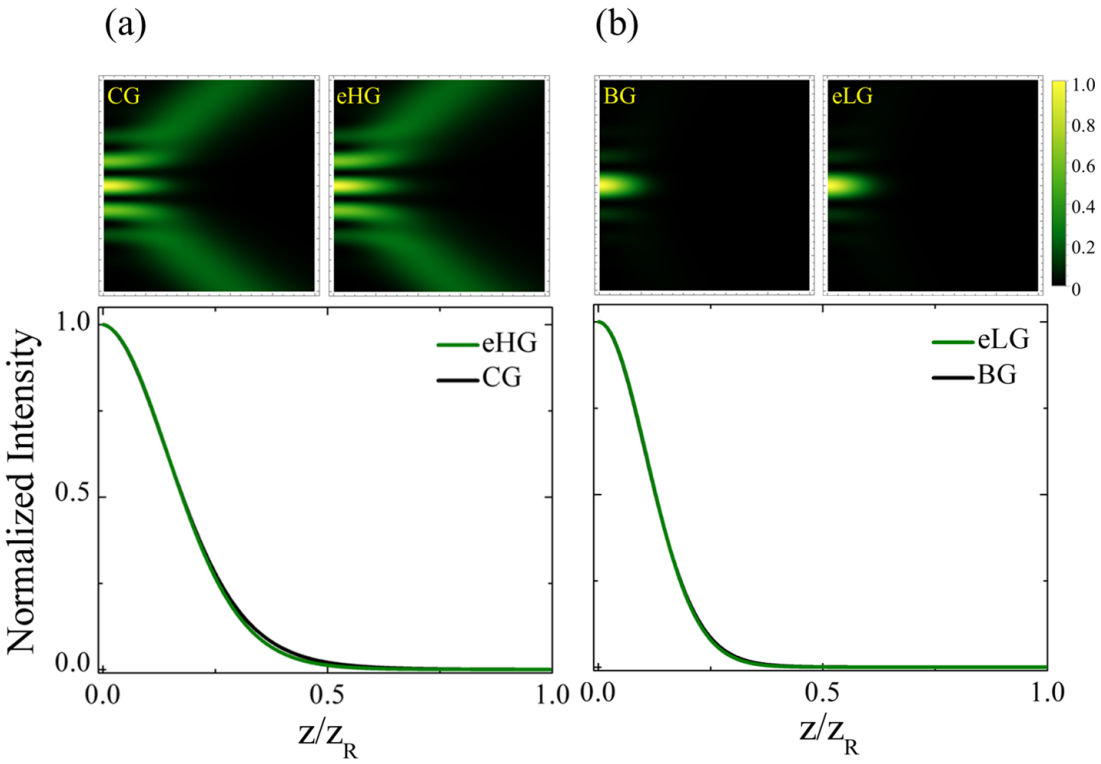

Figure 5.1: The density plots in the plane $\xi - z$ (top row) and the on-axis intensity distribution (bottom row) of the (a) eHG beam ($n = 10$) and the equivalent CG beam, (b)the eLG beam ($p = 10$, $l = 0$) and the equivalent BG beam.

5.1.3 Transverse shape comparison

The equivalence of two beams can be, also, expressed in terms of the similarity of their transverse behavior. In this section, we investigate the analogy between the elegant Gaussian beams and the pseudo-nondiffracting beams at the waist plane ($z = 0$) and the Fourier plane ($z = f$).

The Fourier plane corresponds to the focal plane of a lens. The optical fields of the eGB and the pNDB at the far-field are analytically described, using Fresnel Kirchhoff

diffraction integral ((Eq. 5.5 and Eq. 5.6)), by[77, 112–114]:

$$\begin{aligned} u_{out}^{eHG}(\xi, z=f) &= \int_{-\infty}^{+\infty} u_{in}^{eHG}(x, z=0) \exp\left[-\frac{i2\pi}{\lambda f}\xi x\right] dx \\ &= \sqrt{\pi}\left(\frac{i2\pi\xi w'(z)}{\lambda f}\right)^{n} \exp\left(\frac{-\pi^2\xi^2 w'^2(z)}{\lambda^2 f^2}\right) \end{aligned} \tag{5.11}$$

$$\begin{aligned} u_{out}^{CG}(\xi, z=f) &= \int_{-\infty}^{+\infty} u_{in}^{CG}(x, z=0) \exp\left[\frac{-i2\pi}{\lambda f}\xi x\right] dx \\ &= \frac{2\pi w'^2(z)}{\lambda^2} \exp\left(-(4n+2)\right) \exp\left(-\frac{2\pi^2 w'^2(z)}{\lambda^2 f^2}\xi^2\right) \cosh\left(\frac{2\sqrt{2n+1}\pi w'(z)}{\lambda f}\xi\right) \end{aligned} \tag{5.12}$$

$$\begin{aligned} u_{out}^{eLG}(\rho, z=f) &= \int_{0}^{\infty} u_{in}^{eLG}(r, z=0) J_0\left(\frac{2\pi}{\lambda f}\rho r\right) r dr \\ &= \frac{1}{2}(-1)^p w'^2(z) \exp\left(-\frac{\pi^2\rho^2 w'^2(z)}{\lambda^2 f^2}\right) L_p^{-p}\left(\frac{\pi^2\rho^2 w'^2(z)}{\lambda^2 f^2}\right) \end{aligned} \tag{5.13}$$

$$\begin{aligned} u_{out}^{BG}(\rho, z=f) &= \int_{0}^{\infty} u_{in}^{BG}(r, z=0) J_0\left(\frac{2\pi}{\lambda f}\rho r\right) r dr \\ &= 2w'^2(z) \exp\left(-\frac{(2p+1)}{4}\right) I_0\left(\frac{\sqrt{4p+2}\pi\rho w'(z)}{\lambda f}\right) \exp\left(-\frac{2w'^2(z)\pi^2\rho^2}{\lambda^2 f^2}\right) \end{aligned} \tag{5.14}$$

where$I_0(.)$ is the zero-order first-kind modified Bessel function.

Eq. (5.11) and Eq. (5.12) represent the far-field of both the elegant Hermite-Gauss beam and its equivalent Cosine-Gauss beam, respectively. As Eq. (5.13) and Eq. (5.14) represent the far-fields of the elegant Laguerre-Gauss beam and its equivalent Bessel-Gauss beam.

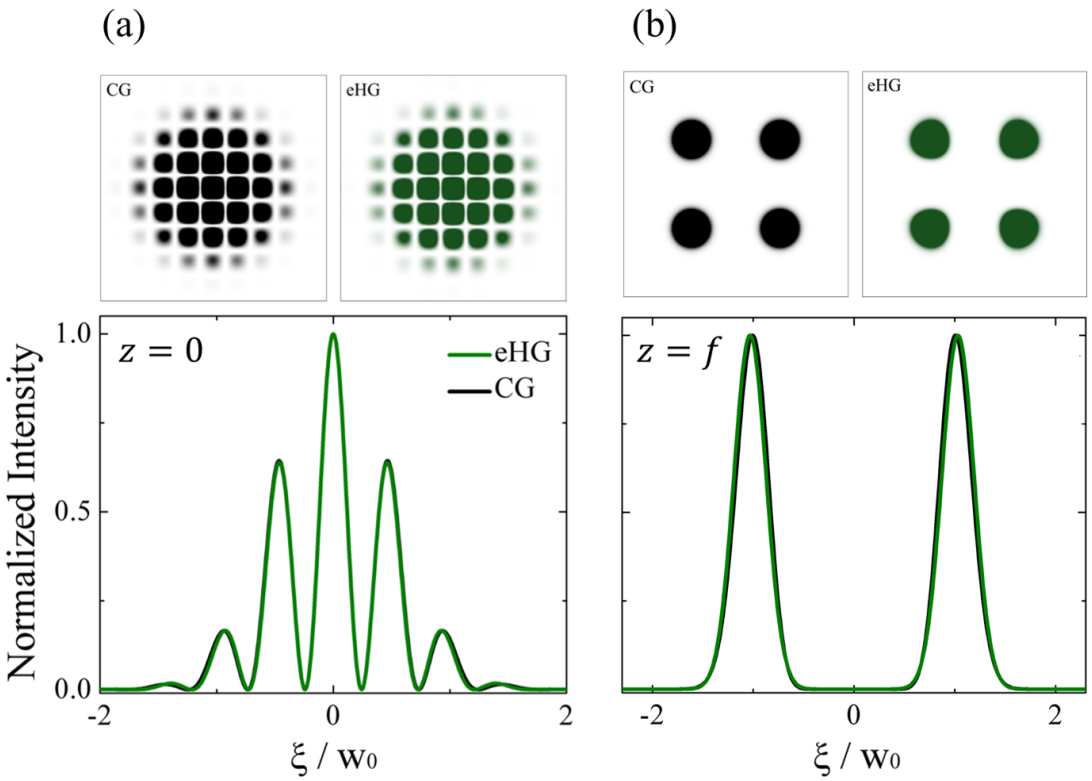

Figure 5.2: The intensity profiles (top row) and the transverse cross-sections (bottom row) of the eHG beam ($n = 10$) and its corresponding CG beam, (a) at the initial plane ($z = 0$) and (b) at the far-field ($z = f$).

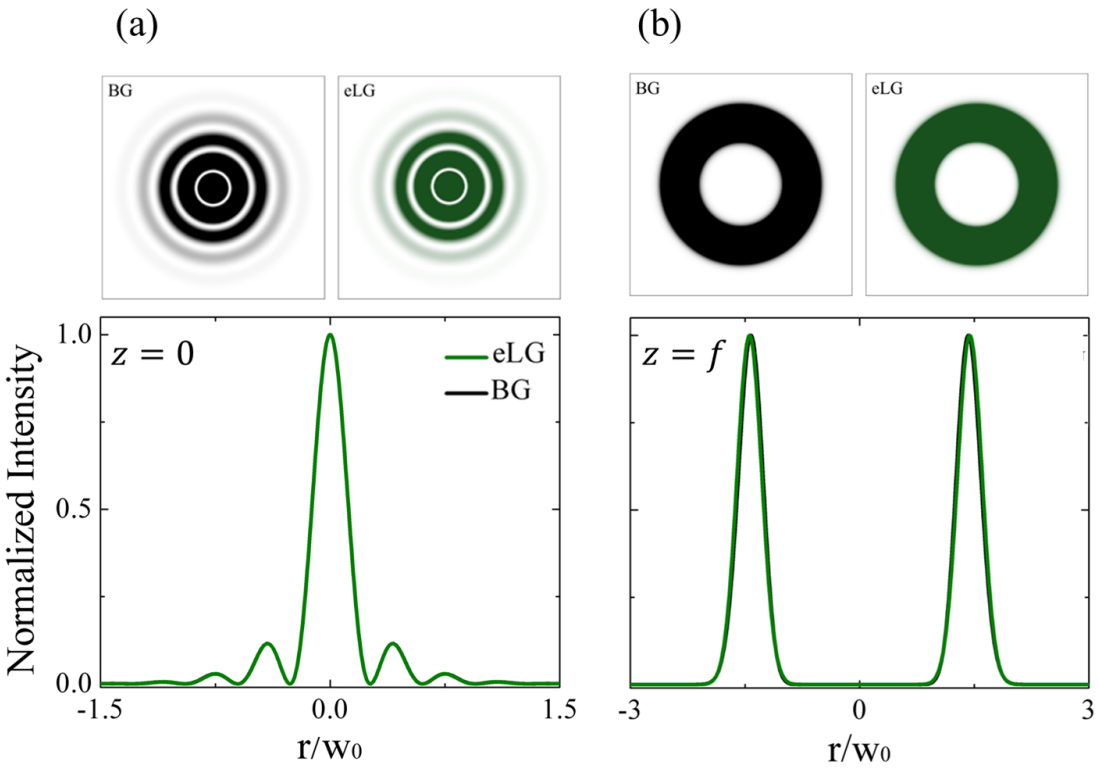

Figure 5.3: The intensity profiles (top row) and the transverse cross-sections (bottom row) of the eLG beam ($p = 10$) and its corresponding BG beam, (a) at the initial plane ($z = 0$) and (b) at the far-field ($z = f$).

In Figure 5.2 (Figure 5.3), the transverse behavior of elegant Gaussian beams and the equivalent pseudo-nondiffracting beams is compared at two different planes. Figure 5.2 (Figure 5.3) shows the intensity profiles (top) and transverse cross-sections (bottom) of the elegant Hermite-Gauss beam of order $n = 10$ (elegant Laguerre-Gauss beam of order $p = 10$) and its corresponding Cosine-Gauss beam (Bessel-Gauss beam), at the waist plane $z = 0$ on the left side (Figure 5.2(a) (Figure 5.3(a))) and at the Fourier plane $z = f$ on the right side (Figure 5.2(b) (Figure 5.3(b))). As is visible from Figure 5.2 (Figure 5.3), the transverse behavior of the two compared beams is identical. (Figure 5.4 (Figure 5.5)) presents the 3D intensity profiles, in which the eGB and the pNDB are indistinguishable.

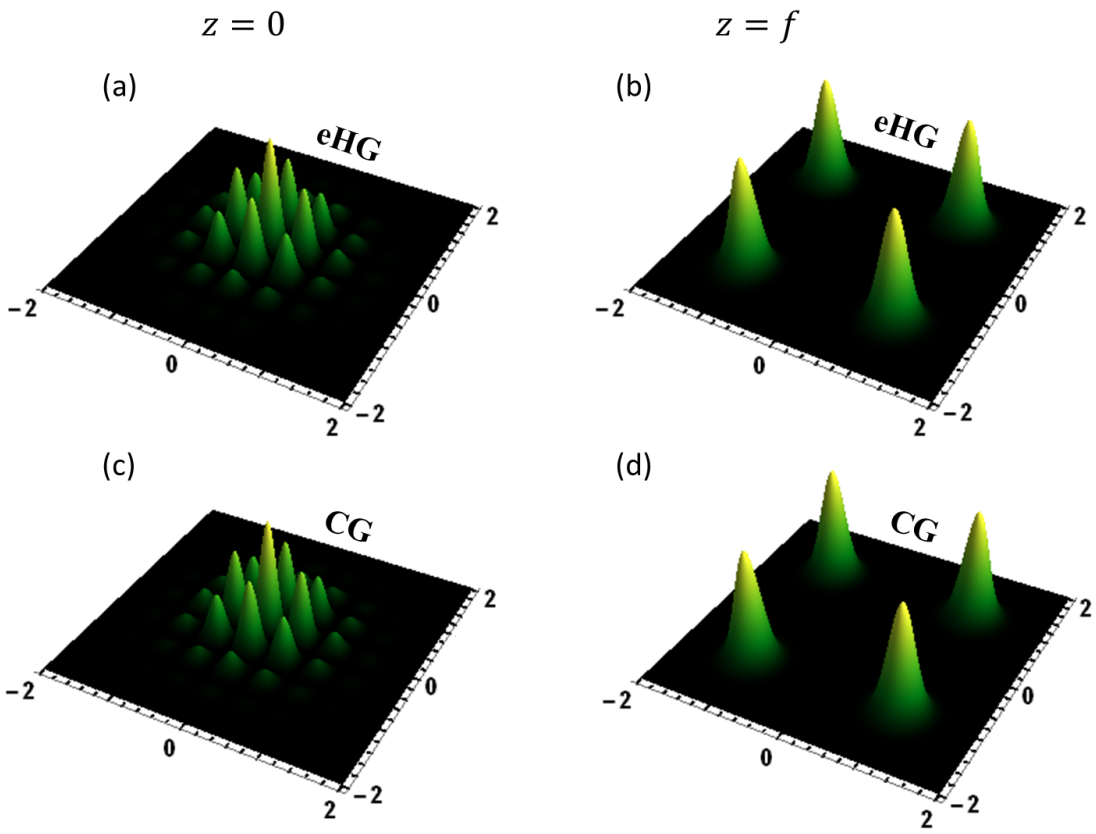

Figure 5.4: The 3D intensity profiles of the eHG beam ($n = 10$) and its corresponding CG beam, at the initial plane ($z = 0$) on the left side and at the far-field ($z = f$) on the right side.

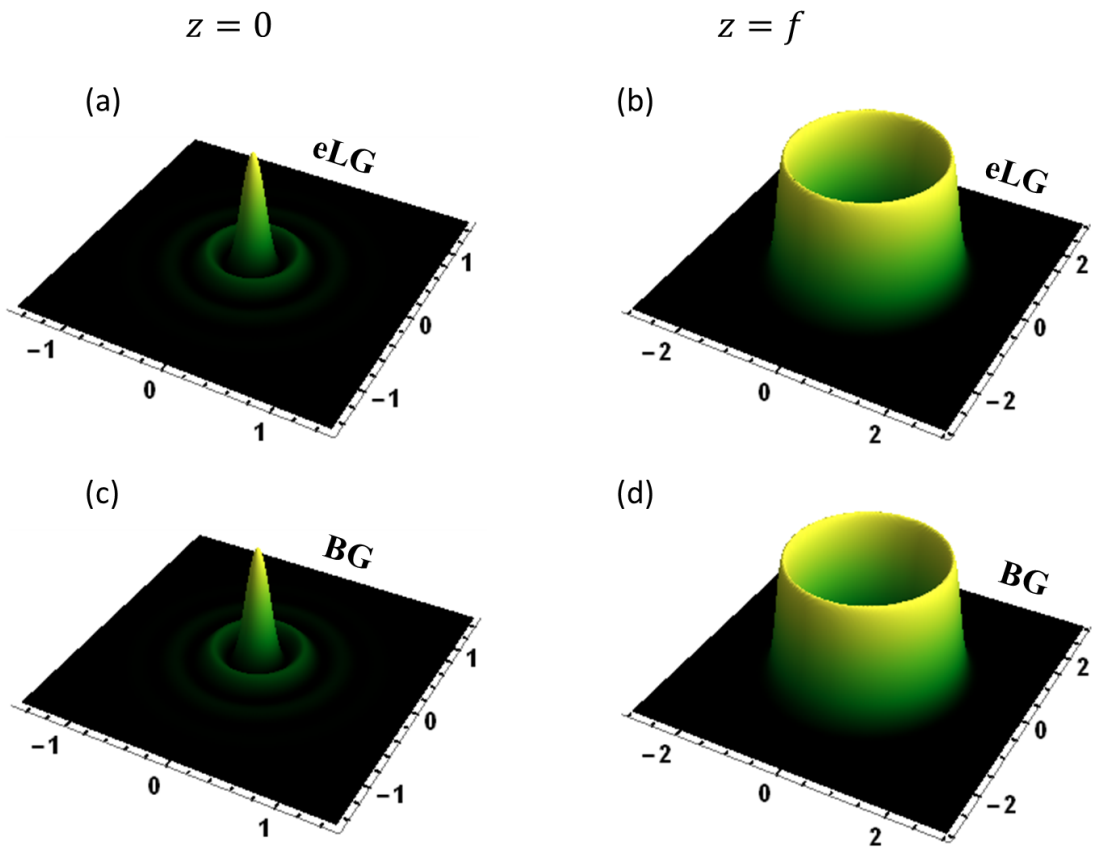

Figure 5.5: The 3D intensity profiles of the eLG beam ($p = 10$) and its corresponding BG beam, at the initial plane ($z = 0$) on the left side and at the far-field ($z = f$) on the right side.

5.1.4 Quantitative comparison

From previous sections, it was shown for a beam order (n and p) equals 10 that the $eGBs$ are similar to $pNDBs$. In the present section, in order to check this similarity for different beam orders and to quantitatively describe the relationship between these two classes of beams, we apply the similarity degree S, used in the previous chapters, as follows:

$$S = \frac{\int_{-\infty}^{+\infty} u_{eHG}(x,n,z)\, u^{*}_{CG}(x,n,z)dx}{\sqrt{\int_{-\infty}^{+\infty} u_{eHG}(x,n,z)\, u^{*}_{eHG}(x,n,z)dx}\,\sqrt{\int_{-\infty}^{+\infty} u_{CG}(x,n,z)\, u^{*}_{CG}(x,n,z)dx}}. \qquad (5.15)$$

$$S = \frac{\int_0^\infty u_{eLG}(r,p,z)\, u^*_{BG}(r,p,z) r dr}{\sqrt{\int_0^\infty u_{eLG}(r,p,z)\, u^*_{eLG}(r,p,z) r dr}\, \sqrt{\int_0^\infty u_{BG}(r,p,z)\, u^*_{BG}(x,p,z) r dr}}. \tag{5.16}$$

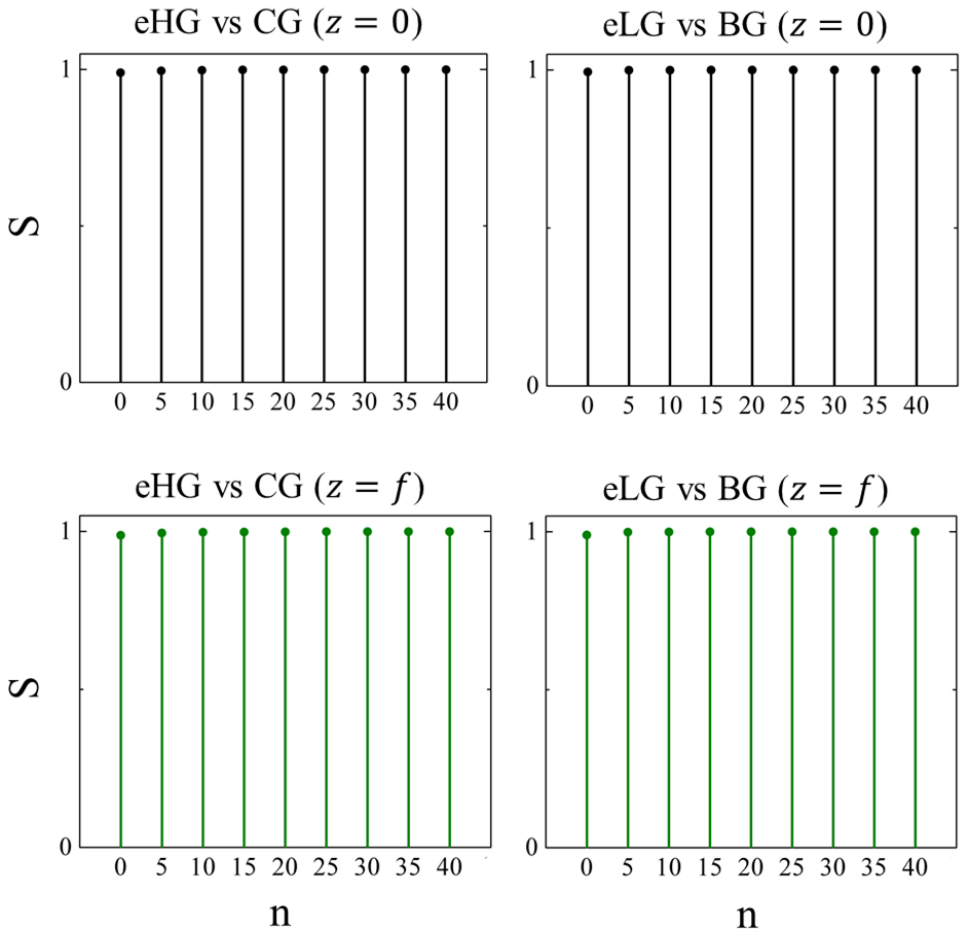

Figure 5.6: Illustration of similarity degree between the two classes of beams at $z = 0$ (top) and at $z = f$ (bottom). (a) The elegant Hermite-Gauss beam and its equivalent Cosine-Gauss beam, (b) the elegant Laguerre-Gauss beam and its equivalent Bessel-Gauss beam. For all the presented beam orders n and in both cases, the value of similarity degree is about 0.99.

Figure 5.6 shows the degree of similarity between the elegant Hermite-Gauss beam (elegant Laguerre-Gauss beam) and its equivalent Cosine-Gauss beam (Bessel-Gauss beam) at the initial plane (top) and at the far-field (bottom). As seen in Figure 5.6, the simi-

larity degree, for the different beam orders, between the two compared beams is almost reaching its maximum ($S \approx 1$) in both cases, eHG (Figure 5.6(a) and (c)) and eLG (Figure 5.6(b) and (d)). This indicates that the elegant Gaussian beams and pseudo-nondiffracting beams are perfectly identical.

For more clarification, the propagation features of the elegant Gaussian beams are investigated and analyzed in the following sections.

5.2 Non diffracting nature of elegant Gaussian beams

This section is devoted to investigating an important feature of the pseudo-nondiffracting beams, which is the propagation-invariance of its transverse intensity profile, for the elegant-Gaussian beams. Where the maximum distance within which the elegant-Gaussian beams remain nondiffracting is estimated.

Within the framework of the connection between the elegant Gaussian beams and the pseudo-nondiffracting beams, demonstrated above, the diffraction free rang z_{max} , illustrated in Figure2.4 of the second chapter, of the eGBs can be investigated using the Eq. 4.5 of the previous chapter, which is given by

$$z_{max} = a\frac{k}{k_\xi}, \tag{5.17}$$

with a is the beam width and k the wave number.

In the case of eHG the beam width can be defined from Ref [115] ($Eq.(17)$) as follows:

$$a = \sqrt{w_e^2} = \sqrt{2w_0'^2 \frac{4n-1}{4(2n-1)}}, \tag{5.18}$$

and k_ξ can be deduced from the asymptotic formula of Eq.5.3 as follows:

$$k_\xi = \frac{\sqrt{2n+1}}{w_0'}, \tag{5.19}$$

The final expression z_{max} of elegant Hermite-Gauss beams of order n, after normalization, is given by

$$\frac{z_{max}}{z_R} = \sqrt{\frac{8n-2}{(2n-1)(2n+1)}}. \tag{5.20}$$

While the final expression z_{max} of elegant Laguerre-Gauss beams of radial order p and azimuthal order l, after normalization, is given by

$$\frac{z_{max}}{z_R} = \sqrt{\frac{2p-l+l^2}{(2p+1)(2p+l)}}. \tag{5.21}$$

where the beam width a, using $Eq.(21)$ of Ref [116], and k_ξ , from the asymptotic formula of Eq.5.4, are defined as:

$$a = \sqrt{\sigma_0^2} = \sqrt{\frac{w_0'^2}{2}\frac{2p-l+l^2}{2p+l}}, \tag{5.22}$$

$$k_\xi = \frac{\sqrt{4p+2}}{w_0'}. \tag{5.23}$$

As shown from Eq. (5.20) and (5.21), the diffraction-free region, as known, depends only on the beam order. Figure 5.7 demonstrates the estimated nondiffracting range, of the propagated eHG beam in Figure 5.7(a) and propagated eLG beam in Figure 5.7(b), for different beam orders n. It can be seen from Figure 5.7 that the value of diffraction-free range z_{max} decreases with increasing the beam order (n and p).

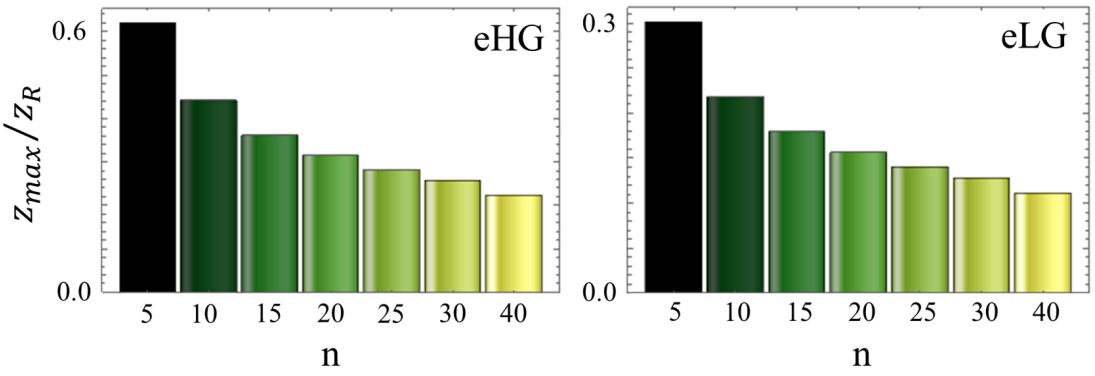

Figure 5.7: The normalized nondiffracting range z_{max}/z_R ,as a function of the beam order, for (a) elegant Laguerre-Gauss beam and (b) elegant Hermite-Gauss beam.

With the aim to validate our results about the diffraction-free range, the density plot in the plane $\xi - z$ of the propagated elegant-Gaussian beams in free space is plotted in Figure 5.8. Where Figure 5.8(a) presents a propagated eHG beam of order $n = 10$ whereas Figure 5.8(b) shows a propagated eLG beam of order $p = 10$ and $l = 0$.The yellow dashed line corresponds to the calculated z_{max}'s value, normalized to the Raleigh length z_R. It seems that the plot corresponds to the calculation in both presented beams.

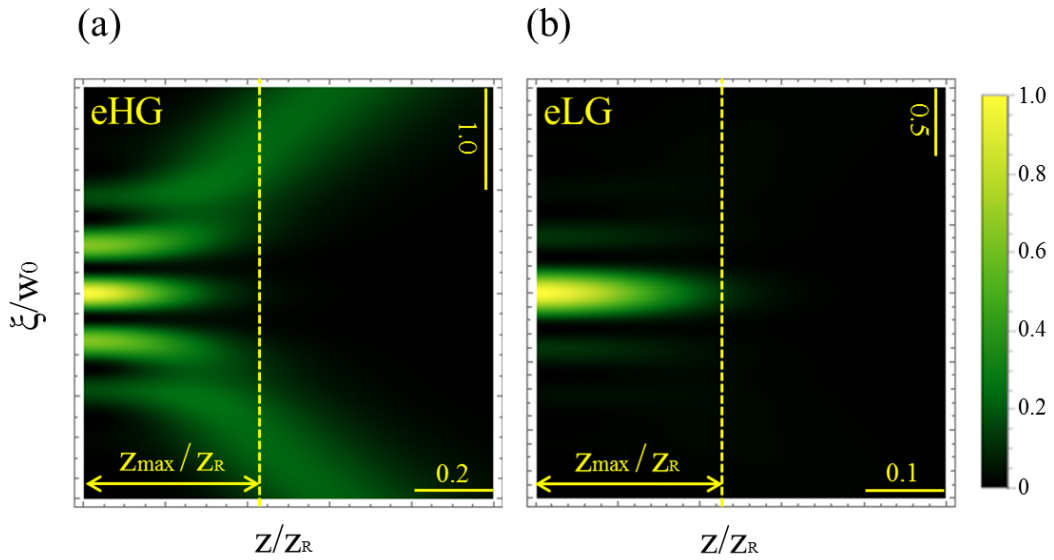

Figure 5.8: The density plot in the plane $\xi - z$ of the propagated (a) elegant Laguerre-Gauss beam and (b) elegant Hermite-Gauss beam, of beam order $p = n = 10$.

5.3 Self-healing ability of elegant Gaussian beams

In this section, one more feature of the pseudo-nondiffracting beams, which is the self-healing ability discussed in the first chapter, is analyzed for the elegant Gaussian beams. In order to illustrate the elegant Gaussian beam's ability to heal itself after encountering an obstacle (an opaque obstruction), the density plot in the plane $\xi - z$, transverse intensity patterns, and the corresponding profiles, of the obstructed beam, are plotted.

Before starting the analysis and since the two-beam classes are equivalent, we can obtain z_{min} that defines the minimum distance before reconstruction occurs, illustrated in Fig.2.4 of the second chapter, as follows [35, 59]:

$$z_{min} = \delta \frac{k}{k_\xi}, \tag{5.24}$$

with δ is the obstacle size.

Figure 5.9 shows the behavior, in the plane $\xi - z$, of the obstructed elegant Hermite-Gauss beam ($n = 10$) by a small size's obstacle in Figure 5.9(a) and by a big size's obstacle in Figure 5.9(b), with displaying a cross-section of the obstructed beam at the plane where the reconstruction occurs. In both cases of Figure 5.9(a) and (b) for sake of simplicity, the obstacle size was chosen to coincide with the zeros of the beam's intensity, where in Figure 5.9(a) the obstacle obstructs the beam on its first intensity zero while in Figure 5.9(b) it obstructs the beam on its third intensity zero. The illustrated plane by the yellow dashed line corresponds to the minimum distance z_{min} after which the self-healing process occurs.

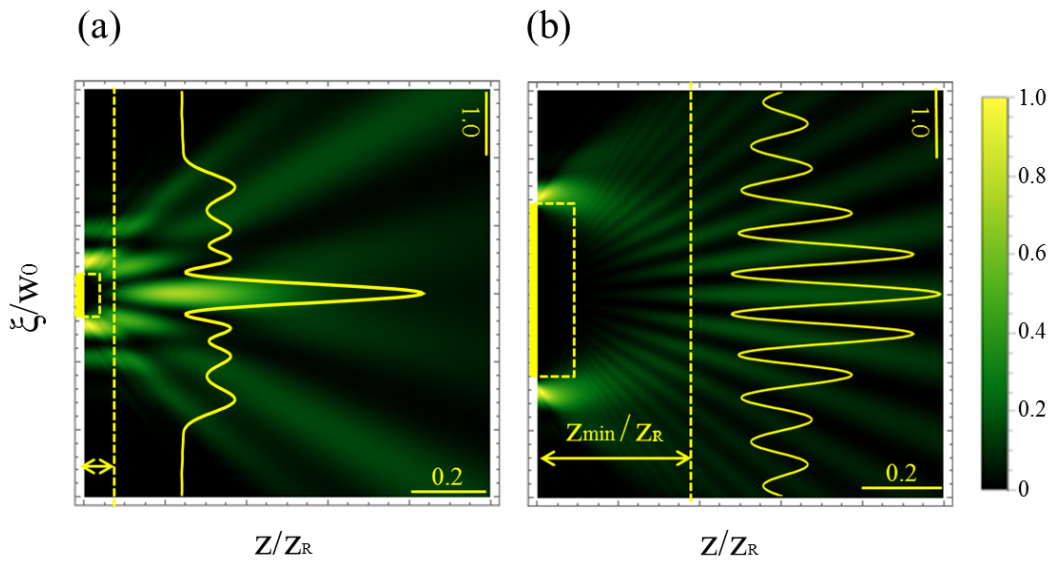

Figure 5.9: (color online) The density plot in the plane $\xi - z$ of the obstructed elegant Hermite-Gauss beam ($n = 10$) by (a) a small obstacle and (b) a big obstacle, with showing the minimum distance z_{min} before the reconstruction occurs. The bold yellow line at the initial plane denotes the size and the position of the obstacle, while the dotted half-rectangle indicates the shadow region.

The same analysis is also performed for an elegant Laguerre Gaussian beam of order $p = 10$ and $l = 0$, in Figure 5.10.

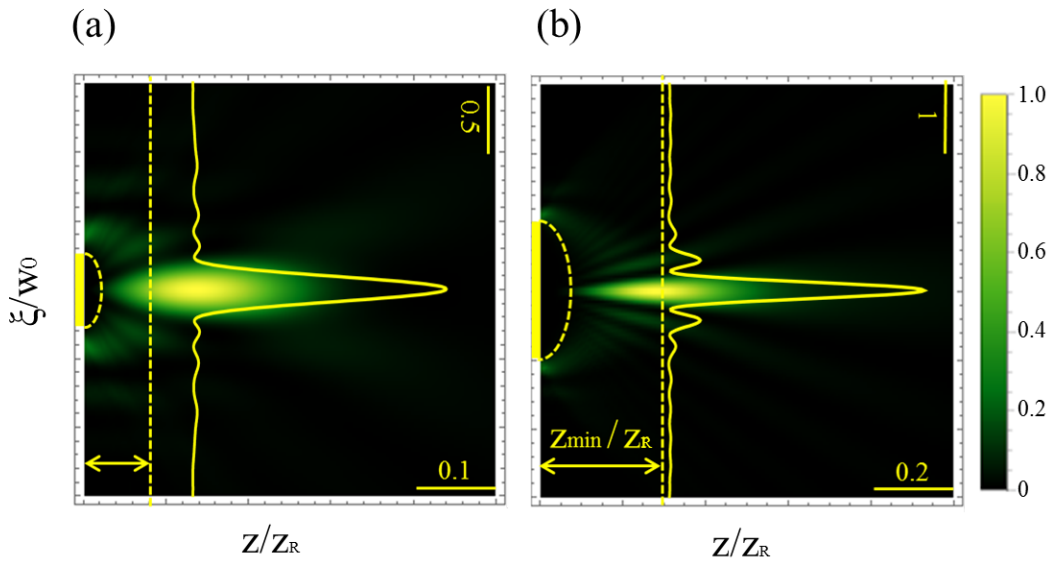

Figure 5.10: The density plot in the plane $\xi - z$ of the obstructed elegant Laguerre-Gauss beam ($p = 10$)by (a) a small obstacle and (b) a big obstacle, with showing the minimum distance z_{min} before reconstruction occurs. The bold yellow line at the initial plane denotes the size and the position of the obstacle, while the dotted half-circle indicates the shadow region.

The un-obstructed and obstructed on-axis intensities are plotted for the two obstruction's sizes; in Figure 5.11(a) for eHG beam and in Figure 5.11(b) for eLG beam. It can be seen that the shift of the on-axis intensity maximum increases as the obstruction's size increases. The latter could be used as an indicator of the self-healing distance.

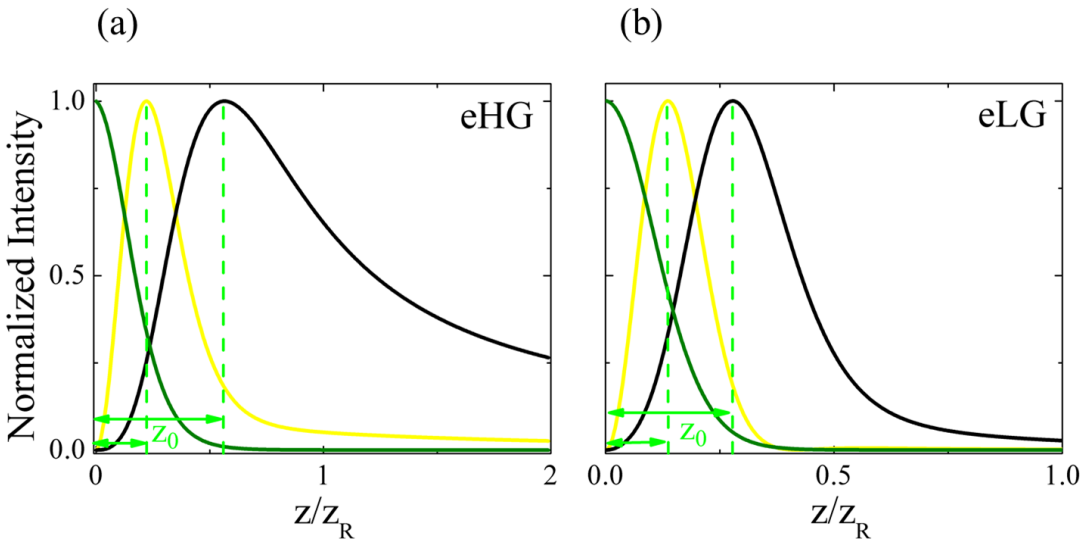

Figure 5.11: The on-axis intensity distribution of unobstructed beam (green curve) and obstructed beam by small (yellow curve) and big obstacle (black curve). (a) eHG beam of beam order $n = 10$, (b) eLG beam of beam order $p = 10$. The plane z_0 is the plane corresponding to the on-axis intensity maximum.

Figure 5.12 shows the intensity patterns (top row) and their corresponding transverse profiles (middle row) of the obstructed eHG beam by a small obstacle on the left side and by a big obstacle on the right side; at the obstacle plane (Figure 5.12(a) and (c)) and at $z = z_0$ plane (Figure 5.12(b) and (d)). The last row presents a comparison between the obstructed eHG beam and its initial shape (yellow curve). It can be noticed in Figure 5.12(e) and (f) that the obstructed part (inner part) of the beam is reconstructed at $z = z_0$ plane in the case of a small obstacle and the case of a big obstacle.

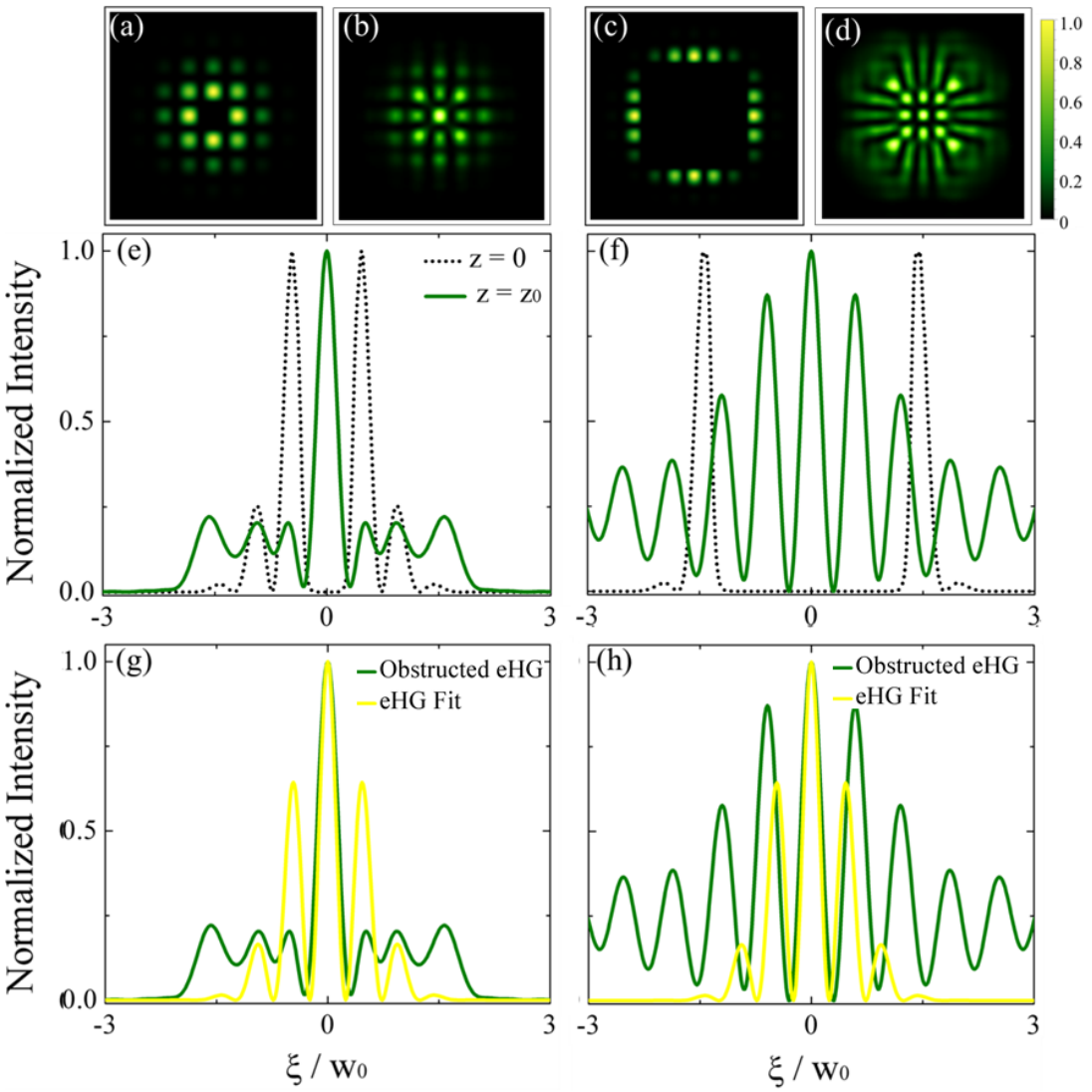

Figure 5.12: The intensity patterns and their corresponding profiles at the obstacle plane $z = 0$ (a,c) and at the $z = z_0$ plane (b,d) of obstructed eHG beam ($n = 10$), by a small (a,b) and big obstacle (c,d); showing the self reconstruction process. The obstructed eHG beam at the plane $z = z_0$ is compared with the un-obstructed one (yellow curve); shown in (g) and (h)

.

Figure 5.13 shows the intensity patterns (top row) and their corresponding transverse profiles (middle row) of the obstructed eLG beam by a small obstacle on the left side and by a big obstacle on the right side; at the obstacle plane (Figure 5.13(a) and (c)) and at $z = z_0$ plane (Figure 5.13(b) and (d)). The last row presents a comparison between the obstructed eLG beam and its initial shape (yellow curve). In that case, the obstructed

part (inner part), by a small obstacle and a big obstacle, is successfully reconstructed at the $z = z_0$ plane.

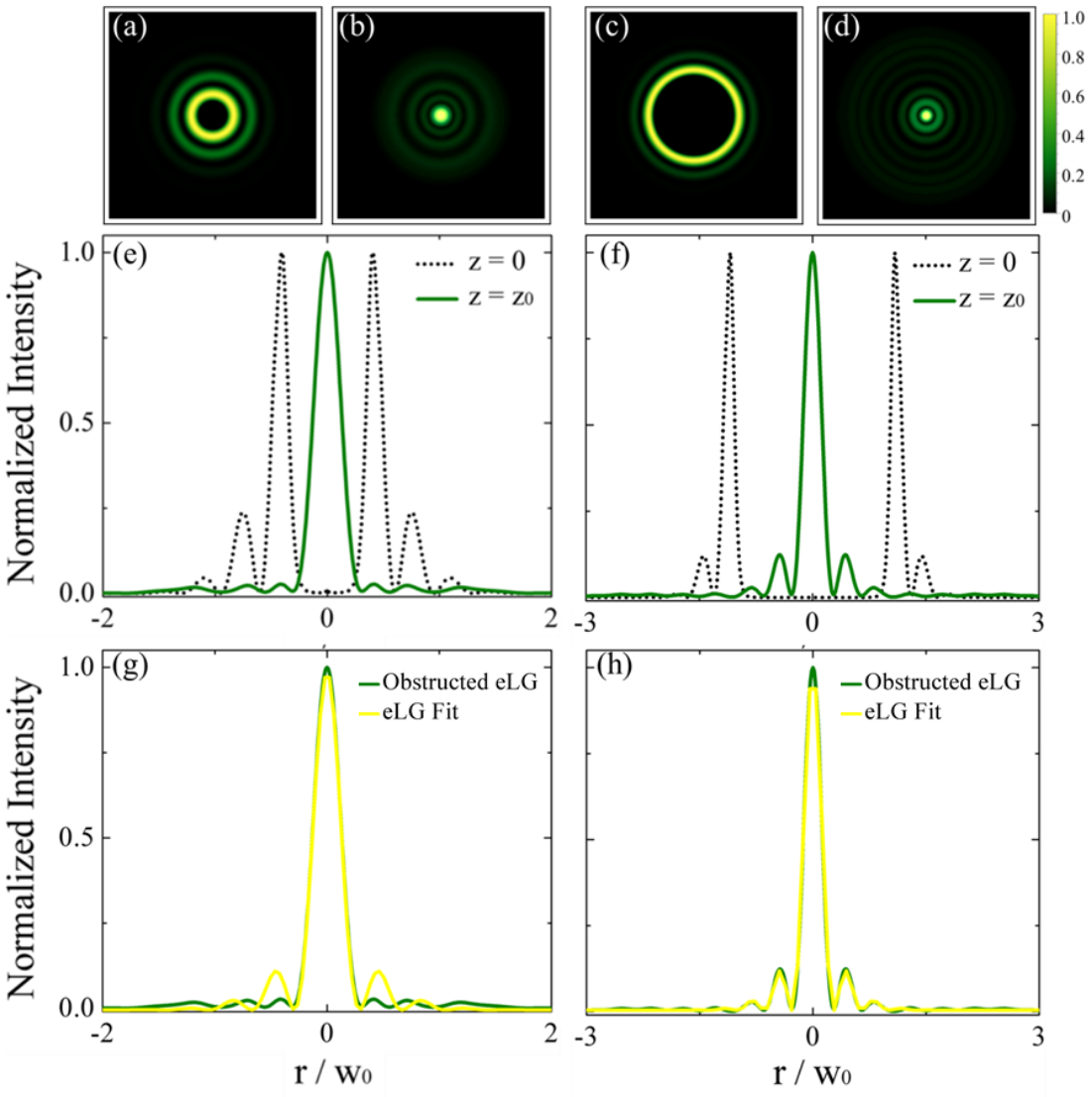

Figure 5.13: The intensity patterns and its corresponding profiles at the obstacle plane $z = 0$ (a,c) and at the $z = z_0$ plane (b,d) of obstructed eLG beam ($p = 10$), by a small (a,b) and big obstacle (c,d); showing the self reconstruction process. The obstructed eLG beam at the plane $z = z_0$ is compared with the un-obstructed one (yellow curve); shown in (g) and (h)

.

As seen from Figure 5.9 (Figure 5.10) and Figure 5.12 (Figure 5.13), the obstructed

elegant Gaussian beams can be reconstructed at the plane $z = z_0$ (which depends on the obstacle size) in both cases; small and big obstacle. In addition, Figures 5.11 – 5.13 indicate the dependence of the self-healing process of the obstructed beam on the obstacle size. Moreover, it can be seen from Figures 5.12(e) and (f) (Figures 5.13(e) and (f)), that when any beam is obstructed, its inner part is always reconstructed after some propagation, that also confirmed by plots presented in the Figures 5.12(g) and (h) (5.13(g) and (h)). This result was demonstrated recently in many papers using the concept of ray optics description of optical beams [117, 118]. When an obstructed optical beam is analyzed using a ray optics description, the inner rays are blocked, while the outer ones bypassing the obstacle and reconstruct (and focus) the beam, but at a further distance, which depends on the obstacle size and position.

With a view to quantitatively assess the self-healing ability of the elegant Gaussian beams (eHG and eLG), we calculate the power content percentage in the remaining part (unblocked part) of the blocked beam using the following expressions:

$$P = \frac{\int_{-\infty}^{-a}(u_{eHG}(x,n,z=0))^2dx + \int_{+a}^{+\infty}(u_{eHG}(x,n,z=0))^2dx}{\int_{-\infty}^{+\infty}(u_{eHG}(x,n,z=0))^2dx}. \tag{5.25}$$

$$P = \frac{\int_{0}^{a}(u_{eLG}(r,p,z=0))^2rdr}{\int_{0}^{\infty}(u_{eLG}(r,p,z=0))^2rdr}. \tag{5.26}$$

Table 5.1: Power content of obstructed beam

	obstacle size	power content (%)
elegant Hermite-Gauss beam		
small obstacle	$0.24w_0$	62.4
big obstacle	$1.24w_0$	1.19
elegant Laguerre-Gauss beam		
small obstacle	$0.26w_0$	59.1
big obstacle	$0.95w_0$	5.53

Table 5.1 exhibits the power content ratio of the blocked elegant Gaussian beams in the case of a small and a big obstacle. From Table 5.1 and Figures 5.9 and 5.10, it can be seen that the self-healing process occurs even after encountering an obstruction that blocks more than 95 % of their intensity.

5.4 Conclusion

In this chapter, we have studied the connection between the elegant Gaussian beams and the pseudo-nondiffracting beams in quantitative and qualitative terms. We have shown that the elegant Hermite-Gauss beam is equivalent to the Cosine Gauss beam as is the case for the elegant Laguerre-Gauss and Bessel Gauss beam. Moreover, we have discussed the diffraction-free nature of the elegant Gaussian beams by investigating their non-diffracting region and self-healing ability. All the obtained numerical results confirm that the two compared families are indistinguishable offering the same behavior. Thus, we have suggested perfect alternative beams to pseudo-nondiffracting beams that can be generated from a stable resonator.

Conclusions and outlooks

5.5 Conclusions

The work presented in this thesis aimed to characterize the propagation behavior of different laser beams that passing through diffractive optical elements; such as aperture, opaque disk, and prism. In chapter 1, definitions for some of the solutions to the paraxial Helmholtz wave equation discussed in this thesis such as Gaussian and higher-order Gaussian beams were given. We also present the spatial light modulator (SLM), the most commonly used device for such beams generation.

In chapter 2, we showed theoretically and experimentally the behavior of LG beams after encountering an aperture and an opaque disk. We assessed the impact of the truncation and the obstruction on the beam shape and the beam properties, where we evaluated two main beam characteristics that enclose the whole behavior of the beam (the beam propagation factor and the focal shift effect). In addition, we interpreted the diffractive effects of the two used elements on the LG beam shape based on the concept of spatial filtering.

As an extension of chapter 2, chapter 3 described a new method to solve analytically the far-field of diffracted LG beams, for which no exact analytical solution is known.We demonstrated that by imposing the right conditions, the inner part of an LG beam behaves as the same part of a Bessel beam (the truncated LG beam is equivalent to a truncated Bessel beam), while the outer part behaves as different ring shifted-Gaussian beams (equivalent to a vortex beam without charge).

Chapter 4 investigated the non-diffracting properties of a fundamental and higher-order Cosine Gauss beam, where we provided, in each case, an analytical expression for the region for which the beam being non-diffracting based on that of its spatial extent.
In chapter 5, we presented a study on the elegant Gaussian beams with particular emphasis on their asymptotic equivalence to pseudo-nondiffracting beams. Furthermore, we discussed their non-diffracting properties.

5.6 Future studies

The contributions in this thesis can lead to new lines of inquiry in different laser applications such as in optical communication, optical manipulation, and optical tweezers.
For homogeneous and inhomogeneous media, the use of a customized light such as non-diffracting and self-reconstructed modes like Bessel Gaussian and Cosine Gaussian beams yields successful applications. Among others; in optical communications, new light beam structures allow to increase the capacity of the carried information. In particle manipulation, a customized light gives more freedom degrees for manipulating particles through complex paths and media. In optical tweezers, such structured beams presented throughout the thesis could be used to create multi-traps for biological structures.

Bibliography

[1] A. Sabatyan and S. A. Hoseini, "Fresnel biprism as a 1d refractive axicon," *Optik*, vol. 124, no. 21, pp. 5046–5048, 2013.

[2] J. C. Maxwell, "A treatise on electricity and magnetism, (1954)," *United States*, 1891.

[3] S. BEA and M. Teich, ""fundamentals of photonics"," *Wiley*, p. 313, 1991.

[4] A. E. Siegman, "Lasers university science books," *Mill Valley, CA*, vol. 37, no. 208, p. 169, 1986.

[5] A. Siegman, "Hermite–gaussian functions of complex argument as optical-beam eigenfunctions," *JOSA*, vol. 63, no. 9, pp. 1093–1094, 1973.

[6] T. Takenaka, M. Yokota, and O. Fukumitsu, "Propagation of light beams beyond the paraxial approximation," *JOSA A*, vol. 2, no. 6, pp. 826–829, 1985.

[7] E. Zauderer, "Complex argument hermite–gaussian and laguerre–gaussian beams," *JOSA A*, vol. 3, no. 4, pp. 465–469, 1986.

[8] F. Gori, G. Guattari, and C. Padovani, "Bessel-gauss beams," *Optics communications*, vol. 64, no. 6, pp. 491–495, 1987.

[9] J. C. Gutiérrez-Vega and M. A. Bandres, "Helmholtz–gauss waves," *JOSA A*, vol. 22, no. 2, pp. 289–298, 2005.

[10] B. Boruah, "Dynamic manipulation of a laser beam using a liquid crystal spatial light modulator," *American Journal of Physics*, vol. 77, no. 4, pp. 331–336, 2009.

[11] A. Forbes, A. Dudley, and M. McLaren, "Creation and detection of optical modes with spatial light modulators," *Advances in Optics and Photonics*, vol. 8, no. 2, pp. 200–227, 2016.

[12] C. Rosales-Guzmán and A. Forbes, *How to shape light with spatial light modulators*. SPIE Press, 2017.

[13] V. Arrizón, U. Ruiz, R. Carrada, and L. A. González, "Pixelated phase computer holograms for the accurate encoding of scalar complex fields," *JOSA A*, vol. 24, no. 11, pp. 3500–3507, 2007.

[14] T. Ando, Y. Ohtake, N. Matsumoto, T. Inoue, and N. Fukuchi, "Mode purities of laguerre–gaussian beams generated via complex-amplitude modulation using phase-only spatial light modulators," *Optics letters*, vol. 34, no. 1, pp. 34–36, 2009.

[15] S. Chabou, A. Bencheikh, J. Pinnell, V. Rodríguez-Fajardo, and A. Forbes, "Do laguerre–gaussian beams recover their spatial properties after all obstacles?" *Applied Physics B*, vol. 126, no. 11, pp. 1–12, 2020.

[16] Y. Li and E. Wolf, "Focal shifts in diffracted converging spherical waves," *Optics Communications*, vol. 39, no. 4, pp. 211–215, 1981.

[17] W. H. Carter, "Focal shift and concept of effective fresnel number for a gaussian laser beam," *Applied optics*, vol. 21, no. 11, pp. 1989–1994, 1982.

[18] R. Wenzel, "Effect of the aperture–lens separation on the focal shift in large-f-number systems," *JOSA A*, vol. 4, no. 2, pp. 340–345, 1987.

[19] P. L. Greene and D. G. Hall, "Focal shift in vector beams," *Optics express*, vol. 4, no. 10, pp. 411–419, 1999.

[20] G. Zhou, "Focal shift of focused truncated lorentz-gauss beam," *JOSA A*, vol. 25, no. 10, pp. 2594–2599, 2008.

[21] S. Liu, P. Li, Y. Zhang, X. Gan, M. Wang, and J. Zhao, "Longitudinal spin separation of light and its performance in three-dimensionally controllable spin-dependent focal shift," *Scientific reports*, vol. 6, p. 20774, 2016.

[22] A. Siegman, "Analysis of laser beam quality degradation caused by quartic phase aberrations," *Applied optics*, vol. 32, no. 30, pp. 5893–5901, 1993.

[23] A. E. Siegman and J. Ruff, "Effects of spherical aberration on laser beam quality," in *Laser Energy Distribution Profiles: Measurement and Applications*, vol. 1834. International Society for Optics and Photonics, 1993, pp. 130–139.

[24] J. A. Ruff and A. Siegman, "Measurement of beam quality degradation due to spherical aberration in a simple lens," *Optical and quantum electronics*, vol. 26, no. 6, pp. 629–632, 1994.

[25] C. Mafusire and A. Forbes, "Generalized beam quality factor of aberrated truncated gaussian laser beams," *JOSA A*, vol. 28, no. 7, pp. 1372–1378, 2011.

[26] A. Bencheikh, M. Bouafia, and K. Ferria, "A new spherical aberration coefficient c 4 for the gaussian laser beam." *Optica Applicata*, vol. 41, no. 4, 2011.

[27] M. Stubenvoll, B. Schäfer, and K. Mann, "Measurement and compensation of laser-induced wavefront deformations and focal shifts in near ir optics," *Optics express*, vol. 22, no. 21, pp. 25 385–25 396, 2014.

[28] B. Boubaha, A. Bencheikh, and K. Aït-Ameur, "Spatial properties of rectified cosine gaussian beams," *Journal of Optics*, vol. 16, no. 2, p. 025701, 2014.

[29] M. Zhang, Y. Chen, Y. Cai, and L. Liu, "Effect of the correlation function on the focal shift of a partially coherent beam," *JOSA A*, vol. 33, no. 12, pp. 2509–2515, 2016.

[30] L. Meng, Z. Huang, Z. Han, H. Shen, and R. Zhu, "Simulation and experiment studies of aberration effects on the measurement of laser beam quality factor (m2)," *Optics and Lasers in Engineering*, vol. 100, pp. 226–233, 2018.

[31] K. Mihoubi, A. Bencheikh, and A. Manallah, "The beam propagation factor m2 of truncated standard and elegant-hermite-gaussian beams," *Optics & Laser Technology*, vol. 99, pp. 191–196, 2018.

[32] M. Born and E. Wolf, *Principles of optics: electromagnetic theory of propagation, interference and diffraction of light.* Elsevier, 2013.

[33] T. Li, "Diffraction loss and selection of modes in maser resonators with circular mirrors," *The Bell System Technical Journal*, vol. 44, no. 5, pp. 917–932, 1965.

[34] J. Taché, "Derivation of abcd law for laguerre-gaussian beams," *Applied optics*, vol. 26, no. 14, pp. 2698–2700, 1987.

[35] I. A. Litvin, M. G. McLaren, and A. Forbes, "A conical wave approach to calculating bessel–gauss beam reconstruction after complex obstacles," *Optics Communications*, vol. 282, no. 6, pp. 1078–1082, March 2009.

[36] M. Anguiano-Morales, M. M. Mendez-Otero, M. D. Iturbe-Castillo, and S. Chávez-Cerda, "Conical dynamics of bessel beams," *Optical Engineering*, vol. 46, no. 7, p. 078001, 2007.

[37] J. Durnin, J. Miceli Jr, and J. Eberly, "Diffraction-free beams," *Physical review letters*, vol. 58, no. 15, pp. 1499–1502, 1987.

[38] D. McGloin and K. Dholakia, "Bessel beams: diffraction in a new light," *Contemporary Physics*, vol. 46, no. 1, pp. 15–28, 2005.

[39] S. H. Tao and X. Yuan, "Self-reconstruction property of fractional bessel beams," *JOSA A*, vol. 21, no. 7, pp. 1192–1197, July 2004.

[40] X. Chu, "Analytical study on the self-healing property of bessel beam," *The European Physical Journal D*, vol. 66, no. 10, p. 259, October 2012.

[41] I. Litvin, L. Burger, and A. Forbes, "Self-healing of bessel-like beams with longitudinally dependent cone angles," *Journal of Optics*, vol. 17, no. 10, p. 105614, September 2015.

[42] J. Broky, G. A. Siviloglou, A. Dogariu, and D. N. Christodoulides, "Self-healing properties of optical airy beams," *Optics Express*, vol. 16, no. 17, pp. 12 880–12 891, August 2008.

[43] M. Anguiano-Morales, A. Martínez, M. D. Iturbe-Castillo, S. Chávez-Cerda, and N. Alcalá-Ochoa, "Self-healing property of a caustic optical beam," *Applied optics*, vol. 46, no. 34, pp. 8284–8290, December 2007.

[44] P. Zhang, Y. Hu, T. Li, D. Cannan, X. Yin, R. Morandotti, Z. Chen, and X. Zhang, "Nonparaxial mathieu and weber accelerating beams," *Physical review letters*, vol. 109, no. 19, p. 193901, November 2012.

[45] V. Arrizón, D. Aguirre-Olivas, G. Mellado-Villaseñor, and S. Chávez-Cerda, "Self-healing in scaled propagation invariant beams," *arXiv preprint arXiv:1503.03125*, March 2015.

[46] I. A. Litvin, L. Burger, and A. Forbes, "Angular self-reconstruction of petal-like beams," *Optics letters*, vol. 38, no. 17, pp. 3363–3365, 2013.

[47] G. Milione, A. Dudley, T. A. Nguyen, O. Chakraborty, E. Karimi, A. Forbes, and R. R. Alfano, "Measuring the self-healing of the spatially inhomogeneous states of polarization of vector bessel beams," *Journal of Optics*, vol. 17, no. 3, p. 035617, 2015.

[48] E. Otte, I. Nape, C. Rosales-Guzmán, A. Vallés, C. Denz, and A. Forbes, "Recovery

of local entanglement in self-healing vector vortex bessel beams," *arXiv preprint arXiv:1805.08179*, 2018.

[49] I. Nape, E. Otte, A. Vallés, C. Rosales-Guzmán, F. Cardano, C. Denz, and A. Forbes, "Self-healing high-dimensional quantum key distribution using hybrid spin-orbit bessel states," *Optics express*, vol. 26, no. 21, pp. 26 946–26 960, 2018.

[50] M. McLaren, T. Mhlanga, M. J. Padgett, F. S. Roux, and A. Forbes, "Self-healing of quantum entanglement after an obstruction," *Nature communications*, vol. 5, p. 3248, 2014.

[51] V. Garcés-Chávez, D. McGloin, H. Melville, W. Sibbett, and K. Dholakia, "Simultaneous micromanipulation in multiple planes using a self-reconstructing light beam," *Nature*, vol. 419, no. 6903, pp. 145–147, September 2002.

[52] S. Li and J. Wang, "Adaptive free-space optical communications through turbulence using self-healing bessel beams," *Scientific reports*, vol. 7, p. 43233, February 2017.

[53] F. O. Fahrbach, P. Simon, and A. Rohrbach, "Microscopy with self-reconstructing beams," *Nature Photonics*, vol. 4, no. 11, pp. 780–785, November 2010.

[54] M. Duocastella and C. B. Arnold, "Bessel and annular beams for materials processing," *Laser & Photonics Reviews*, vol. 6, no. 5, pp. 607–621, 2012.

[55] J. W. Goodman, *Introduction to Fourier Optics*, ser. McGraw-Hill physical and quantum electronics series. Roberts and Company Publishers, 2005.

[56] K. Iizuka, *Engineering Optics*, ser. Springer Series in Optical Sciences. Springer-Verlag New York, 2008.

[57] H. Volkmann, "Ernst abbe and his work," *Applied optics*, vol. 5, no. 11, pp. 1720–1731, November 1966.

[58] J. A. Davis, D. M. Cottrell, J. Campos, M. J. Yzuel, and I. Moreno, "Encoding amplitude information onto phase-only filters," *Applied optics*, vol. 38, no. 23, pp. 5004–5013, 1999.

[59] X. Chu and W. Wen, "Quantitative description of the self-healing ability of a beam," *Optics express*, vol. 22, no. 6, pp. 6899–6904, March 2014.

[60] A. E. Siegman, "Defining the effective radius of curvature for a nonideal optical beam," *IEEE Journal of Quantum Electronics*, vol. 27, no. 5, pp. 1146–1148, 1991.

[61] A. Forbes, *Laser beam propagation: generation and propagation of customized light*. CRC Press, 2014.

[62] R. L. Phillips and L. C. Andrews, "Spot size and divergence for laguerre gaussian beams of any order," *Applied optics*, vol. 22, no. 5, pp. 643–644, March 1983.

[63] N. Reng and B. Eppich, "Definition and measurements of high-power laser beam parameters," *Optical and quantum electronics*, vol. 24, no. 9, pp. S973–S992, September 1992.

[64] D. Zwillinger and A. Jeffrey, *Table of integrals, series, and products*. Elsevier, 2007.

[65] T. F. Johnston, "Beam propagation (m 2) measurement made as easy as it gets: the four-cuts method," *Applied optics*, vol. 37, no. 21, pp. 4840–4850, July 1998.

[66] A. Bencheikh, S. Chabou, and O. C. Boumeddine, "Far-field diffraction of obstructed laguerre-gaussian beams," *JOSA A*, vol. 37, no. 11, pp. C20–C26, 2020.

[67] A. D. Kiselev and D. O. Plutenko, "Optical trapping by laguerre-gaussian beams: Far-field matching, equilibria, and dynamics," *Physical Review A*, vol. 94, no. 1, p. 013804, 2016.

[68] V. Garbin, D. Cojoc, E. Ferrari, R. Z. Proietti, S. Cabrini, and E. Di Fabrizio,

"Optical micro-manipulation using laguerre-gaussian beams," *Japanese journal of applied physics*, vol. 44, no. 7S, p. 5773, 2005.

[69] A. Trichili, A. B. Salem, A. Dudley, M. Zghal, and A. Forbes, "Encoding information using laguerre gaussian modes over free space turbulence media," *Opt. Lett.*, vol. 41, no. 13, pp. 3086–3089, 2016.

[70] M. A. Cox, L. Maqondo, R. Kara, G. Milione, L. Cheng, and A. Forbes, "The resilience of hermite–and laguerre–gaussian modes in turbulence," *J.Light. Technol.*, vol. 37, no. 16, pp. 3911–3917, 2019.

[71] N. Bhebhe, C. Rosales-Guzman, and A. Forbes, "Classical and quantum analysis of propagation invariant vector flat-top beams," *Appl. Opt.*, vol. 57, no. 19, pp. 5451–5458, 2018.

[72] A. Forbes and I. Nape, "Quantum mechanics with patterns of light: Progress in high dimensional and multidimensional entanglement with structured light," *AVS Quantum Science*, vol. 1, no. 1, p. 011701, 2019.

[73] J. Mendoza-Hernández, M. L. Arroyo-Carrasco, M. D. Iturbe-Castillo, and S. Chávez-Cerda, "Laguerre–gauss beams versus bessel beams showdown: peer comparison," *Optics letters*, vol. 40, no. 16, pp. 3739–3742, August 2015.

[74] Z. Bouchal, J. Wagner, and M. Olivik, "Bessel beams in the focal region," *Opt. Eng.*, vol. 34, no. 6, pp. 1680–1689, 1995.

[75] B. Lü, W. Huang, and B. Zhang, "Fraunhofer diffraction of a bessel beam focused by an aperture lens," *Opt. Commun.*, vol. 119, no. 1-2, pp. 6–12, 1995.

[76] V. V. Kotlyar, A. A. Kovalev, and A. P. Porfirev, "Optimal phase element for generating a perfect optical vortex," *J. Opt. Soc. Am. A*, vol. 33, no. 12, pp. 2376–2384, 2016.

[77] I. S. Gradshteyn and I. M. Ryzhik, *Table of integrals, series, and products.* Academic press, 2014.

[78] A. Bencheikh, S. Chabou, O. C. Boumeddine, H. Bekkis, A. Benstiti, L. Beddiaf, and W. Moussaoui, "Cosine beam: diffraction-free propagation and self-healing," *JOSA A*, vol. 37, no. 11, pp. C7–C14, 2020.

[79] G. Libri, *Histoire des sciences mathématiques en Italie: depuis la renaissance des lettres jusqu'à la fin du XVIIe siècle.* chez Jules Renouard et C. ie, 1840, vol. 1.

[80] F. Cajori, "History of physic," 1962.

[81] F. Grimaldi, *Physico-mathesis de lvmine, coloribvs, et iride, aliisque adnexis libri duo: opvs posthvmvm*, 1665. [Online]. Available: https://books.google.dz/books?id=FzYVAAAAQAAJ

[82] P. Drude, "The theory of optics, trans. cr mann and ra millikan," 1959.

[83] A. E. Shapiro, "Kinematic optics: A study of the wave theory of light in the seventeenth century," *Archive for history of exact sciences*, vol. 11, no. 2-3, pp. 134–266, 1973.

[84] H. Huygens, "Traité de la lumiere, pierre vander aa, marchand libraire, leide (1690, in french)."

[85] S. J. Rigaud, *Correspondence of Scientific Men of the Seventeenth Century: Including Letters of Barrow, Flamsteed, Wallis, and Newton, Printed from the Originals in the Collection of the Right Honourable the Earl of Macclesfield: In Two Volumes.* University Press, 1841, vol. 2.

[86] T. Young, "I. the bakerian lecture. experiments and calculations relative to physical optics," *Philosophical transactions of the Royal Society of London*, no. 94, pp. 1–16, 1804.

[87] J. Stratton, "Electromagnetic theory. mcgraw-hill book company, inc," 1941.

[88] J. Durnin, "Exact solutions for nondiffracting beams. i. the scalar theory," *JOSA A*, vol. 4, no. 4, pp. 651–654, 1987.

[89] M. A. Bandres, J. C. Gutiérrez-Vega, and S. Chávez-Cerda, "Parabolic nondiffracting optical wave fields," *Optics letters*, vol. 29, no. 1, pp. 44–46, 2004.

[90] C. López-Mariscal, M. A. Bandres, J. C. Gutiérrez-Vega, and S. Chávez-Cerda, "Observation of parabolic nondiffracting optical fields," *Optics express*, vol. 13, no. 7, pp. 2364–2369, 2005.

[91] C. Vetter, R. Steinkopf, K. Bergner, M. Ornigotti, S. Nolte, H. Gross, and A. Szameit, "Realization of free-space long-distance self-healing bessel beams," *Laser & Photonics Reviews*, vol. 13, no. 10, p. 1900103, 2019.

[92] C. López-Mariscal and K. Helmerson, "Shaped nondiffracting beams," *Optics letters*, vol. 35, no. 8, pp. 1215–1217, 2010.

[93] W. Shaomin, L. Qiaug, and L. Xuanhui, "Super-diffraction limiting propagation of cos beams [j]," *APPLIED LASER*, vol. 2, 1994.

[94] S. Wang, Q. Lin, and X. Lu, "Realization of super-diffraction limiting propagation by cos beams," *Optik (Stuttgart)*, vol. 100, no. 1, pp. 8–10, 1995.

[95] Z. Jiang, "Truncation of a two-dimensional nondiffracting cos beam," *JOSA A*, vol. 14, no. 7, pp. 1478–1481, 1997.

[96] C. J. Sheppard, "Pupil filters for generation of light sheets," *Optics express*, vol. 21, no. 5, pp. 6339–6345, 2013.

[97] I. Golub, B. Chebbi, and J. Golub, "Toward the optical "magic carpet": reducing the divergence of a light sheet below the diffraction limit," *Optics letters*, vol. 40, no. 21, pp. 5121–5124, 2015.

[98] D. Wilding, P. Pozzi, O. Soloviev, G. Vdovin, C. J. Sheppard, and M. Verhaegen, "Pupil filters for extending the field-of-view in light-sheet microscopy," *Optics letters*, vol. 41, no. 6, pp. 1205–1208, 2016.

[99] B.-J. Chang and R. Fiolka, "Light-sheet engineering using the field synthesis theorem," *Journal of Physics: Photonics*, vol. 2, no. 1, p. 014001, 2019.

[100] H. T. Eyyuboğlu and Y. Baykal, "Analysis of reciprocity of cos-gaussian and cosh-gaussian laser beams in a turbulent atmosphere," *Optics Express*, vol. 12, no. 20, pp. 4659–4674, 2004.

[101] C. Ding, L. Liao, H. Wang, Y. Zhang, and L. Pan, "Effect of oceanic turbulence on the propagation of cosine-gaussian-correlated schell-model beams," *Journal of Optics*, vol. 17, no. 3, p. 035615, 2015.

[102] W. Wan-Jun and W. Zhen-Sen, "Propagation of annular cos-gaussian beams through turbulence," *JOSA A*, vol. 35, no. 7, pp. 1165–1172, 2018.

[103] J. Lin, J. Dellinger, P. Genevet, B. Cluzel, F. de Fornel, and F. Capasso, "Cosine-gauss plasmon beam: a localized long-range nondiffracting surface wave," *Physical Review Letters*, vol. 109, no. 9, p. 093904, 2012.

[104] S. Fu, Y. Tsur, J. Zhou, L. Shemer, and A. Arie, "Propagation dynamics of non-spreading cosine-gauss water-wave pulses," *Physical review letters*, vol. 115, no. 25, p. 254501, 2015.

[105] J. Turunen, A. Vasara, and A. T. Friberg, "Holographic generation of diffraction-free beams," *Applied optics*, vol. 27, no. 19, pp. 3959–3962, 1988.

[106] R. El Attar, *Special functions and orthogonal polynomials*. Lulu. com, 2006, vol. 3.

[107] B. M. Project, A. Erdélyi, and H. Bateman, *Tables of integral transforms: based in part on notes left by Harry Bateman and compiled by the staff of the Bateman manuscript project*. McGraw-Hill, 1954.

[108] S. Chabou and A. Bencheikh, "Elegant gaussian beams: nondiffracting nature and self-healing property," *Applied Optics*, vol. 59, no. 32, pp. 9999–10 006, 2020.

[109] M. Mazilu, D. J. Stevenson, F. Gunn-Moore, and K. Dholakia, "Light beats the spread:"non-diffracting" beams," *Laser & Photonics Reviews*, vol. 4, no. 4, pp. 529–547, 2010.

[110] R. A. Silverman *et al.*, *Special functions and their applications*. Courier Corporation, 1972.

[111] A. Bencheikh and A. Forbes, "The non-diffracting nature of truncated hermite–gaussian beams," *JOSA A*, vol. 37, no. 11, pp. C1–C6, 2020.

[112] S. Saghafi and C. Sheppard, "Near field and far field of elegant hermite-gaussian and laguerre-gaussian modes," *Journal of Modern Optics*, vol. 45, no. 10, pp. 1999–2009, 1998.

[113] G. Zhou, R. Qü, and L. Sun, "The structural properties of cosine-gaussian beam in the far field," *Journal of Modern Optics*, vol. 55, no. 15, pp. 2485–2495, 2008.

[114] R. Borghi and M. Santarsiero, "M 2 factor of bessel–gauss beams," *Optics letters*, vol. 22, no. 5, pp. 262–264, 1997.

[115] S. Saghafi and C. Sheppard, "The beam propagation factor for higher order gaussian beams," *Optics communications*, vol. 153, no. 4-6, pp. 207–210, 1998.

[116] M. A. Porras, R. Borghi, and M. Santarsiero, "Relationship between elegant laguerre–gauss and bessel–gauss beams," *JOSA A*, vol. 18, no. 1, pp. 177–184, 2001.

[117] M. A. Alonso and M. R. Dennis, "Ray-optical poincaré sphere for structured gaussian beams," *Optica*, vol. 4, no. 4, pp. 476–486, 2017.

[118] T. Malhotra, R. Gutiérrez-Cuevas, J. Hassett, M. Dennis, A. Vamivakas, and

M. Alonso, "Measuring geometric phase without interferometry," *Physical review letters*, vol. 120, no. 23, p. 233602, 2018.

Abstract:

Laser beam propagation has been a subject of active research for over 50 years.

Throughout this thesis, we study the propagation behavior of different laser Gaussian beams, such as Laguerre Gaussian and Hermite Gaussian beams, passed through diffractive optical elements (aperture, opaque disk, prism). We perform an investigation into the parameters (the beam propagation factor, focal shift effect, beam width, free-diffraction range, ...) that delineate the properties of these propagated beams (non-diffracting nature and self-healing property), through quantitative and qualitative measurements.

The understanding and identification of such beam properties will be useful for various fields.

Keywords: Gaussian beams, laser beam propagation, diffraction, laser beam characteristics.

Résumé:

La propagation du faisceau laser fait l'objet des recherches actives depuis plus de 50 ans. Tout au long de cette thèse, nous étudions la propagation des faisceaux lasers Gaussiens, tels que les faisceaux Laguerre-Gauss et Hermite-Gauss, passés à travers des éléments optiques diffractifs (ouverture, disque opaque, prisme). Nous effectuons une investigation sur les paramètres (facteur de qualité M^2, l'effet du décalage focal, la largeur, la région de diffraction libre, ...) qui délimitent les propriétés de ces faisceaux propagés (la nature non diffractant et la propriété d'auto-reconstruction), par des mesures quantitative et qualitative.

La compréhension et l'identification de ces propriétés des faisceaux seront utiles pour divers domaines.

Mots-clés: Les faisceaux Gaussiens, propagation des faisceaux lasers, la diffraction, les caractéristiques des faisceaux lasers.

ملخص :

كان انتشار شعاع الليزر موضوع بحث لما يزيد عن 50 عامًا.

من خلال هذه الأطروحة ، ندرس سلوك انتشار مختلف أشعة الليزر الغاوسية ، المارة عبر العناصر البصرية الانعكاسية (الفتحة ، القرص المعتم ، المنشور). نقوم بإجراء تحقيق في المعلمات (عامل انتشار الحزمة، وتأثير التحول البؤري، وعرض الحزمة، ومنطقة الانعراج الحر، ...) التي تحدد خصائص هذه الحزم المنتشرة (الطبيعة غير المشتتة وخاصية الشفاء الذاتي) ، من خلال القياسات الكمية والنوعية.

فهم وتحديد خصائص الحزمة سيكون مفيدًا لكثير من المجالات.

الكلمات المفتاحية: أشعة جاوس ، انتشار شعاع الليزر ، الانعراج ، خصائص شعاع الليزر.